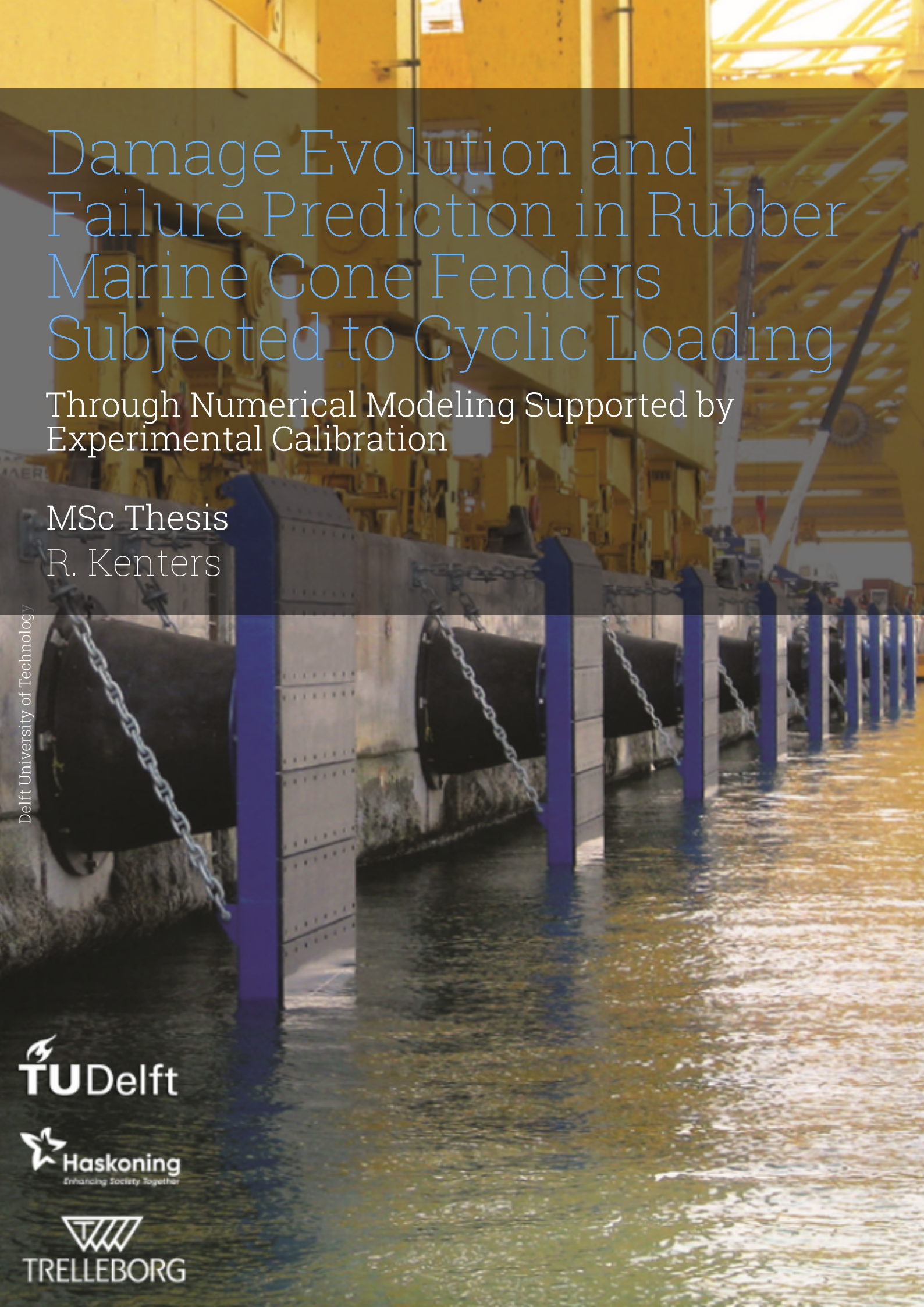

Damage Evolution and Failure Prediction in Rubber Marine Cone Fenders Subjected to Cyclic Loading

Through Numerical Modeling Supported by Experimental Calibration

MSc Thesis

R. Kenters

Delft University of Technology

TU Delft

Haskoning
Enhancing Society Together

TRELLEBORG

Damage Evolution and Failure Prediction in Rubber Marine Cone Fenders Subjected to Cyclic Loading

Through Numerical Modeling Supported by Experimental Calibration

by

R. Kenters

Master Thesis

in partial fulfillment of the requirements for the degree of

Master of Science
in Mechanical Engineering

at the Department Maritime and Transport Technology of Faculty Mechanical, Maritime and Materials Engineering of Delft University of Technology

to be defended publicly on Tuesday January 13, 2026, at 12:15 PM

Student number: 5184894
MSc track: Multi-Machine Engineering
Report number: 2025.MME.9152

Supervisor:	Dr. C.L. (Carey) Walters	
Thesis committee:	Dr. J. (Jovana) Jovanova	TU Delft committee chair, Mechanical Engineering
	Dr. A.A. (Alfred) Roubos	TU Delft committee chair, Civil Engineering and Geosciences
	Dr. A.F.J. (Alex) van Deyzen	Company supervisor, Haskoning
	ing. M. (Marco) Gaal	Company supervisor, Trelleborg
Date	January 4 , 2026	

An electronic version of this thesis is available at http://repository.tudelft.nl/

Cover: Trelleborg's Super Cone Fenders (SCN)
Style: TU Delft Report Style

TU Delft

Haskoning
Enhancing Society Together

TRELLEBORG

Preface

Hereby, I present my Master's thesis titled: "Damage Evolution and Failure Prediction in Rubber Marine Cone Fenders Subjected to Cyclic Loading". This work represents the final stage of the Master of Science in Mechanical Engineering with the corresponding track of Multi-Machine Engineering at Delft University of Technology.

This study was supervised by Dr. C.L. (Carey) Walters, associate professor in the Maritime Transport and Technology and in collaboration with Haskoning and Trelleborg. By combining experimental calibration tests with numerical models, this thesis aims to provide a more reliable estimation of the service life of rubber marine cone fenders subjected to cyclic loading. These components ensure safe and efficient berthing operations in ports.

I would like to express my gratitude to everyone who supported me throughout this work. In particular, I would like to thank Carey Walters for his input and feedback during this research. I also wish to thank Alex van Deyzen for the guidance from Haskoning and Marco Gaal, for the guidance from Trelleborg, and for providing the rubber samples used in the experimental tests. Finally, I would like to thank Wei Jun Wong for assisting me with the testing procedure in the laboratory.

R. Kenters
Delft, January 2026

Abstract

Marine rubber cone fenders are critical components in port infrastructure designed to absorb the kinetic energy of a berthing vessel. However, when a vessel is permanently moored in harsh wave and wind environments, the fenders are subjected to cyclic loading due to resonant vessel motions. This can result in 500.000 fender deflections per year, which can cause complete rupture of the cone fender due to fatigue. The PIANC 2024 mentioned that within current guidelines, there is insufficient information available to provide limits for fenders subjected to cyclic loading. This thesis addresses the gap to characterize damage evolution and predict the service life of rubber marine cone fenders subjected to cyclic loading. In this study, the Super Cone fender of Trelleborg with a height of 400 millimeters (SCN 400) was used as a reference model. First, experimental uniaxial tension and compression tests were performed. Three different engineering strain rates were tested to capture the rate dependence of the rubber. This provided input for the determination of the stress strain relationships that were subsequently used to calibrate the hysteresis material model in Abaqus. The Bergström–Boyce model showed the best correlation with the experimental data among the models investigated with a total normalized mean absolute difference of 9.4%. To investigate the most suitable damage parameter, a data set from the literature containing uniaxial fatigue data on natural rubber has been used. To gain insight into the corresponding stresses and strains, the fatigue specimen was modeled in FEA. The maximum principal stress, shown to be effective in multiaxial fatigue and exhibiting the highest correlation across all loading ratios in the data set studied, was selected as the most suitable damage parameter. The cone fender was implemented in FEA using axisymmetric four-node quadrilateral hybrid elements (CAX4RH) within an implicit quasi-static dynamic framework in Abaqus. The FEA model was found to have a maximum reaction force of approximately 14% higher than the experimental performance, while matching the overall shape of the force deflection curve. The steepest decrease in predicted service life was observed for deflections up to the buckling point. The influence of loading velocity on stress states was analyzed by selecting three critical elements with relatively high maximum principal stress development. The average increase in stress among critical elements was found to be the highest in the buckling phase during compression. When the loading velocity increased by a factor of eight, the average stress in this phase increased by 38%, corresponding to a reduction of 57% of its predicted service life. In addition, the average increase in the maximum principal stress among the critical elements was closely related to the increase in stress in the uniaxial tension experiments at a strain of 0.3 when the strain rate was increased by a factor of ten. Finally, modifications have been made to the example cone fender to enhance its suitability for handling a large amount of small energies. A geometric variation analysis had been conducted that resulted in the selection of two important dimensional parameters. Focusing on the inner radius and the angle of the inner axis led to a design that achieved a 32% increase in energy absorption up to the defined maximum principal stress limit.

Keywords: Rubber Cone Fenders, Service Life, Fatigue, Cyclic Loading, Damage Parameters

AI statement

For this thesis, generative AI has been used to support and enhance this work in the following ways:

- The visualization of data and the generation of Python plots. The codes with corresponding plots were all reviewed, tested, and adjusted where necessary.
- Solving problems and errors in Latex overleaf and formatting figures and tables in the desired layout.
- The conversion of tables with numerical data from Excel or Python to Latex overleaf.
- Grammar was checked with the built in function in Latex overleaf and words were replaced in certain cases to improve sentences.

Contents

Nomenclature

Abbreviations

CB	Carbon Black
CDIT	Coastal Development Institute of Technology
CED	Crack Energy Density
DIC	Digital Image Correlation
DOF	Degree(s) of Freedom
EPDM	Ethylene Propylene Diene Monomer
EPFM	Elastic–Plastic Fracture Mechanics
FEA	Finite Element Analysis
FSRU	Floating Storage and Regasification Unit
LEFM	Linear Elastic Fracture Mechanics
LMA	Levenberg–Marquardt Algorithm
NMAD	Normalized Mean Absolute Difference
NR	Natural Rubber
PIANC	Permanent International Association of Navigation Congresses
SBR	Styrene–Butadiene Rubber
SCN	Super Cone Fender
SED	Strain Energy Density
SR	Synthetic Rubber
TF	Temperature Factor
UV	Ultraviolet
VF	Velocity Factor
WG	Working Group

Symbols

Symbol	Description	Unit
E	Kinetic energy to be absorbed by fenders and structure	kNm
E_c	Characteristic berthing energy	kNm
E_d	Design berthing energy	kNm
E_{base}	Base fender performance energy	kNm
$E_{f,d}$	Design fender energy absorption	kNm
M	Displacement of the vessel	tonnes
B	Breadth of the ship	m
v	velocity	m/s
A	Area	m^2
F	Force	N
C_M	Virtual mass coefficient	–
C_E	Eccentricity coefficient	–
C_S	Softness factor of the vessel–fender system	–
C_C	Berth configuration factor	–
C_V	Velocity factor	–
C_T	Temperature factor	–
C_A	Angular (berthing-angle) factor	–
C_m	Multiple fender contact factor	–
γ_E	Partial energy factor	–
γ_m	Partial material factor	–
K	Radius of gyration of the vessel	m
E	Young's modulus	Pa
G	Shear modulus	Pa
E^*	Complex modulus	Pa
E'	Storage modulus	Pa
E''	Loss modulus	Pa
G^*	Complex shear modulus	Pa
G'	Storage shear modulus	Pa
G''	Loss shear modulus	Pa
δ	Phase lag / loss angle	rad or °
$\tan\delta$	Loss tangent	–
σ	Cauchy (true) stress	Pa
τ	Kirchhoff stress	Pa
P	First Piola–Kirchhoff stress tensor	Pa
S	Second Piola–Kirchhoff stress tensor	Pa
ε	Strain	–
ν	Poisson's ratio	–
ρ	Density	kg/m^3
F	Deformation gradient tensor	–
λ	Principal stretch ratio	–
$\lambda_{1,2,3}$	Principal stretches in three material directions	–
I_1, I_2, I_3	Invariants of Cauchy–Green deformation tensor	–
W	Strain energy density	Pa
D	Compressibility parameter	–
N_f	Number of cycles to failure	–
R	Loading ratio	–

List of Figures

List of Tables

1

Introduction

Marine fenders are essential components in port infrastructure, designed to protect vessels and quay structures from forces that occur during mooring operations. The main function of a fender system is to absorb the energy of a berthing vessel and to dissipate the associated reaction forces into the supporting structure [2]. Before fenders were developed approximately 60 years ago, old wires and wood were used for this application. From then on, the fenders have developed significantly in both size and variety to handle the increasing dimensions and diversity of vessels [3].

Ports play a crucial role in the distribution of goods, since 80% of goods are transported by sea [48]. When fenders suddenly fail, this can lead to delays in operations, damage to vessels and qua walls, and increased maintenance costs. In busy ports, this will have a significant impact on supply chains and the economy. Moreover, sudden failure of fenders, may lead to additional safety risks to personnel and in case of the transportation of chemicals, this may even lead to environmental accidents such as oil spills. Since ports have become busier over the years [18] and vessel sizes are increasing, this topic will become even more relevant.

Today, in most cases, rubber cone fenders with steel panels are used due to their high efficiency, energy absorption capabilities, and suitability for angular loads. Therefore, this study is focused on that specific type. Currently, the fender selection process is based on berthing energy and does not take cyclic loading into account. When vessels such as Floating Storage and Regasification Units (FSRUs) are permanently moored in harsh wave and wind environments, this can cause 500.000 fender compressions per year [20] due to resonant vessel motions. Resonant vessel motions typically occur when the wave or wind forces match or are close to the vessel's natural frequency [25].

The PIANC 2024 [2] considers 3000 full compression cycles for experimental durability testing raising the question of whether cone fenders can withstand this large number of deflections without failure. In recent cases in the industry, cone fenders failed too quickly due to complete rupture in cases with cyclic loading. The PIANC 2024 mentioned that within the current guidelines, there is insufficient data available to provide limits for cone fenders subjected to a large number of fender compressions.

This study will use experimental and numerical models of the behavior of rubber to estimate the damage development and predict the service life of cone fenders subjected to cyclic loading. Furthermore, it proposed a design with improved service life for these specific cases. The central main question of this research is defined as follows: "How does the local distribution of stress and strain within a rubber cone fender affect crack initiation when subjected to cyclic loading, and how can this be predicted?"

1.1. Research questions

This thesis will investigate the following research questions. The main research question is defined as: ”How does the local distribution of stress and strain within a rubber cone fender affect crack initiation when subjected to cyclic loading, and how can this be predicted?” This main research question is divided into the following sub-questions.

1. What is the most suitable damage parameter that can describe crack initiation due to fatigue in a rubber cone fender?
2. How is the applied loading velocity related to the local strain rate at a specific position within the rubber cone fender?
3. How does loading velocity affect stress states at a specific position within the rubber cone fender?
4. Which loading ratio (R-ratio) during cyclic loading provides the most reliable prediction of fatigue-related service life in rubber cone fenders?
5. To what extent can the geometry of the rubber cone fender be optimized to improve its service life in cyclic loading conditions?

1.2. Thesis structure

The structure of the thesis is organized as follows. In chapter 2 the background of buckling fenders is discussed and the way they are normally selected for a specific application. In chapter 3 a literature review is performed that explores the mechanical properties of rubber and the constitutive models available to describe its specific behavior. In addition, this chapter focuses on mechanics responsible for the softening of rubber after repeated load cycles and fatigue models that are commonly used to characterize the service life of rubber until crack initiation and subsequently crack propagation. chapter 4 describes the uniaxial tension and compression test procedures performed in the laboratory of Delft University of Technology. The results of the experiments are discussed, and based on these results a rate-dependent constitutive model is fitted to capture the behavior of the rubber compound. In chapter 5 the most suitable damage parameter is investigated based on a uniaxial dataset of natural rubber including multiple loading ratios. Several damage parameters are investigated, and their correlation is assessed with the least squares method. In chapter 6 the example cone fender is implemented in FEA using Abaqus and the strain rates and stress states are analyzed. chapter 7 proposes a optimization for the cone fender geometry, aiming to maximize energy absorption under a certain stress limit. Boundary conditions are defined to constrain the allowable force and minimum required efficiency. This results in a design that is better suited for situations involving cyclic loading and is expected to have an improved service life based on three cases investigated.

2

Background

2.1. Buckling fenders working principle

Buckling fenders consisting of cone, cell, element, or element/leg fenders and have a characteristic force deflection curve as indicated in Figure 2.2. In the initial stage, the reaction force increases linearly as a result of elastic deformation until it reaches a certain amount of force after which the fender buckles, and its reaction force remains more or less constant with increasing deflection until it bottoms out, and then the reaction force increases monotonically. Typically, a buckling fender operates around an energy absorption efficiency of around 70 to 80% [2] of its maximum capacity. The maximum capacity assumes that during compression, the reaction force remains constant after buckling. Due to the high efficiency, the maximum reaction force is early reached in the compression process approximately at half the deflection.

Figure 2.1: Cone, cell and element/leg fenders [2]

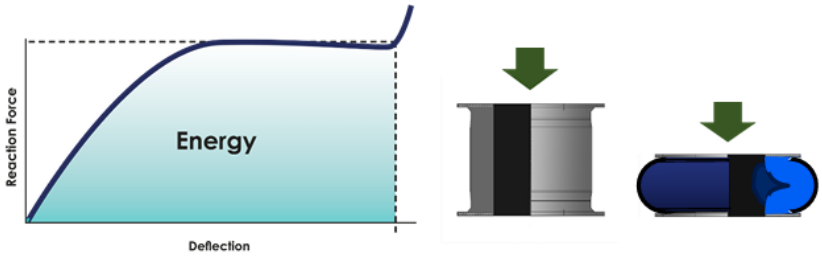

Figure 2.2: Buckling fender force deflection curve [2]

2.2. Berthing calculation based on berthing energy

Fenders improve the safety of berthing operations by absorbing the kinetic energy of the vessel. The fenders absorb a part of the energy and the other part is converted to the supporting structure, or into elastic deformation of the vessel hull [21]. For safe berthing, the allowable energy absorbed by the fenders and the allowable hull pressure of the vessel must not be exceeded. The allowable hull pressure depends on the size, design, and type (container, cargo, or bulk carrier) of the vessel and can range between 150-700 kPa [8]. The berthing energy indicates the amount of energy available when a

vessel berths. In order to calculate the berthing energy, a frequently used guideline is the PIANC 2024 [2]. The basic formulation for the calculation of the berthing energy (neglecting angular velocity vessel) can be taken as given in Eq. 2.1 with the corresponding descriptions in Table 2.1.

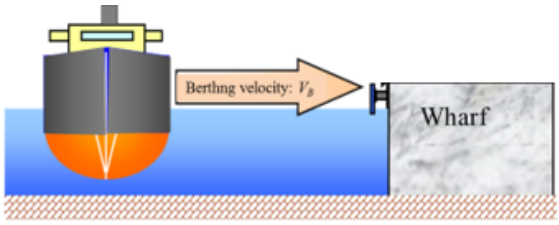

Figure 2.3: Berthing energy [70]

$$E = \frac{1}{2} M v_B^2 C_M C_E \tag{2.1}$$

Table 2.1: Symbols berthing energy and their descriptions

Symbol	Description
E	Kinetic energy to be absorbed by fenders and structure (kNm).
M	Displacement of the vessel (tonnes).
v_B	Normal component of vessel's velocity to structure (m/s).
C_M	Virtual mass coefficient, measured the additional mass due to added water.
C_E	Eccentricity coefficient, calculated for the rotation of a vessel.

Eq. 2.1 differs from PIANC WG 33 (and others), for the following reasons. The working group has removed the softness factor (C_S) based on [8], which shows that the contribution of the elastic vessel hull is below 1%. The berth configuration factor (C_C) has been removed because this effect is now included in the berthing velocity recordings used to determine the characteristic berthing velocity.

Virtual mass coefficient
When a vessel is in motion through the water, it is subjected to additional hydrodynamic and drag forces due to viscous effects that slow the vessel [2]. Inertial forces caused by the mass of the surrounding water around the vessel resist changes in velocity and are known as added mass and are accounted for with the added mass factor (C_M). The most important variable is the clearance under the keel of the vessel. The mass factor can be calculated with Eq. 2.2 with the parameters draft of the vessel (D) and breadth of ship (B) [5].

$$C_M = 1 + \frac{2D}{B} \tag{2.2}$$

Eccentricity coefficient
During the moment of impact of the vessel to the quay, a part of the kinetic energy is converted into rotational energy of the vessel at the moment of impact with the fender. This relation is defined in the eccentric coefficient [21] and could be determined with Eq. 2.3. The rotation of the vessel takes place at the point of contact of the fender.

$$C_E = \frac{K^2 + R^2 \cos^2 \gamma}{K^2 + R^2} \tag{2.3}$$

Table 2.2: Symbols and their descriptions for eccentricity coefficient

Symbol	Description
K	Radius of gyration of the vessel (m).
R	Distance of the line parallel to the quay from the vessel's center of gravity (m).
γ	Angle between the normal components of the vessel's velocity and the line crossing the center of gravity and contact point (°).

Design berthing energy

The design berthing energy can be calculated with Eq. 2.4. Here, the characteristic berthing energy (E_C) accounts for the uncertainty of the berthing velocity, the displacement of the vessel, and the berthing angle. Then it is multiplied by the partial energy factor (γ_E) which contains corrections for factors such as annual berthing frequency, pilot assistance, and vessel size correlations.

$$E_d = \gamma_E E_C \tag{2.4}$$

2.2.1. Performance correction factors

Using the design berthing energy, the base performance of the fender could be determined according to tables from the fender supplier with data for each type, size and possible rubber fender. After identifying the correction factors based on the design criteria of the project, the characteristic performance can be calculated with Eq. 2.5. To ensure project reliability, partial resistance factors of safety are applied to the characteristic performance to determine fender design performance using the partial material factor (γ_m) according to Eq. 2.6. To verify that the selected fender is suitable, the designer should check whether Eq. 2.7 is valid.

$$E_c = E_{\text{base}}\, C_v\, C_t\, C_a\, C_m \tag{2.5}$$

$$E_{f,d} = \frac{E_c}{\gamma_m} \tag{2.6}$$

$$E_{f,d} \geq E_d \tag{2.7}$$

Velocity factor

Typical berthing velocities for vessels range from 20 mm/s to 500 mm/s [67]. In an ideal scenario, the fender manufacturers would test at actual velocities. However, due to the expensive equipment and wide range of fenders in the market, this is a challenging task. For a certain velocity, two factors influence the velocity factor (VF). The compression rate (compression time) and the type of rubber. Compression time is directly correlated with compression rate and has a significant impact on VF as shown in Figure 2.4. A larger fender takes more time to compress and has at the same berthing velocity a lower compression rate and VF compared to a smaller fender. The compound of rubber discussed in section 2.3 also has an impact on VF. For example, 100% natural rubber will have a lower VF than 100% synthetic rubber due to the difference in stress relaxation. The magnitude of VF is important because it affects the fender performance characteristics (reaction force and energy absorption) at normal berthing velocities.

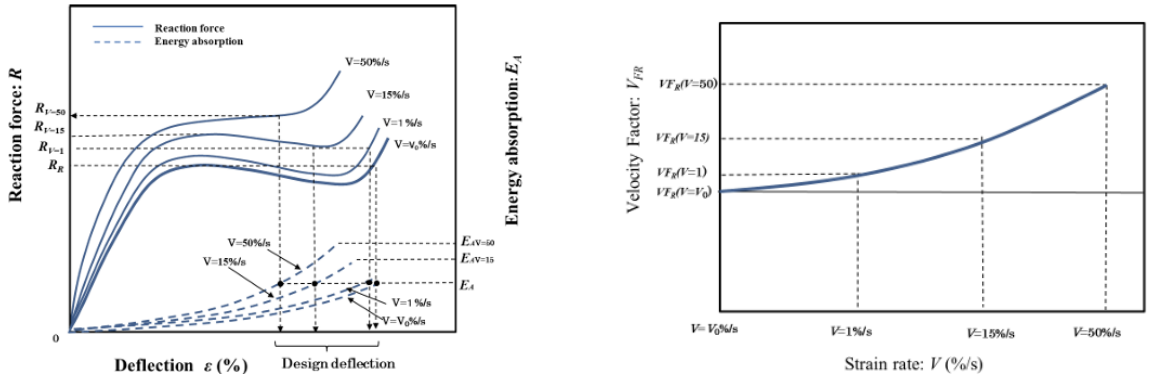

(a) Performance at different compression velocities [70]

(b) Influence of compression rate on VF [70]

Figure 2.4: Comparison of the influence of velocity factor and compression rate on fender performance.

Angular factor

The fender compression angle is defined as the angle that the vessel hull created against the berthing structure at the point of impact [2]. This is a combination of the horizontal and vertical angle of the hull profile at the bow onto the berth. In case of dolphins and monopiles, the effect of angular compression is even more important. Designers must be sure that during compression, the fender does not hit the supporting structure. The angular factor takes the energy loss into account in calculating the absorption capability. The energy absorption capability of the fenders reduces with larger angles. Therefore, the angular factor reduces as well with larger angles. Ignoring the amount of energy loss can underestimate the forces acting on the fender and supporting structure.

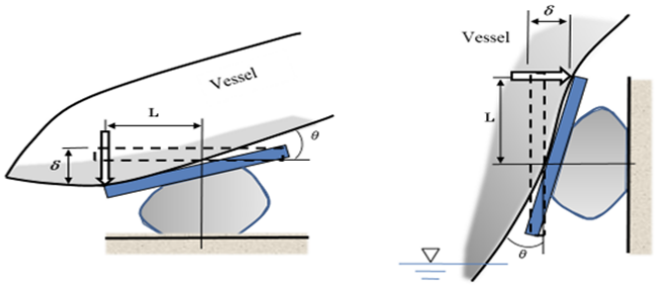

Figure 2.5: Angular horizontal and vertical berthing [70]

Temperature factor

Rubbers are measured with stress and strain behavior and rated with the modulus (stiffness) of the rubber compound [67]. The elasticity of rubber is important because it is directly proportional to the reaction force and thus energy absorption. Rubber loses its stiffness when it is warm and becomes stiffer when cold. The maximum reaction force will occur at the lowest operating temperature, whereas the minimum energy absorption will occur at the highest temperature [2]. To accommodate temperature changes, it is essential to apply the temperature factor (TF) during fender design.

Multiple fender contact factor

When a vessel contacts multiple fenders at the same time, which is typical for parallel berthing, the total kinetic energy is distributed across them. This results in a system that has a higher total energy absorption capacity in comparison with a single fender, enabling designers to select multiple smaller fenders that reduce the reaction force on the supporting structure. The multiple fender contact factor (range from 1.5 to 3.0) is determined through an approach considering fender pitch (center to center distance), fender size, and vessel geometry. Often simulations are required to imitate berthing situations [2]. In this way, the optimal number of fenders can be chosen, ensuring an effective berthing operation.

2.3. Compound fenders

The mechanical properties of the specific rubber material depend strongly on the compounding ingredients and the manufacturing process [47]. Therefore, it is important to carefully consider the compound structure of the rubber fenders. The optimal composition of the rubber may differ by location or berthing situation depending on the desired properties. Typical ingredients of rubber cell/cone fenders with each their own functionalities will be discussed in this section.

Typically, fenders are made from natural rubber (NR), synthetic rubber (SR), or a blend of both. NR is valued for its excellent mechanical properties that include high tensile strength and elasticity and builds up heat up slower than synthetic rubbers. Synthetic rubber is an artificial elastomer and can be made from petroleum by polymerization. Two of the most commonly used synthetic rubbers are styrene butadiene rubber (SBR) and ethylene propylene diene monomer (EPDM). SBR has excellent abrasion resistance and aging properties comparable to those of NR. Because SBR can withstand temperature ranges from 45° C to 100° C it is perfect for environments with higher temperatures and wear loading [33]. However, manufacturers also employ EPDM because of its ability to withstand aging, weathering, oxygen, and chemicals, making it suitable for harsh conditions [14]. In summary, synthetic rubbers often offer advantages such as consistent quality, availability, and enhanced resistance to environmental factors, but lack the mechanical strength of NR in general.

Recycled rubber, which is made mostly from crumbled and reclaimed (devulcanized) rubber, is due to its advantages for the environment and economy, becoming more important in the fender industry. The production of recycled rubber is an energy-intensive process in which the powder is heated under pressure with certain additional corrosive chemicals that break long rubber molecules into shorter lengths [2]. Although recycled rubber may be cheaper and more environmentally friendly than virgin rubber, its mechanical properties are totally different. The fender sector currently lacks the knowledge necessary for the successful integration of recycled rubber. Incorrect mixing with virgin rubber leads to performance issues such as increased hysteresis, heat build-up, reduced weather resistance, and increased risk of cracking [64].

In addition to raw rubber, a typical fender consists of a (reinforcement) filler and 20-30% other smaller ingredients [41]. Carbon black is currently a well established reinforcement material in the market. By adding this material, the tensile strength of the compound increases until it reaches the critical stage, after which the tensile strength decreases [69]. Another well-known reinforcement material is calcium carbonate. Adding calcium carbonate enhances the ability of the process and improves the behavior during vulcanization. Despite these advantages, it has a bad reputation in the market because in some cases it led to poorer performance and reduced durability in rubber fenders [64]. The other smaller ingredients consist of oil, which reduces the viscosity of rubber, accelerators that speed up the vulcanization process, and antioxidants that protect the material from oxidative degradation.

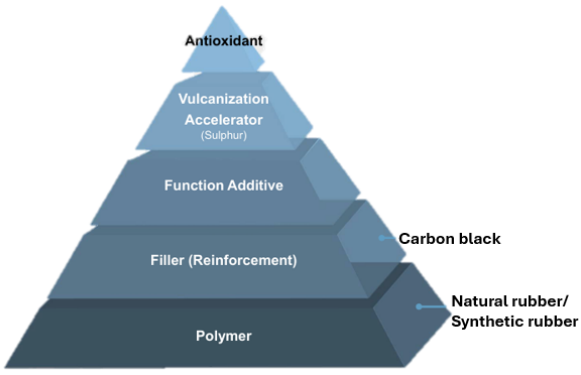

Figure 2.6: Compounding structure [41]

Table 2.3: Composition ingredients

Ingredients	%
Raw rubber (polymer)	40–45
Filler (reinforcing)	30–40
Oil (functional additives)	20–10
Others (S + ACC etc.)	10–5
Total	**100**

2.4. Impact of location

In Figure 2.7 three different types of mooring scenarios of FSRUs (Floating Storage and Regasification Units) are illustrated. Each mooring scenario has to deal with its own environmental circumstances. Often, a rough estimate could be made of the seriousness of the environmental conditions in the place of the moored vessel. For example, the vessel in Indonesia 14 kilometers offshore will most likely experience more movements than the vessel in Groningen protected with land. However, to select the right type of fender, a more in-depth mooring analysis must be performed, giving parameters such as the magnitudes and directions of the resultant force in time with an associated period. This is especially relevant in cases with cyclic loading, which represents a frequent amount of cycles (loading and unloading) in a short time period. This results in a large amount of fender compressions per day and can cause rapid fender failure due to fatigue. Because FSRUs and other permanently moored vessels are constantly subjected to these dynamic factors, this phenomenon is particularly applicable to them [20].

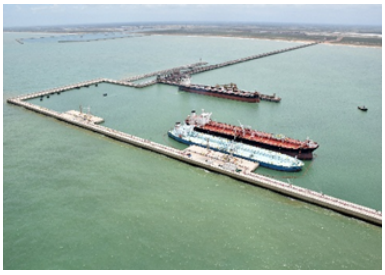

(a) Port of Açu in Brazil

(b) Port Eemshaven Groningen

(c) Indonesia (West Java) 14 km from coast

Figure 2.7: Differences in mooring locations

2.4.1. Operational factors

Besides the impact of the location of the moored vessel on the fender. Operational factors also play a crucial role in the lifespan of the fender. Busy ports expose fenders more often to the heavy impacts of arriving vessels as permanent moored vessels experience lower more frequent fender compressions in time [2]. In both cases, the vessel size is an important parameter for the exerted force on the fender. Furthermore, there are different types of mooring line configurations, which can be used for limiting the vessel movement. The choice of this specific configuration is strongly related to the magnitude of the forces and frequency working on the fender. In addition, the structure behind the fender is also important. The concrete quay is rigid, in contrast to a dolphin mounted on the sea bottom, which is less stiff. The consequence is that the fender with the concrete quay structure must withstand a greater reaction force than the fender with a dolphin structure.

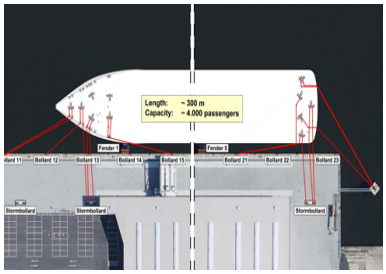

(a) Line configuration example [1]

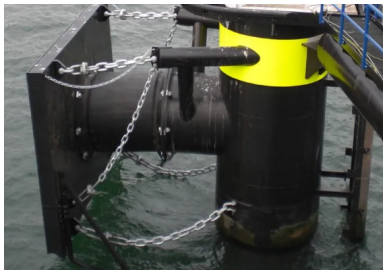

(b) Dolphin with cell fender [67]

Figure 2.8: Operational factors berthing at location

2.5. Environmental conditions

When a vessel is moored, it still has six degrees of freedom (DOF). Three translations (surge, sway, and heave) and three rotations (roll, pitch, and yaw) as shown in Figure 2.9. The vessel is subjected to forces such as wind, waves, and currents, which vary in time. Therefore, time-dependent equations of motion are required to calculate the forces acting on the fenders. In Eq. 2.8 the equation of motion in the time domain is illustrated [49]. Here are matrices A, B and C represent the added mass, damping, and stiffness, respectively. The vector F denotes the generalized force vector acting on the fender and x represents the generalized motion vector, containing the displacements in each degree of freedom. The time derivatives $\dot{x}$ and $\ddot{x}$ are the velocity and acceleration vectors, respectively.

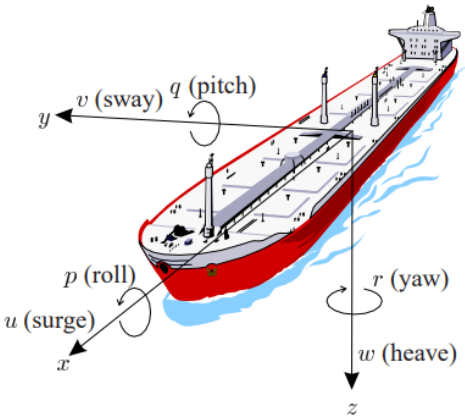

Figure 2.9: Vessel movements [34]

$$F_i = \sum_{j=1}^{6} \left[A_{i,j}\ddot{x}_j(t) + \int_{-\infty}^{t} B_{i,j}(t-\tau)\dot{x}_j(\tau)\,\mathrm{d}\tau + C_{i,j}x_j(t) \right] \tag{2.8}$$

Wind forces

Wind is a flow of air that is height dependent and non-stationary caused by variations in pressure and temperature. Because the load caused by the wind is proportional to the square of the wind velocity as shown in Eq. 2.9 in the x direction, high wind speeds cause significant loading. Especially with the growing wind areas of vessels that are becoming larger over years, this problem is something to consider. The drag coefficient (C_X) could be captured from the literature or determined with wind tunnel tests. Since the wind depends on the location with its own characteristics, local wind data should be used for analysis. In situations where local wind data are not available, simplified models can be used. Some guidelines use a constant maximum wind speed for mooring conditions. However, when the actual wind is higher, unexpected situations could occur. Therefore, the ROM guideline [16] could calculate the effect of wind fluctuations when only the mean wind force is known by applying gust factors. For the analysis of the force caused by the wind, the port policy is important. In some cases,

large vessels need to leave the port before a storm approaches. In this case, high wind speeds do not need to be taken into account during the analysis. Extreme wind conditions such as tornadoes and hurricanes are also crucial to consider. In most cases, the vessel leaves the port when these situations occur.

$$F_X = \frac{1}{2} \cdot C_X \cdot \rho \cdot v^2 \cdot A \tag{2.9}$$

Waves
All berthing places on seas, rivers, canals, and lakes experience waves-induced motions as a result of the wind. However, there are different types of waves that can occur in the ocean or along the coastline. For example, in some cases the waves will hit the quay and be reflected before reaching a moored vessel. In certain locations, such as rivers or ports behind locks, the impact of waves on the moored vessel may be minimal. However, in the cases where dolphins are placed in the ocean, waves could be the most important factor. For these cases, wave simulations have to be performed to get a better understanding of the dynamic movements of the vessel. A moored vessel has a natural motion of typically 50-200 seconds [25]. When there are long periods of wind waves (longer than 8 seconds) created by local winds or swells from storms, they have the ability to excite moored vessels. Furthermore, long-period gravity waves (longer than 30 seconds) caused by wave groups and shallow water have the potential to generate resonant vessel motions as they are in the range of the vessel's natural motion, resulting in large motions of the vessel. These resonant vessel motions should be avoided, causing rapid damage to the fenders.

Current
Current movements during berthing arise from tidal conditions, river flows, or generated by the wind. The force caused by the current on the vessel can be calculated in the same way as the wind force. Due to the high density of the flowing water, the resulting force can still be significantly large. The area below the waterline should be considered in the calculation. Therefore, it is the worst situation when a vessel is completely loaded. The current force is mostly applied as a constant load.

3

Literature review

This chapter contains the literature review of the thesis, that preliminary focuses on the properties of rubber and models available to characterize its behavior. In addition, methods are explored to predict the fatigue life of rubber.

3.1. Rubber behavior and constitutive models

3.1.1. Mechanical properties of rubber

Rubber is an elastomer that can be divided into two main categories, natural and synthetic. The mechanical properties of rubber are strongly dependent on the composition, fillers (such as carbon black or silica), temperature and loading conditions [44]. In general, rubber has a low elastic modulus, making it possible to deform under stress and recover to its original shape when unloading. This process allows fenders to absorb the kinetic energy of the vessel, reducing the risk of structural structural damage. The behavior of rubber is non-linear and viscoelastic. Rubber acts elastically in lower strains according to Hooke's law but hardens in larger strains where Hooke's law is no longer valid [61]. The non-linear stress strain curve as shown in Figure 3.1a of rubber can be explained with its molecular structure. The cross-linked polymer chains are stretching under tension, causing polymer chains to align and form crystalline regions as illustrated in Figure 3.1b. Furthermore, the strain rate significantly influences the stress response, higher strain rates leading to increased stiffness [20].

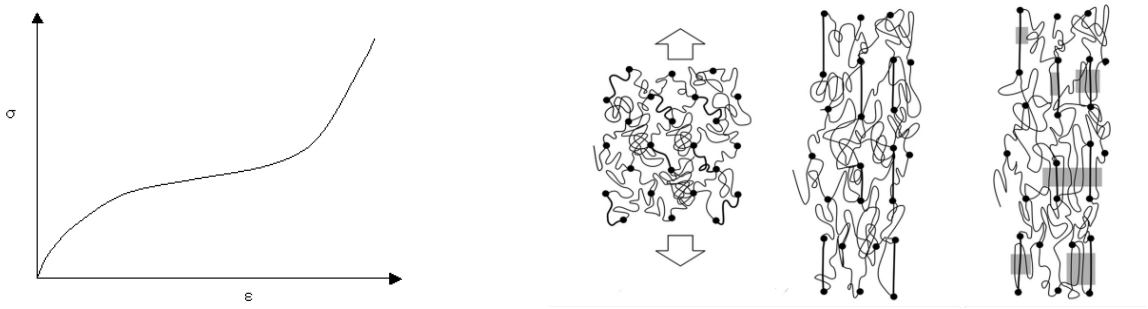

(a) Typical stress-strain curve of rubber [74]

(b) Strain-induced crystallization [23]

Figure 3.1: Mechanical behavior and microstructural response of rubber under strain

The Poisson ratio of rubber is approximately 0.5 as shown in Eq. 3.1 and rubber is nearly incompressible [72], meaning that the volume remains almost constant during compression due to the fact that the bulk modulus (K) is much greater than the shear modulus (G). In addition, natural rubber is isotropic but reinforcements can affect stiffness and may lead to anisotropic behavior.

$$\nu = \lim_{K \to \infty} \frac{3K - 2G}{2(3K + G)} = \frac{1}{2} \tag{3.1}$$

Viscoelastic (time-dependent) materials consist of two parts when subjected to an external force. The viscous part means that the material deforms gradually, and the elastic part means that the material returns to its original shape after the force is removed [12]. Viscoelastic materials have three key characteristics as shown in Figure 3.2. Hysteresis describes the difference between the loading and unloading curve which is the energy loss during one load cycle. Stress relaxation is the effect where stress decreases with time under constant strain. Creep on the other hand, is the increase in strain when the material is subjected to constant stress over time.

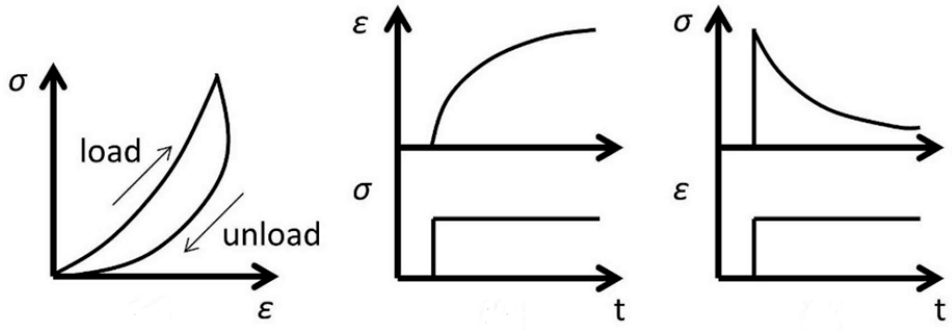

Figure 3.2: Viscoelastic behavior hysteresis, creep and stress relaxation [76]

The dynamic behavior of viscoelastic materials can be characterized with the complex modulus approach [57]. In most cases, there is a phase lag between stress and strain as illustrated in Figure 3.3a with a certain amount of energy lost. The real component of the Young's modulus is the storage modulus (E') which is the energy stored inside the material. The imaginary viscous part can be quantified with the loss modulus (E") which takes the internal friction into account. Finally, the ratio between the loss modulus to storage modulus can be defined, which is known as the loss tangent. These relations are shown in Eq. 3.2.

$$E^* = E' + iE'', \quad E' = \left(\frac{\sigma_0}{\varepsilon_0}\right)\cos\delta, \quad E'' = \left(\frac{\sigma_0}{\varepsilon_0}\right)\sin\delta, \quad \delta = \tan^{-1}\left(\frac{E''}{E'}\right) \tag{3.2}$$

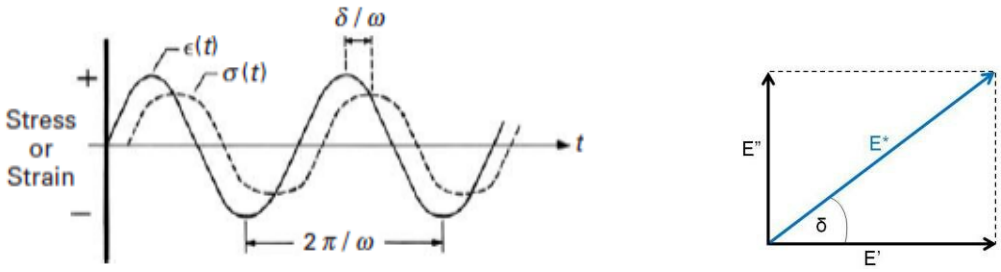

(a) Viscoelastic response with phase lag

(b) Loss tangent

Figure 3.3: Dynamic viscoelastic response with phase lag and loss tangent [57]

The magnitude of the storage and loss modulus is strongly related to frequency and temperature [82]. Figure 3.4 shows the effect of different temperatures and frequencies on the stiffness (storage) and damping (loss) of the shear modulus.

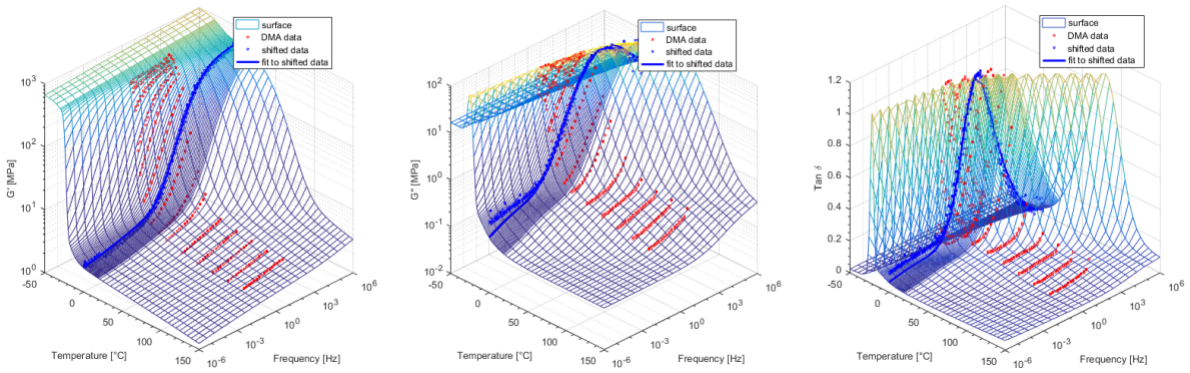

Figure 3.4: G', G" and tan (δ) for different temperatures and frequencies [57]

The time-dependent behavior of the shear modulus can be described with the Prony series in Eq. 3.3 [57]. Here is $G(t)$ representing the shear relaxation and g_i^p and τ_i^c are material constants with N being the number of relaxation times.

$$G(t) = g_0 \left[1 - \sum_{i=1}^{N} \bar{g}_i^p \left(1 - e^{-t/\tau_i^c} \right) \right] \tag{3.3}$$

3.1.2. Hyperelastic material models

Several hyperelastic models were developed to formulate the relationship between stress and strain with the strain energy function. Those models with the associated theory and assumptions will be explained in this subsection.

The deformation gradient tensor F in Eq. 3.4 is a method for quantifying the movement of an external body and is especially suitable for materials undergoing large deformations [10]. It describes how material points move from their initial state to the current configuration (deformed state). When $F_{ij} = \delta_{ij}$, there is no deformation but only a rigid body motion. If $\frac{\partial u_i}{\partial x_j} \neq 0$ the material undergoes some deformation, such as stretching, compression, or shear.

$$F_{ij} = \delta_{ij} + \frac{\partial u_i}{\partial x_j} \tag{3.4}$$

Commonly used measures for finite strains are the left (B) and right (C) Cauchy and Lagrange (E) material strain tensors, which are derived from the deformation gradient with matrix transformations as shown in Eq. 3.5. These transformations are essential in the finite strain theory and modeling of non-linear behavior of hyper-elastic materials.

$$C = F^T F \qquad B = F F^T \quad E = \frac{1}{2}(C - I) \tag{3.5}$$

Linear elastic materials follow a linear relationship in which the stress is proportional to the strain. For hyperelastic materials the stress-strain relationship is non-linear and depends on the strain energy function W, which represents the stored energy per unit volume as a function of deformation [45]. The relationship for the energetic stress is shown in Eq. 3.6 and can be expressed in terms of the right Cauchy and Lagrange strain tensor.

$$S = 2\frac{\partial W(C)}{\partial C} = \frac{\partial W(E)}{\partial E}. \tag{3.6}$$

The Cauchy stress could be calculated according to Eq. 3.7. Here is J_F the local volume change of an element. In practice assuming $J_F = 1$ (incompressibility) for rubber is reasonable and this term could

be neglected [66]. The Cauchy stress is used mainly in the deformed configuration, while the energetic stress is used more often in material models with an available strain energy function.

$$\sigma = J_F^{-1} F S F^T \tag{3.7}$$

Besides the Cauchy stress also known as the ”true stress”, it can sometimes be more practical to work with other stress measures [10]. These other stress measures include the Kirchhoff stress (Eq. 3.8) , the First Piola-Kirchhoff stress (Eq. 3.9) and the Second Piola-Kirchhoff stress (Eq. 3.10).

$$\tau = J_F \sigma \tag{3.8}$$

$$P = J_F \sigma F^{-T} \tag{3.9}$$

$$S = J_F F^{-1} \sigma F^{-T} \tag{3.10}$$

A well-known method to determine the finite strain is to use the principal extension ratios along the three perpendicular axis of the material. Consider a unit cube that is transformed into a rectangular having three unequal edge lengths as shown in Figure 3.5. The extension ratios (λ) may be greater than one, which corresponds to a stretch, or lower than one, which corresponds to a compression [72]. Assuming that the material is incompressible and therefore the volume remains constant, the condition in Eq. 3.11 must apply.

$$\lambda_1 \lambda_2 \lambda_3 = 1 \tag{3.11}$$

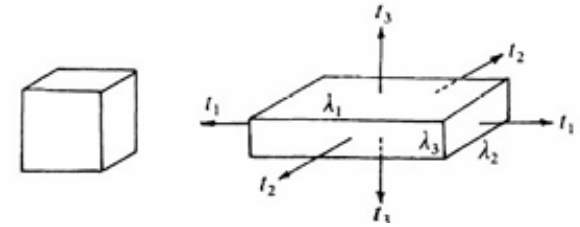

Figure 3.5: Unstrained state to strained state [72]

The right Cauchy deformation tensor C has three invariants, in terms of stretches this can be rewritten as Eq. 3.12. The first invariant measures the total stretch in all directions, the second invariant is related to shear deformations, and the third invariant is representing the volume changes and is equal to one in incompressible materials. The invariants form the basis of many hypereleastic material models which will be discussed below.

$$I_1 = \lambda_1^2 + \lambda_2^2 + \lambda_3^2 \quad I_2 = \lambda_1^2\lambda_2^2 + \lambda_2^2\lambda_3^2 + \lambda_3^2\lambda_1^2 \quad I_3 = \lambda_1^2\lambda_2^2\lambda_3^2 \tag{3.12}$$

Neo-Hookean

The Neo-Hookean model predicts the stress-strain behavior of rubber materials and is based on the first order [28] of the reduced strain energy function as shown in Eq. 3.13. The stress-strain relationship in the begin phase of rubber is linear but becomes non-linear at a certain point. The Neo-Hookean model is a simple model that represents the strain energy density function for an incompressible system [30] and is defined in Eq. 3.14. Here, C_i is the material constant, I_1 the first invariant of the left Cauchy-Green deformation tensor, D_1 the compressibility term and J the determinant of the deformation gradient. The Neo-Hookean model is based on statistics of cross-linked polymer chains. However,

when the chains are stretched to their maximum point, the elastic modulus will suddenly rise, which makes this model less suitable to predict accurately at higher strains.

$$W = \sum_{i=1}^{N} C_i(\bar{I}_1 - 3)^i + \sum_{i=1}^{N} \frac{1}{Di}(J-1)^{2i} \tag{3.13}$$

$$W = C_1(I_1 - 3) \tag{3.14}$$

Mooney-Rivlin
The Mooney-Rivlin model is an extension of the Neo-Hookean model. The strain energy function proposed from the Mooney-Rivlin model as shown in Eq. 3.15 is derived from a linear combination of two invariants of the Cauchy-Green left deformation tensor to account for hyperelastic, incompressible, isotropic, and non-linear behavior [38]. C_1 and C_2 are empirically determined material constants, and I_1 and I_2 the first and second invariants of the Cauchy-Green deformation tensor. This model can be used for components with medium strains [30] and allows a simple definition of quasi-static temperature dependence.

$$W = C_1(I_1 - 3) + C_2(I_2 - 3) \tag{3.15}$$

Ogden
The Ogden [50] model is an hyper-elastic model that predicts the stress-strain behavior of a rubber material, using the principal stretch ratios (λ) and material constants (μ, α) as shown in Eq. 3.16. Unlike Neo-Hookean or Mooney-Rivlin, this model does not require the invariants, making the model flexible and suitable for data fitting. The Ogden model is particularly useful in applications with large deformations and high accuracy. However, Ogden does not take finite-chain extensibility into account, which makes it less suitable in applications with extreme strain stiffening.

$$W = \sum_{i=1}^{N} \frac{\mu_i}{\alpha_i}\left(\lambda_1^{\alpha_i} + \lambda_2^{\alpha_i} + \lambda_3^{\alpha_i} - 3\right) + \sum_{i=1}^{N} \frac{1}{D_i}\left(J-1\right)^{2i} \tag{3.16}$$

Arruda-Boyce
The Arruda-Boyce [4] model is also called the eight-chain form and is based on the deformation of the elastomer's microstructure. The Arruda-Boyce model consists of a volume element which is made up of eight chains stretching from the center to each corner. The strain energy function according to Arruda-Boyce is given in Eq. 3.17. The values of coefficients C_1 to C_5 arise in the statistical treatment of the non Gaussian chains. The locking stretch λ, is the stretch at which the slope of the stress strain curve will increase significantly. The initial shear modulus μ_0 is related to μ with the relation in Eq. 3.18.

$$W = \mu \sum_{i=1}^{5} \frac{C_i}{\lambda^{2i-2}}(I_1^i - 3^i) + \frac{1}{D}\left(\frac{J^2-1}{2} - \ln J\right) \tag{3.17}$$

$$\mu_0 = \mu\left(1 + \frac{3}{5\lambda^2} + \frac{99}{175\lambda^4} + \frac{513}{875\lambda^6} + \frac{42039}{67375\lambda^8}\right) \tag{3.18}$$

$$\begin{aligned} C_1 &= \frac{1}{2} & C_2 &= \frac{1}{20} & C_3 &= \frac{11}{1050} \\ C_4 &= \frac{19}{7000} & C_5 &= \frac{519}{673750} \end{aligned} \tag{3.19}$$

3.1.3. Viscoelastic material models

Rubber is a viscoelastic material which results in time-dependent responses such as stress relaxation, creep, and hysteresis. In this subsection, both linear and nonlinear models that are able to describe this viscoelastic behavior will be discussed.

Linear models

Linear viscoelastic models assume small deformations and a linear stress-strain relationship. In addition, these models are not including damage from previous applied loads. Linear viscoelastic models that are widely used are the models of Maxwell, Kelvin-Voigt, and Zener.

Maxwell

The Maxwell model is able to simulate a linear viscoelastic model using a spring and a damper connected in series. The spring represents the elastic deformation with Hooke's law, and the damper accounts for the viscous (η) effect using Newton's law. This model can effectively describe the stress relaxation effect under constant strain.

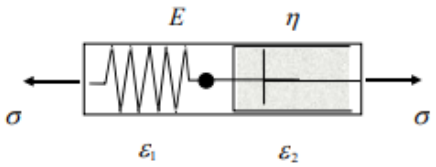

Figure 3.6: Maxwell model schematic [29]

$$\frac{d\varepsilon}{dt} = \frac{1}{E}\frac{d\sigma}{dt} + \frac{1}{\eta}\sigma \tag{3.20}$$

Kelvin-Voigt

The Kelvin-Voigt model uses the same elements as the Maxwell model, but here, the elements are connected in parallel instead of in series. This formulation can describe the phenomenon of creep under constant stress, where the strain increases until it reaches a certain limit.

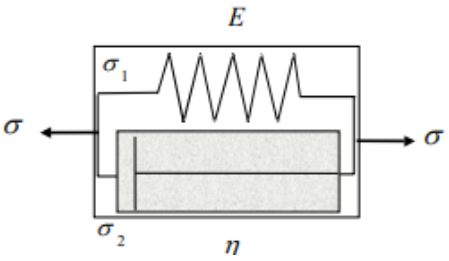

Figure 3.7: Kelvin-Voigt model schematic [29]

$$\frac{d\varepsilon}{dt} + \frac{E}{\eta}\varepsilon = \frac{1}{\eta}\sigma \tag{3.21}$$

Standard linear model (Zener)

The standard linear model, also known as the Zener model combines the features of Maxwell and Kelvin-Voigt to describe the material behavior more accurately. This model can represent both creep and stress relaxation behavior.

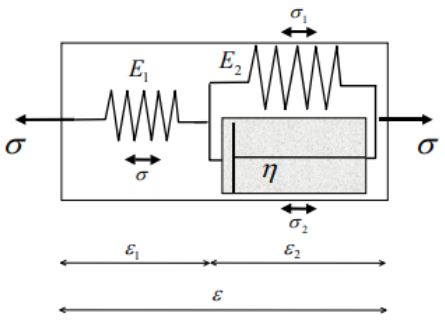

Figure 3.8: Zener model schematic

$$\sigma + \frac{\eta}{E_1 + E_2}\frac{d\sigma}{dt} = \frac{E_1 E_2}{E_1 + E_2}\varepsilon + \frac{E_1 \eta}{E_1 + E_2}\frac{d\varepsilon}{dt} \tag{3.22}$$

Nonlinear models

The models mentioned above assume a small deformation where the strain is proportional to the stress and the storage and loss modulus are independent of the strain amplitude. Second, the strain caused by a load currently applied should be independent of any previous load. When one of these conditions is violated, non-linear viscoelastic models are required to describe its behavior. Two examples that can describe this behavior are the models of Bergström–Boyce and Schapery.

Bergström–Boyce

The Bergström–Boyce [9] model is able to combine a hyperelastic network with a parallel time and rate-dependent viscoelastic network. This model is a micro mechanism inspired constitutive model, and commonly called the BB model. The BB model can describe large strain behavior of elastomers, while taking into account the frequency, temperature, stress relaxation, creep and hysteresis dependency. By combining the BB model with a Mullins effect (discussed in subsection 3.2.2) model, it is found that the complete behavior of elastomers can be predicted. In Abaqus [15] this is worked out in a parallel rheological framework that can simulate the non-linear viscoelastic behavior. The main principle in this framework is that the behavior is modeled separately. In Eq. 3.23 the BB model is shown. Here are A,E, C and m material parameters and $\dot{\bar{\varepsilon}}^{cr}$, λ^{cr} and $\bar{q}$ the creep strain rate, extension ratio and deviatoric Kirchhoff stress, respectively.

$$\dot{\bar{\varepsilon}}^{cr} = A\left(\lambda^{cr} - 1 + E\right)^{C}\left(\bar{q}\right)^{m} \tag{3.23}$$

Schapery

The non-linear viscoelastic Schapery [62] model takes the influences of high stress levels, temperature, aging and other circumstances into account via non-linear equations based on the Boltzmann's superposition principle [39]. This model is formulated in an intergral (1D) formulation in Eq. 3.24 which is powerful but mathematically complex.

$$\varepsilon(t) = g_0(t)D_0\sigma(t) + g_1(t)\int_{0^-}^{t}\Delta D(\psi - \psi^{\tau})\frac{d}{d\tau}\left[g_2(\tau)\sigma(\tau)\right]d\tau \tag{3.24}$$

Here, g_0, g_1 and g_2 are the stress dependent parameters and D the creep compliance. The reduced time ψ can be defined as follows:

$$\psi(t) = \int_0^t \frac{1}{\alpha_\sigma[\sigma(s)]\,\alpha_T[T(s)]}\,ds \tag{3.25}$$

where α_σ and α_T are the time shift factors due to the stress and temperature. In the case where g_0=g_1=g_2=α_σ=α_T=1, this leads to the linear variant with the Boltzmann's superposition principle.

3.2. Physical mechanisms causing reduction in stiffness rubber

Several mechanisms contribute at the same time to the reduction of the stiffness of rubber, especially with cyclic loading. These mechanisms will be discussed and explained in this section.

3.2.1. Payne effect

The nonlinear decrease in the storage modulus (stiffness) with increasing strain amplitude is called the ”Payne effect” with typical strain ranges from 0.1% to 10%. This phenomenon can be explained by the reversible breakdown of physical networks with filler interactions such as carbon black or silica [68]. When the strain amplitude increases, these interactions become disrupted resulting in a decrease in stiffness. Rubbers with a high amount of fillers tend to show more non-linearity due to filler networking, resulting in more internal friction. In cyclic loading conditions this aspect is contributing to hysteresis and heat build up. In Figure 3.9 the curves of the stiffness and damping are shown in the Payne effect range. In the beginning phase, the rubber is stiff with low-energy dissipation. When the networks are breaking, the stiffness drops and the damping increases until a certain limit.

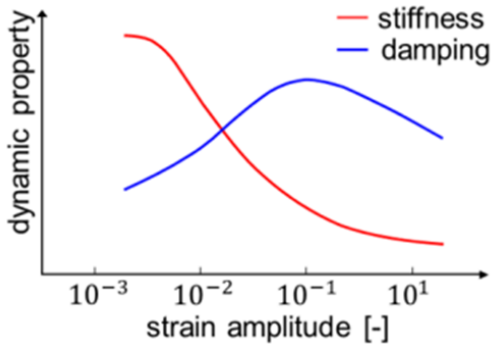

Figure 3.9: Payne effect [55]

3.2.2. Mullins effect

The Mullins effect as shown in Figure 3.10a is about stress softening of an elastomer, especially during the first few loading cycles, resulting in a decrease in stiffness and an increase in hysteresis [72]. When the material is loaded for the first time, it follows the path a-b-b’ with unloading path b’-B-a. If the material is reloaded, it follows the softening path a-B-b’ in an ideal Mullins effect representation where the hysteresis is neglected with the exception of the first loading cycle. Although the Payne effect occurs at smaller strains, the Mullins effect occurs at larger strains. In addition, the Mullins effect is non-reversible and path dependent, meaning that the behavior of the elastomer after the first time of straining can not be reproduced anymore, unless a long resting time (more than one week). The Mullins effect is caused by changes within the microstructure of the elastomer. These include bond rupture, molecules slipping, filler rupture and disentanglement as shown in Figure 3.10b [52]. Elastomers with a large amount of added fillers are more exposed to the Mullins effect because of the increased number of bonds available for breakage. Furthermore, the degree of stress softening depends on the amplitude of the strain. Large strain amplitudes cause more microstructure damage, resulting in a greater reduction in stiffness. In addition, the loading rate, temperature and type of filler influence the Mullins effect as well. FEA software such as Abaqus can incorporate the Mullins effect by using a damage variable with the Ogden-Roxburgh [51] formulation, as shown in Eq. 3.26. Here are r,m and β material parameters and W_m and W_0 the maximum strain energy potential and the threshold strain energy, respectively.

$$\eta = 1 - \frac{1}{r}\,\mathrm{erf}\left(\frac{W_m - W_0}{m + \beta W_m}\right) \tag{3.26}$$

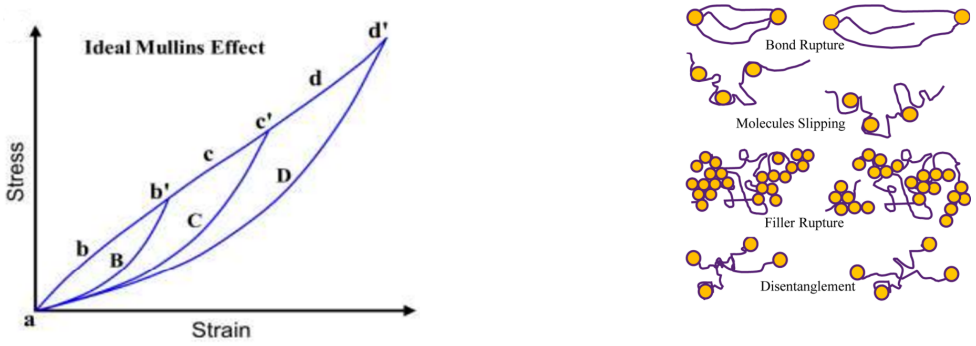

(a) Mullins effect [81]

(b) Types of bond failures [52]

Figure 3.10: Mullins effect in rubber with associated microscopic bond failures

3.2.3. Residual deformation and delayed elastic strain

Residual deformation is the permanent set of strain remaining in the rubber in the unloaded situation [11]. Often, when a rubber specimen is first stretched to a high strain, the specimen does not fully recover to its original length because a part of the deformation has become permanent or delayed due to the viscoelastic properties. Typically, this is associated with the Mullins effect as shown in Figure 3.11. The permanent deformation arises because polymer chains have yielded or slipped and cannot fully come back to their initial configuration. Rubbers with more fillers are more sensitive to permanent deformation because of the increase in filler interactions. In the stress-strain curve, the new loading curve with a permanent set of strain is shifted over the axis of the strain. This will cause a reduction in overall stiffness when the zero-strain scenario is considered as reference point.

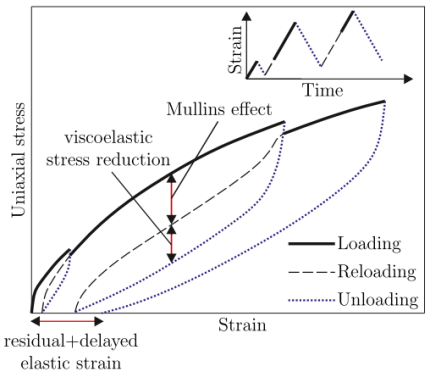

Figure 3.11: Cyclic load showing the viscous, the Mullins and the residual strain effects [19]

3.2.4. Hysteresis

Since rubber is a viscoelastic material, it dissipates a part of the energy in the form of heat. This energy can be calculated with the area between the loading and unloading curves in Figure 3.2 and is called hysteresis [25]. This phenomenon can be significant under high-frequency or high-strain cyclic loading conditions. When heat accumulates in the rubber, oxidative reactions occur, leading to a reduction in cross link density [36] and consequently to a reduction in stiffness as shown in Figure 3.12. Researchers have investigated the role of ambient temperatures on the behavior of rubber, but here the self-heating phenomenon is often neglected, and the relationship with the frequency is currently unknown. [71] [53]. Luo et al. [37] investigated the relationship between self-heating due to hysteresis and cyclic loading. He found that the temperature within the first cycles increased rapidly, after which the specimen kept its steady value for a prolonged period, which accounts for the majority of the life, and then suddenly increased until the specimen ruptured. The stiffness was not measured in this experiment.

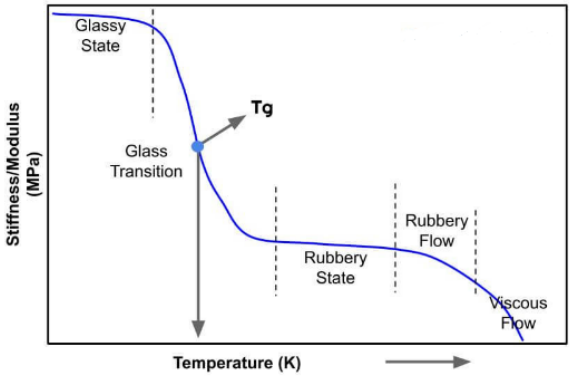

Figure 3.12: Temperature and stiffness of amorphous polymer with glass transition [54]

3.2.5. Micro structural changes

When a load is applied to a rubber sample, micro-cracks or voids can initiate in regions with high strains or material defects. In the beginning, these effects are small and do not affect the mechanical behavior, but when the number of cycles increases, they can expand to macroscopic cracks [53] illustrated in Figure 3.13. This effect will cause a reduction in the stiffness of the material and could eventually lead to failure due to fatigue. The type of rubber, either natural or synthetic, differ significantly in micro-cracking behavior. Natural rubber offers strong resistance as a result of the strain-induced crystallization effect, whereas synthetic rubber must rely on its initial strength. Due to the crystallization effect, an abrupt increase in stiffness could occur in NR after an intermediate number of cycles. In addition, cyclic loading can cause chain scission or cross-link breakage in the long term, resulting in a lower stiffness as well. Especially when environmental aging (oxygen, ozone, and UV) contributes simultaneously, this process will be accelerated [44].

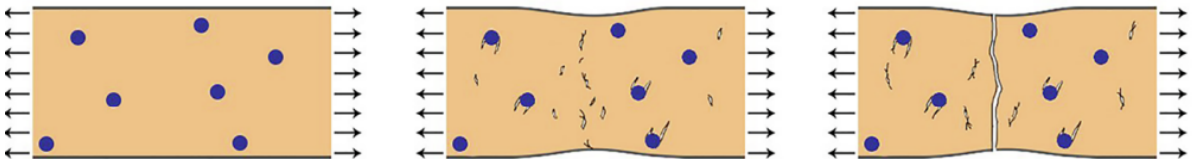

Figure 3.13: Schematics of the micro-structural damage evolution in rubber near particle content [13]

3.3. Rubber fatigue models

In the literature, there are two phases for the prediction of fatigue life in rubber: the crack initiation and the crack propagation method [71]. In the crack initiation approach, the end of life is experimentally defined as the appearance of a crack of a certain size based on stress, strain or energy history at a point in the material. When the initial crack position and shape are known, crack propagation could be used, which is based on tearing energy to get information about crack growth before failure. In this section, these two methods will be discussed.

3.3.1. Crack initiation

The crack initiation method was first performed by Wöhler. He used a number of cycles to evaluate fatigue life and drew the S-N curve (stress amplitude vs. cycles to failure), which is still used today [53]. In Figure 3.14 a typical example of an S-N curve based on strain is illustrated. Other commonly used parameters for predicting the fatigue life of a rubber component are stress and energy. According to Shangguan et al. [80] the crack initiation life of filled natural rubber accounts for more than 90% of its total life in uniaxial tensile fatigue tests. There are two assumptions in applying this crack initiation method. First, the rubber is isotropic and second, the rubber has no macroscopic cracks. Here, it is considered that the fatigue life follows a power law with its parameters. An example is shown based on strain in Eq. 3.27 with A and b being the material constants.

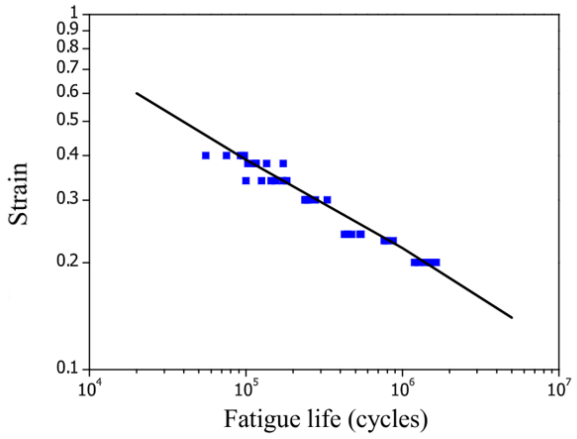

Figure 3.14: S-N curve of natural rubber based on strain [77]

$$N_f = A \cdot \epsilon^{-b} \tag{3.27}$$

Strain based
The strain is often used in experiments to predict the lifetime of a component. The main reason is that the strain could easily be measured from displacements [43]. In addition to the strain, the maximum principal strain is also widely used, which refers to the largest normal strain acting on a plane where the shear force is zero [53]. The direction of crack formation is most of the time perpendicular to the maximum principal strain direction. Li et al. [35] performed uniaxial fatigue tests with the maximum principal strain as the damage parameter, and the outcome of the prediction results was consistent with the experimental results. Shangguan et al. [80] performed the same tests with specimens of carbon black filled natural rubber and used prediction models based on principal strain, octahedral shear strain, and Green Lagrange strain. The predictions were all sufficiently accurate, but the Green Lagrange strain was found to be the most accurate. Kim et al. [31] concluded the same with the prediction of a diabolo specimen made of natural rubber. The results mentioned above were all based on uniaxial fatigue testing and in general accurately. However, Ro et al. [56] concluded that the maximum principal strain is not suitable for multi-axial loading of natural rubber. Ayoub et al. [6] validated this with styrene butadiene rubber in a load combination with tension and torsion.

Stress based
The stress-based method is also used to predict the fatigue life of rubber. Parameters such as the first and second invariants of the Cauchy stress tensor have been used, but their reliability was found to be doubtful, especially in the case with multi axial loading found by Saintier et al. [60]. Another method used the maximum principal stress as the damage parameter, the maximum principal stress showed good correlation with loading ratios equal to zero but failed for positive loading ratios. Saintier et al. concluded that this might be the result of the crystallization of filled natural rubber. G.Ayoub [7] investigated carbon filled styrene butadiene rubber using combinations of tension and torsion. The maximum principal stress successfully described the number of cycles until crack initiation for the uniaxial and multiaxial stress state.

Energy based
Among the energy-based prediction methods, the strain energy density (SED) is the most commonly used. The SED approach is a method for quantifying the amount of elastic energy stored per unit volume in the material. Under uniaxial loading conditions, this is a relatively straightforward method to make fatigue-life predictions [75]. However, under multiaxial loading Pan et al. [83] found that not all stored energy contributes to crack formation resulting in an underestimation of the predicted lifetime. Therefore, Mars et al. [71] came with the crack energy density (CED) approach, which takes only the energy into account that is available for the crack formation. CED considers the critical plane approach, making this method more suitable for multi axial loading. Zine et al. [84] compared this method with the

SED method based on experimental data from the literature consisting of uniaxial tension and torsion fatigue tests and concluded indeed that CED was making better predictions.

Micro-mechanisms crack initiation

Saintier et al. [58] investigated specimen surfaces using a field effect Zeiss scanning electron microscope equipped with dispersive spectroscopy analysis. The goal here was to identity micro-crack initiation mechanisms in natural rubber exposed to a cyclic load. Cracks were found to initiate in regions with pre-existing material faults also known as inclusions or agglomerates independent of the type of loading. Several initial voids were analyzed at the surface but non of the cracks were found to initiate from this areas. The most inclusions are caused by SiO_2 and $CaCO_3$ which are often added for process-ability. Agglomerates arise during the mixing process and often consist of carbon-black particles resulting in a local higher modulus. The formation of agglomerates is hard to avoid is the mixing process. Using the electron microscope, two different phenomena were found to occur near the crack based on the type of inclusion, namely decohesion and cavitation. Decohesion can relatively easy be observed with a microscope because the surface is free of rubber and was found dominant at stiff inclusions. The instantaneous void nucleation under a certain stress state is called cavitation and was found to occur in areas with agglomerates. The observation is that there is no clear interface between the agglomerate and the rubber that prevents stress relief through decohesion. As a result, local stresses increase until they reach the cavitation threshold. In this case cavitation is the dominant damage initiation mechanism.

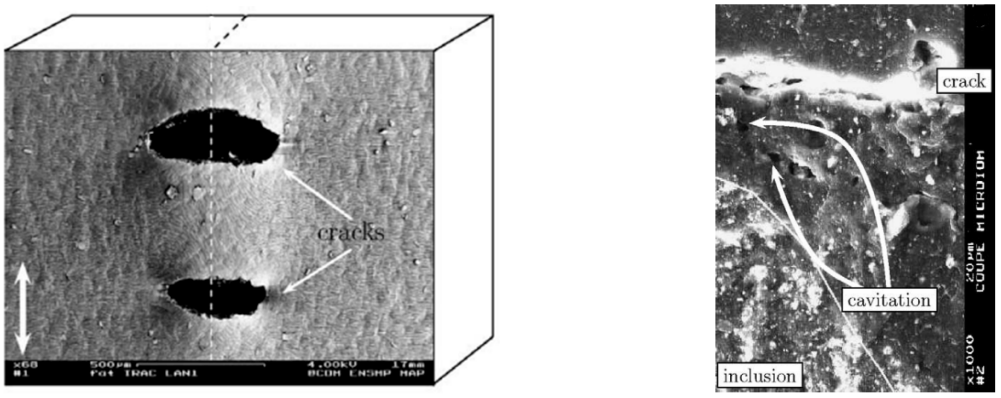

(a) Cracks in deformed configuration

(b) Inclusion and cavitation

Figure 3.15: crack initiation after a tension–compression test on a diabolo specimen [58]

3.3.2. Crack propagation

The crack propagation method is based on fracture mechanics and assumes that there are many tiny cracks in the rubber due to the production technology. The fatigue life here is defined as the number of cycles required for a crack to grow from the initial size to the maximum crack size based on the external energy release rate [53]. For a rubber the minimum energy required to grow a crack is the energy to break all the chains that cross the path of the crack. To specify this energy Lake and Thomas derived an expression for this crosslinking strength [26] as shown in Eq. 3.28.

$$T_0 = \left[\left(\frac{3}{8} \right)^{1/2} \rho A U \gamma^{1/2} L M_0^{-3/2} \right] M_c^{1/2} = K M_c^{1/2} \tag{3.28}$$

The tearing energy (T_0) in which crack growth is not affected by mechanical loading depends on the characteristics of the polymer. Namely the density(ρ), Avogadro's number (A), bond strength (U), chain stiffness (γ), bond length (L), molecular weight of a main chain bond (M_0) and the molecular weight between crosslinks (M_c). For a certain type of polymer, all characteristics are fixed, so this can be combined as a constant (K) with the exception of the molecular weight between cross-links. According to this theory, an illustration is given in Figure 3.16. First, the crack approaches the network chain

(blue line) between crosslinks (red dots). When the crack reaches the network chain, the chain will be stretched until it breaks, which allows the crack to go further in its path.

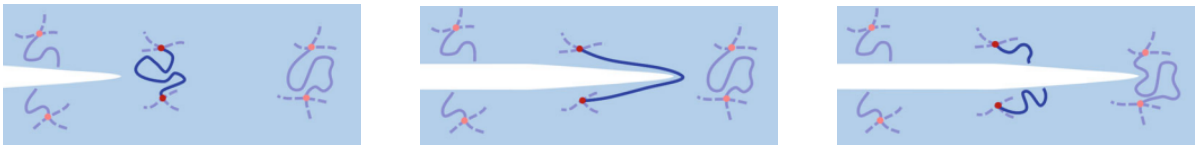

(a) Crack approaches chain **(b)** Network chain stretched **(c)** Network chain breaks

Figure 3.16: Different stages crack propagation [26]

Due to the large deformations of the rubber materials, an elastic crack could be observed under loaded conditions. In most cases, the crack propagation is in the orthogonal direction to the main stress. The strain energy release rate (potential energy decrease per unit crack area) is the parameter for crack growth. In the rubber literature, this is also called the tearing energy and can be defined as: [79]:

$$T = -\frac{\partial U}{\partial A} \tag{3.29}$$

Here, T is the tearing energy, U the elastic strain energy, and A the area of crack. Lindley and Thomas determined the crack propagation rate $\frac{da}{dn}$ versus the tearing energy for rubber materials. The relationship can be divided into four regions [66] with each of their own characteristics, as can be seen in Figure 3.17. The main challenge is to calculate the strain energy release rate with the associated crack and predict the growth path. In practice, this is often experienced as difficult.

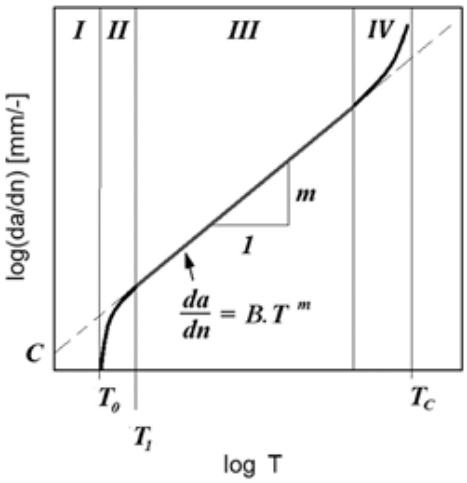

Figure 3.17: Logarithmic plot of crack growth rate [66]

When the value of the tearing energy is lower than T_0, the crack growth is equal to r due to aging and independent of repeated loading. Here is a the crack length and n the number of load cycles.

$$T \leq T_0 \implies \frac{da}{dn} = r \tag{3.30}$$

As the value of T exceeds T_0 the relation between the propagation rate and the tearing energy satisfies the following function:

$$T_0 \leq T \leq T_I \implies \frac{da}{dn} = A(T - T_0) + r \tag{3.31}$$

In region III the relationship between crack growth and tearing energy can be described with Paris & Erdogan power law where B and m are material constants. This region is mostly found in engineering problems.

$$T_i \leq T < T_c \implies \frac{da}{dn} = B \cdot \Delta T^m \tag{3.32}$$

Finally, the crack propagation is unstable and the crack propagation rate becomes infinite.

$$T \approx T_c \implies \frac{da}{dn} = \infty \tag{3.33}$$

3.3.3. Factors affecting fatigue life

There are several factors that influence the fatigue life of a rubber component. These factors include mechanical loads, rubber composition, and environmental conditions. This section explores how these parameters contribute to fatigue behavior.

Mechanical loads

The fatigue life of the rubber is strongly dependent on the type of mechanical load. Mechanical loads include tension, compression, torsion or a combination of them [53]. In fatigue tests, the influence of different loading situations could be investigated. The load ratio R represents the ratio of the minimum and the maximum stress or strain within a load cycle. Mohammed et al.[46] found based on experiments with natural and synthetic rubber that in fully relaxation conditions (R=0) a rise in strain leads to an increase in dissipated energy. The fatigue life could here be increased with lowering the maximum strain. Due to the strain crystallization a reinforcement effect occurred on the fatigue behavior with positive loading ratios (R>0). It was also found that fatigue life improves with increasing the minimum strain even when the maximum strain increases. In contrast, when R<0 the fatigue life was reduced for both rubbers. Furthermore, Ghosh [24] investigated the impact of different loading modes on fatigue behavior. Here it was found that the crack growth rate is significantly higher with pulse loading than under sinusoidal loading, due to the higher strain rates of pulse loading. The frequency of loading causes heat generation within the rubber as a result of energy dissipation. It was found that with a higher frequency the accumulation of heat cannot be released to the environment fast enough [23]. The higher temperature of the rubber leads to an increase in crack growth rate which reduces the fatigue life.

Rubber composition

Rubber offers a wide range of mechanical properties by varying the composition of the compound and the manufacturing process [20]. As discussed in section 2.3 fenders could me made from different compounds with each having their own mechanical properties. The main compounding factors that are known influencing fatigue behavior are polymer type, filler type, antioxidants and cross-linking agents [44]. Strain crystallization has some beneficial consequences on the fatigue performance of a rubber. In a rubber without strain crystallization crack growth can be significant under a static or dynamic load. Some examples of rubbers that undergo strain crystallization are natural rubber, isoprene rubber and poly-chloroprene. The filler carbon black is commonly used in the fender industry, which enhances the fatigue properties of rubber by minimizing the crack growth rate. [2]. Antioxidants protect rubber from environmental impacts (oxygen, ozone, and UV) and help against heat build-up due to hysteresis by decomposing hydro-peroxides [23]. Cross-linking agents are important in the vulcanization process because a higher cross-link density is associated with increased stiffness and reduced hysteresis, resulting in a longer fatigue life.

Environmental conditions

The environmental conditions are important for the rubber fatigue life, especially in the long term, and the fatigue life will be different in a different environment. Exposure to high temperatures will permanently age the rubber, showing a significant impact on fatigue life [23]. A higher temperature leads to an increased crack growth rate. The reason behind this is that less energy dissipated at high temperatures results in more energy available for crack growth for the same tearing energy [63]. This effect occurs even more in non-crystallizing rubbers as a result of the viscoelasticity effects. Most rubbers are exposed to the open air, so rubbers undergo chemical reactions with oxygen, which leads to a decrease in

mechanical properties and reduced resistance to fatigue [44]. In addition, exposure to ultraviolet (UV) radiation leads to a decrease in tensile and tear strength. At the same time ozone will also react with the rubber material leading to accelerated damaging. In some cases seawater is also involved in the degradation process. Narynbek [73] studied the performance of natural rubber through fatigue testing in seawater and compared it with fatigue in air. He found that in relaxed loading conditions they were almost the same, while under heavy loading conditions with large strain the fatigue life with seawater was longer than in air. This phenomenon can be explained by the fact that the thermal conductivity of seawater is higher than that of air, able to quickly reduce the temperature of rubber.

3.4. Conclusion literature review

Since rubber marine cone fenders are rupturing in some cases when subjected to cyclic loading, fatigue-related damage to rubber is a relevant aspect to investigate. To determine the fatigue life of rubbers, two approaches are commonly used, based on crack initiation and crack propagation. The crack initiation methods could be divided into stress, strain and energy based approaches. From the literature, it can be concluded that the most suitable damage parameter for crack initiation in uniaxial loading depends on the specific compound used and the applied loading ratio, since many researchers use different damage parameters [53]. Furthermore, when the crack initiation position is known, crack propagation methods could be used to obtain information about the crack growth before failure. The main challenge here is to predict the path of the crack and calculate the tearing energy (energy release rate) associated with the crack [53]. Moreover, the crack initiation life represents 90% of its total fatigue life in uniaxial tension testing [80], making it the most practical approach to focus on. However, multiaxial fatigue predictors are still quite new in the literature and only a few researchers such as Mars et al. [42] and Saintier et al. [60] have investigated this. Since rubber components often experience multiaxial stresses, this might be important to consider when making a prediction of the service life of a cone fender. In addition, it is important to realize that the fatigue life of rubber is strongly influenced by exposed environmental conditions, such as temperature, UV radiation, and ozone [73].

Determining the service life of rubber marine cone fenders is not straightforward, since multiple factors affect the fatigue life. The most suitable damage parameter for crack initiation is highly dependent on the specific compound and the loading ratio. The loading ratio within the cone fender is not constant throughout the compression cycle and may differ depending on the location within the cone fender. Local stresses influenced by the geometry result in fatigue damage in different regions. Moreover, the frequency of the cyclic load may cause residual deformation due to delayed strain, especially at higher frequencies. In addition, the loading velocity influences the strain rates within the cone fender, and that impacts the stress states affecting crack initiation. Taken together, a compressive approach is required that takes into account all these aspects. In the thesis, these aspects will be explored in detail, with the aim of making reliable predictions of the service life of rubber marine cone fenders under cyclic loading conditions.

4

Experimental tests lab Delft University of Technology

In this chapter, the rubber tests performed at Delft University of Technology are discussed together with the methodology used. Furthermore, the results are explained, and a material model is fitted based on these results.

4.1. Uniaxial tension and compression

Uniaxial tension and compression tests were performed in the Delft University laboratory to characterize the stress strain relations of the specific rubber compound used in cone fenders. The dumbbell specimens for tension, and cylindrical specimens for compression were obtained from Trelleborg and are according to the ISO 815-1 standard. The cylindrical specimen measured a height of 12.5 millimeters and 29 millimeters in diameter. The tension specimen followed a dumbbell geometry with a gauge length of 33 millimeters and a width of 6.2 millimeters in the narrow section. Additional dimensions can be found in the technical drawing in Figure 10.1. In uniaxial tension and compression illustrated in Figure 4.1, the specimen is loaded along one axis and the principal stretch ratios orthogonal to this axis will be similar. For incompressible rubber, the deformation gradient is equal to Eq. 4.1 in this case.

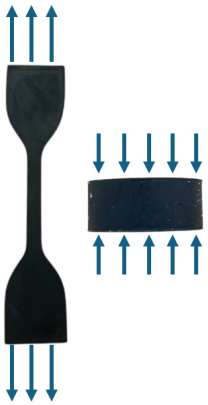

Figure 4.1: Uniaxial compression and tension forces on specimens

$$F = \begin{pmatrix} \lambda & 0 & 0 \\ 0 & \frac{1}{\sqrt{\lambda}} & 0 \\ 0 & 0 & \frac{1}{\sqrt{\lambda}} \end{pmatrix} \tag{4.1}$$

4.1.1. Test plan and setup

In total, three uniaxial tension and three uniaxial compression tests were performed at different engineering strain rates with each factor ten in between. The mechanical response of the rubber is rate dependent due to the viscoelastic properties of the rubber. The goal was to gain insight into the change in mechanical response. To ensure redundancy, each test was repeated three times, after which the average was taken per test. Both the uniaxial compression tests and the uniaxial tension tests were carried out on the Instron 8801 servo-hydraulic machine. For uniaxial tension self-fabricated steel plates were used tightened with 16 bolts to secure the dumbell-shaped specimens. Here, an additional 150 N load cell was used to measure the force during the uniaxial tension tests. During compression tests, standard Instron compression plates could be used, including the 100 kN load cell located inside the Instron. In Figure 4.3 the experimental tension and compression setup is shown in their initial (unstrained) and final (fully strained) configuration.

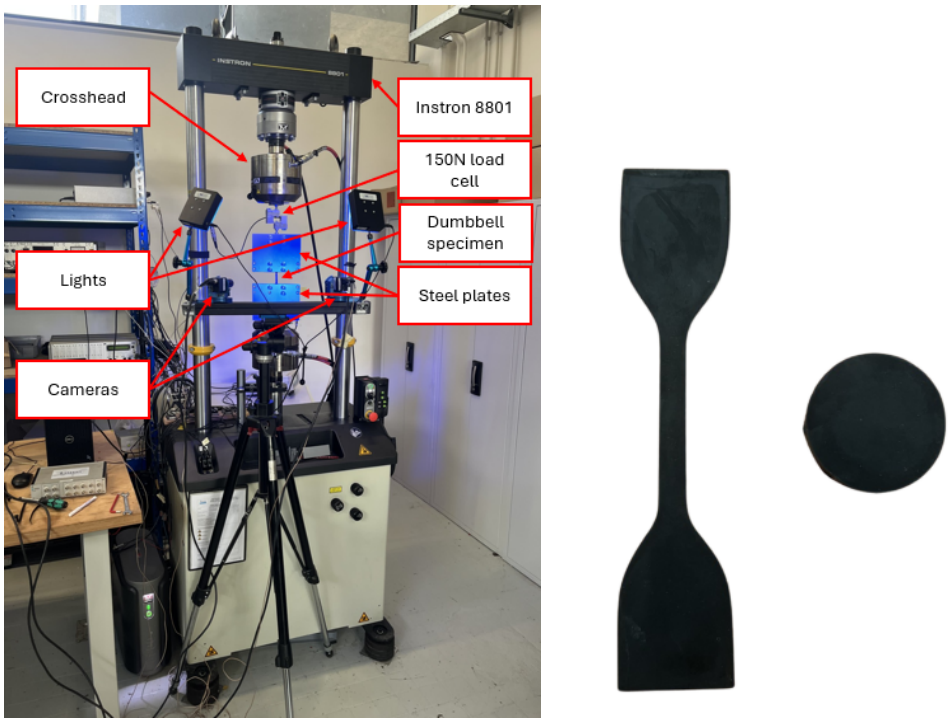

(a) Instron 8801 servo-hydraulic test setup **(b)** Specimens used (ISO 815-1)

Figure 4.2: Experimental setup and specimen types used in rubber tests at Delft University of Technology

The following test parameters in Table 4.1 and Table 4.2 were determined in advance of the experiments. The engineering strain rate was calculated using Eq. 4.2. Note that L_0 and L_1 correspond to the length in the undeformed and deformed configurations, respectively. In uniaxial compression tests L_0 corresponds to the height of the cylindrical specimen, whereas L_0 for uniaxial tension corresponds to the length of the gauge length of the dumbbell-shaped specimen.

Table 4.1: Test parameters for uniaxial tension

Test	Engineering strain (-)	Strain rate (1/s)	Absolute crosshead distance (mm)	Duration (s)	Absolute crosshead velocity (mm/s)
1	3.8	0.01	125.4	380	0.33
2	3.8	0.1	125.4	38	3.3
3	3.8	1	125.4	3.8	33

Table 4.2: Test parameters for uniaxial compression

Test	Engineering strain (-)	Strain rate (1/s)	Absolute crosshead distance (mm)	Duration (s)	Absolute crosshead velocity (mm/s)
4	-0.38	-0.01	4.75	38	0.125
5	-0.38	-0.1	4.75	3.8	1.25
6	-0.38	-1	4.75	0.38	12.5

$$\dot{\varepsilon}_{eng} = \frac{d\varepsilon_{eng}}{dt} = \frac{v}{L_0} \tag{4.2}$$

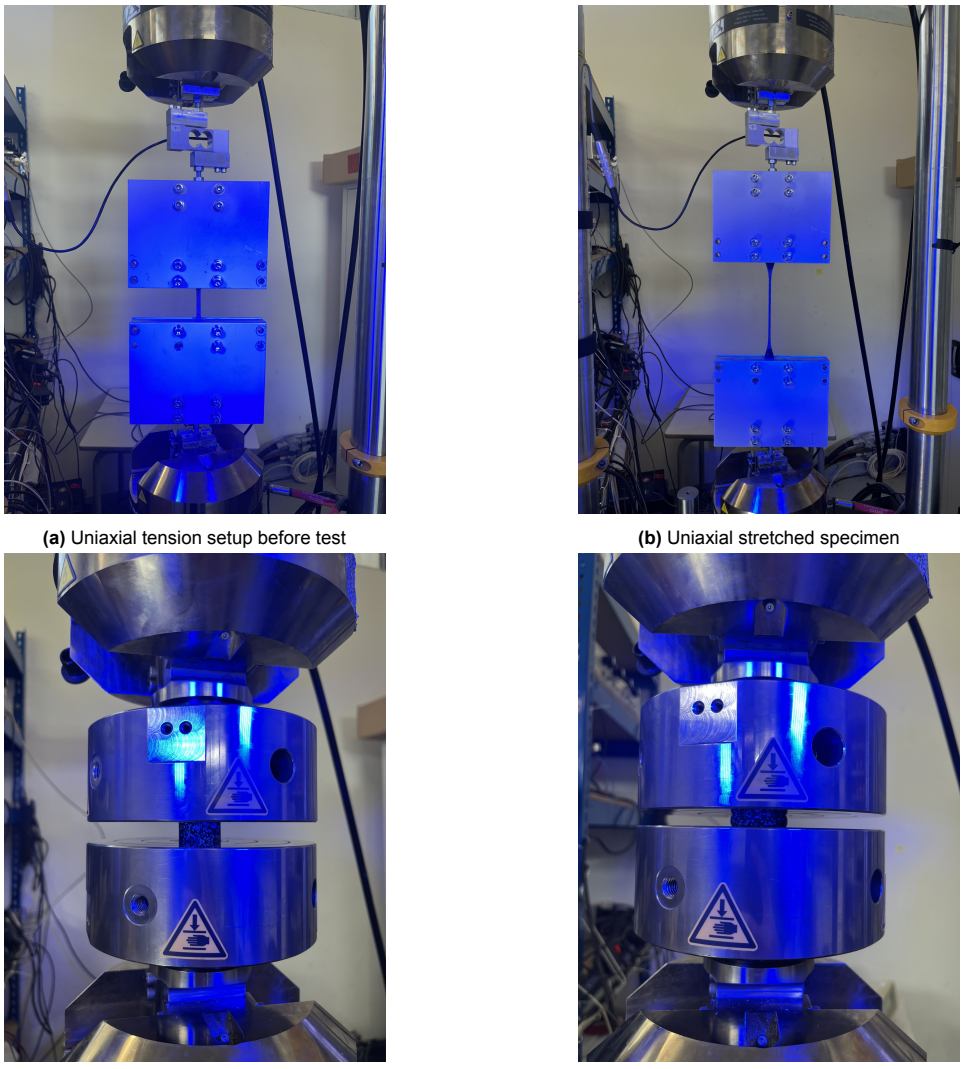

(a) Uniaxial tension setup before test

(b) Uniaxial stretched specimen

(c) Uniaxial compression setup before test

(d) Uniaxial compressed specimen

Figure 4.3: Uniaxial tension and compression setup Delft University of Technology

Digital image correlation (DIC) was used to measure displacements on the surface of the specimen during the tests. Digital image correlation is a non-optical measuring technique that determines strain based on tracking the surface displacement captured from sequential images. This technique offers significant advantages over traditional point-based instruments because it provides deformation across the whole surface. During the experiments two LIMESS cameras were used which were able to track the displacement of the white points in 3D located on the surface of the specimen. The speckle pattern was applied to the surface of the specimen with white spray paint. Based on the Pythagorean theorem,

the engineering strain based on the DIC displacements was determined. Because the uniaxial tension setup is less rigid compared to the uniaxial compression configuration, and given that the region of interest with uniaxial tension is only the gauge length. The strain in uniaxial tension was determined using DIC as previously discussed. For the uniaxial compression setup, the strain was derived from the crosshead displacement since no distinct gauge length is present. Here, DIC measurements were only used for verification purposes. The DIC technique applied on uniaxial tension and compression specimens is shown in Figure 4.4 during the experiment.

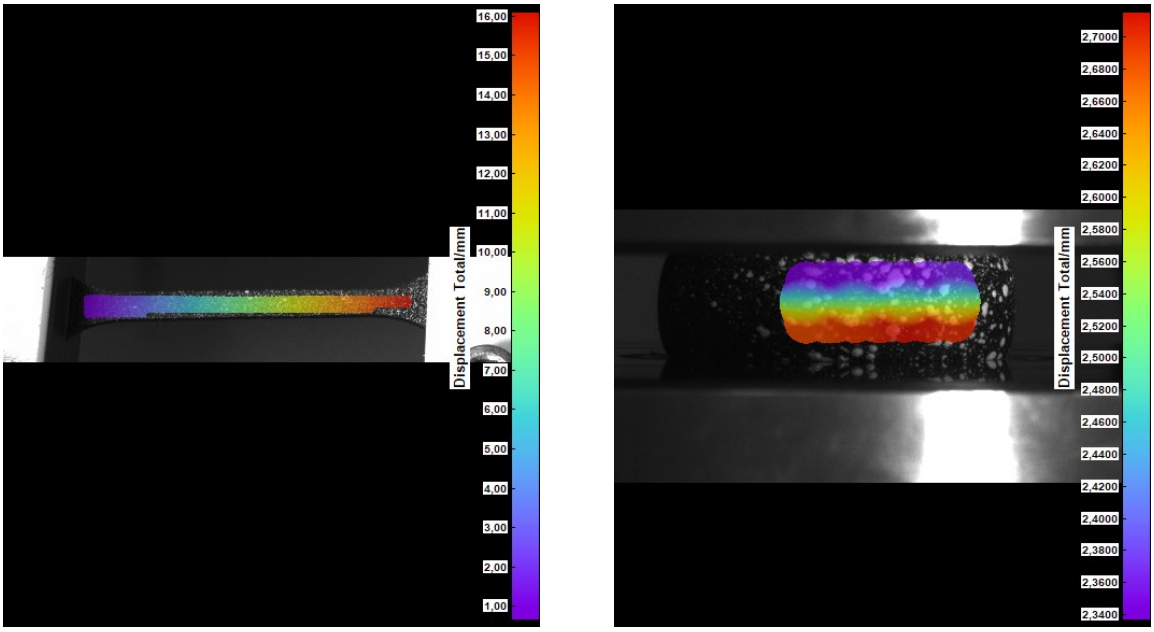

(a) DIC uniaxial tension

(b) DIC uniaxial compression

Figure 4.4: DIC used on specimens experimental setup

4.1.2. Stress strain relationship uniaxial tension and compression

Based on the force measurement by the 150 N load cell for uniaxial tension and the 100 kN load cell for uniaxial compression, the engineering strain for the uniaxial tension was derived from DIC measurements while for uniaxial compression it was based on the crosshead displacement resulting in a engineering stress-strain relation shown in Figure 4.5a and Figure 4.5c. The engineering stress was calculated using the original cross-sectional area of the material. Because large deformations occur in the experiments, it is more convenient to take advantage of the true stress and strain. The true stress is calculated using the instantaneous cross-sectional area. The true stress strain relation is shown in Figure 4.5b and Figure 4.5d. It is important to note that the engineering strain measured with DIC during uniaxial tension was exactly half the value given in Table 4.1 based on crosshead displacement. The ends of the dumbbell-shaped specimen are also straining, leading to an overestimation of the strain when relying on crosshead displacement. This observation emphasizes the advantage of measuring strain using DIC with large deformations in the gauge length. The rate-dependent behavior of the rubber compound is clearly illustrated in Figure 4.5. Under uniaxial compression , the true stress at a true strain of -0.4 corresponding to a engineering strain rate of 1.0/s is approximately 42% lower compared to the slower engineering strain rate of 0.010/s. This highlights the significant influence of the strain rate on the mechanical response of the tested rubber.

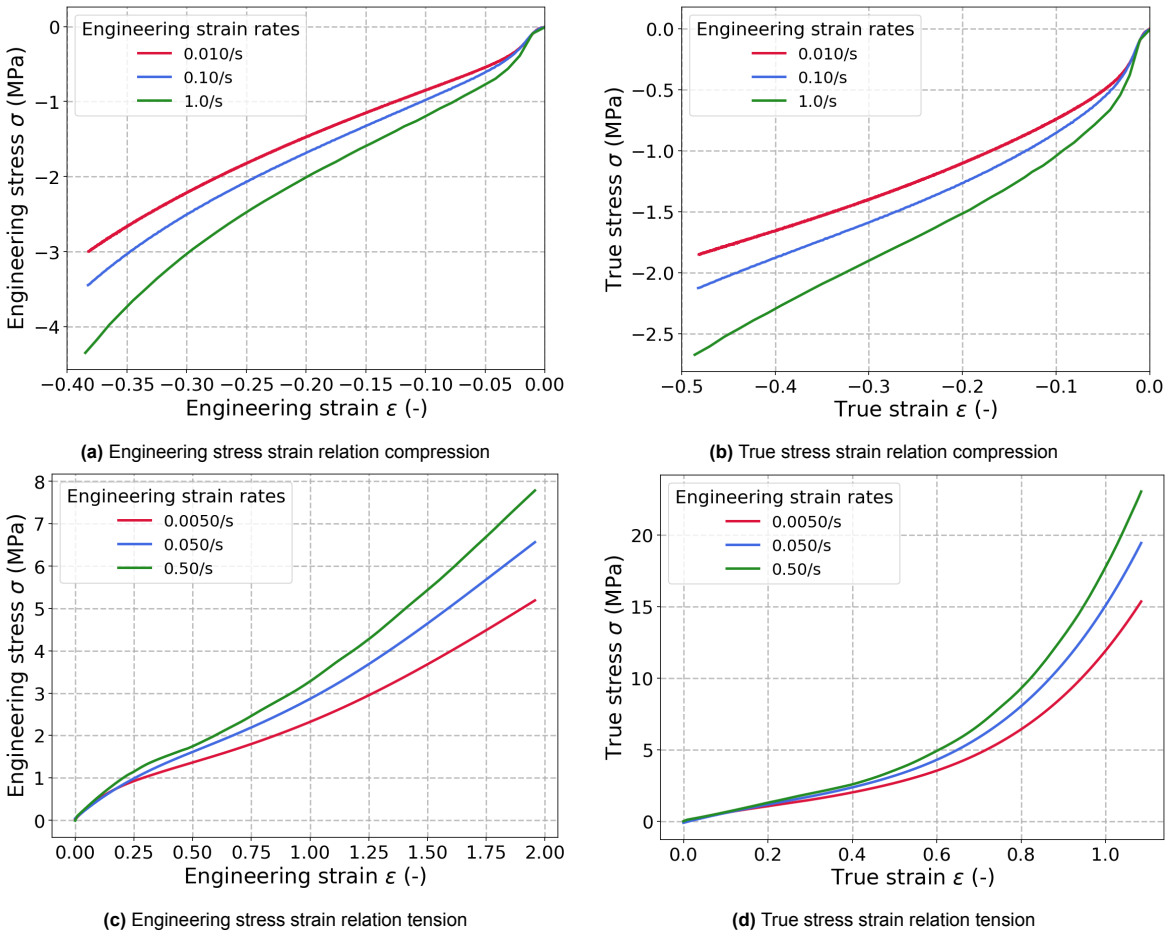

(a) Engineering stress strain relation compression

(b) True stress strain relation compression

(c) Engineering stress strain relation tension

(d) True stress strain relation tension

Figure 4.5: Uniaxial tension and compression experimental results

4.2. Determination of parameters in the hysteresis material model

The hysteresis material model is an advanced model for predicting non-linear, time-dependent, and large-strain behavior of elastomers. The response of elastomers can be represented using two parallel networks illustrated in Figure 4.6. Network A is a non-linear hyperleastic network modeled as a spring, and network B consists of a non-linear hyperelastic network in series with a non-linear viscoelastic component, modeled as a dashpot. The hystersis material model is implemented in Abaqus [15] under the suboption *HYSTERESIS.

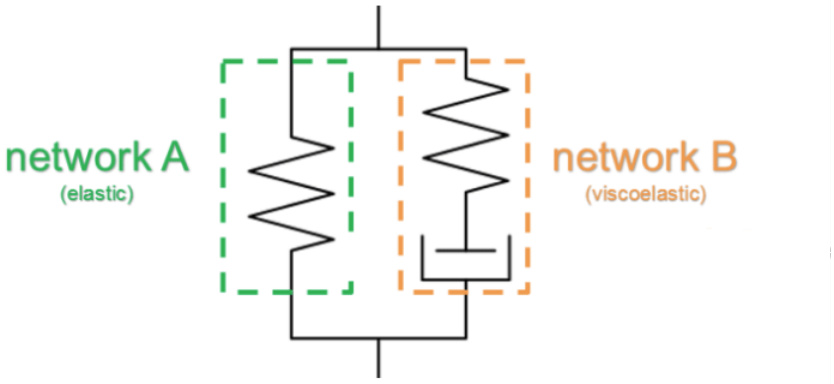

Figure 4.6: The parallel rheological framework schematic concept [65]

The applied deformation gradient acts on both networks according to Eq. 4.3. The deformation gradient that acts on network B could be further divided into elastic and viscoelastic components.

$$F = F_A = F_B \tag{4.3}$$

$$F_B = F_B^e \, F_B^{cr} \tag{4.4}$$

The material model consists of the following parameters and network interactions:

- An isotropic hyperelastic model describes the equilibrium response of network A.
- A stress scaling factor S, that describes the stress ratio carried by network B to that carried by network A under identical elastic stretching.
- A positive exponent m, in general greater than one characterizing the effective stress dependence of the effective creep strain rate in network B.
- An exponent C in the range of [-1,0], characterizing the creep strain dependence of the effective creep strain rate in network B.
- A scaling constant A, in the expression for the effective creep strain rate to maintain dimensional consistency in the equation.
- A constant E, in the expression for the effective creep strain rate, this constant regularizes the creep strain rate near the undeformed state.

The response of network A with the imposed deformation gradient F is governed by hyperelasticity. The stress dependence on network B is only dependent on F_B^e and governed by the same hyperelastic potential as network A with the stress scaling factor S. For a given F, the determination of F_B^e requires a constitutive relation for F_B^{cr} given in Eq. 4.6.

$$\sigma^B = S\sigma^A(F_e^B) \tag{4.5}$$

$$F_B^e \, \dot{F}_B^{cr} \, {F_B^{cr}}^{-1} \, {F_B^e}^{-1} = \dot{\varepsilon}_B^{cr} \left(\frac{S_B}{\sigma_B} \right) \tag{4.6}$$

Here is $\dot{\varepsilon}_B^{cr}$ the effective creep strain rate in network B and S_B the Cauchy stress deviator tensor in network B. The effective stress in network B and the effective creep strain rate are given by the following expressions in Eq. 4.7 and Eq. 4.8 respectively.

$$\sigma_B = \sqrt{\frac{3}{2} \, S_B : S_B} \tag{4.7}$$

$$\dot{\epsilon}_B^{cr} = A \left[\lambda_B^{cr} - 1 + E \right]^C (\sigma_B)^m \tag{4.8}$$

Where, $\lambda_B^{cr} - 1$ is the nominal creep strain in network B and λ_B^{cr} the chain stretch in network B expressed in Eq. 4.9

$$\lambda_B^{cr} = \sqrt{\frac{1}{3} \, I : C_B^{cr}} \tag{4.9}$$

Where, C_B^{cr} is given in Eq. 4.10.

$$C_B^{cr} = {F_B^{cr}}^T \cdot F_B^{cr} \tag{4.10}$$

4.2.1. Fitting material models

Several hyperelastic models like Neo-Hookean, Ogden and Arruda-Boyce discussed in subsection 3.1.2 were used as network A to fit the experimental data using the Mcalibration software package [27]. The Levenberg-Marquardt Algorithm (LMA) is implemented according Eq. 4.11 [22] in MCalibration to fit the experimental data. Here, the variable J represents the local sensitivity function ($\frac{\partial \hat{y}}{\partial a}$), describing how the parameters influence the predicted values. W, serves as the weighting matrix, also known as the inverse of the measurement error. λ, being the damping coefficient that helps unsure stability. h_{lm}, serves as the update step that results in parameter adjustments and y and $\hat{y}$ being the data points and predicted values of the model, respectively. This LMA is developed for solving nonlinear least squares problems and consists of two numerical optimization algorithms, the gradient descent method and the Gauss-Newton method. When the parameters are far from the optimal value, the LMA acts more like the gradient descent method and acts more like the Gauss-Newton method when the parameters are close to the optimal value with smaller values of the damping coefficient.

$$\left[J^{\mathrm{T}} W J + \lambda \operatorname{diag}(J^{\mathrm{T}} W J)\right] h_{\mathrm{lm}} = J^{\mathrm{T}} W (y - \hat{y}) \tag{4.11}$$

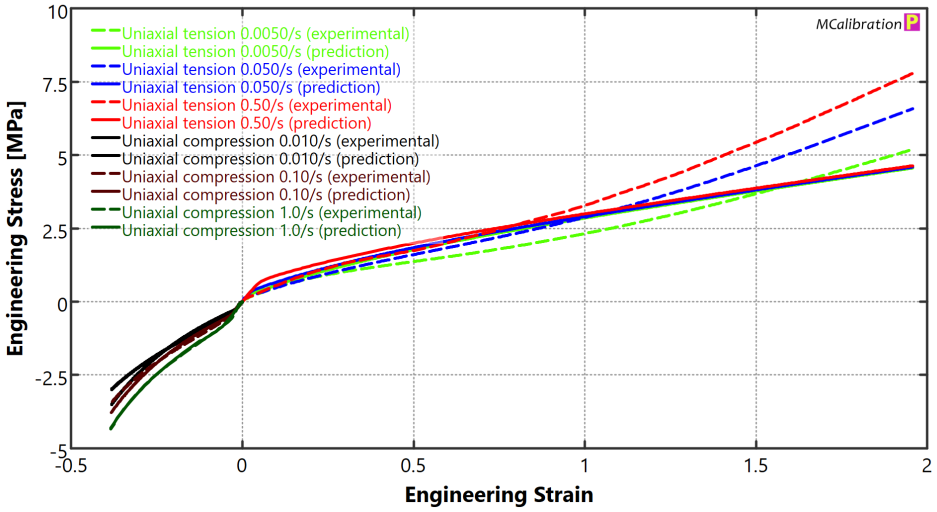

(a) Neo-Hookean as hyperelastic network

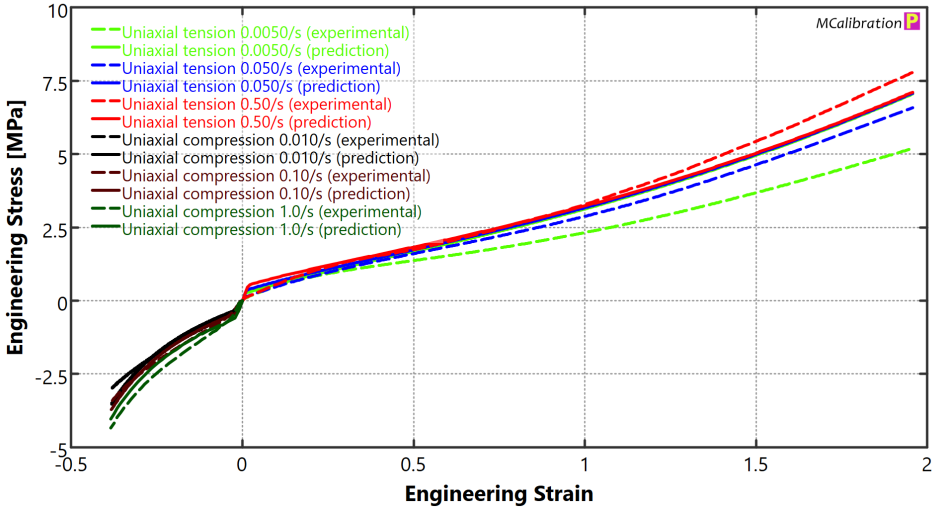

(b) Ogden as hyperelastic network

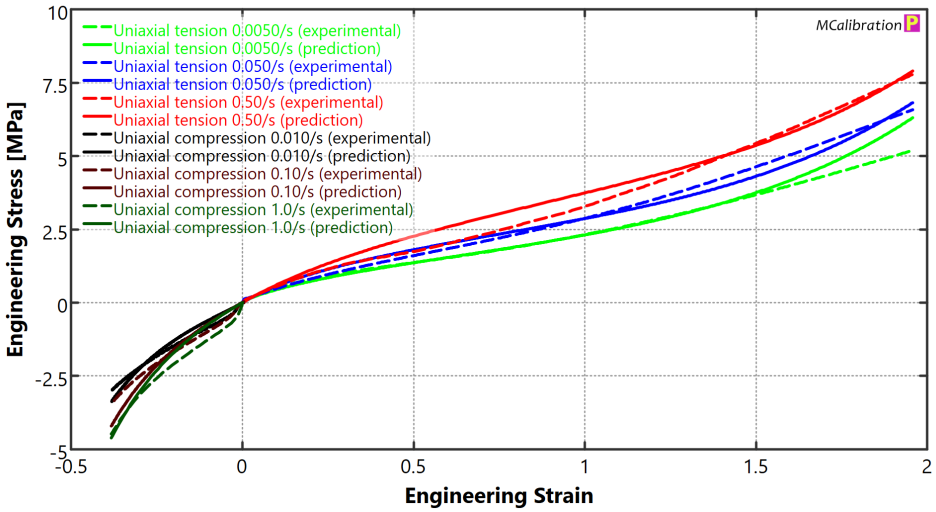

(c) Arruda–Boyce as hyperelastic network

Figure 4.7: Curve fitting procedure using software package MCalibration [27]

Evaluation prediction models

The error of each prediction per model was quantified using the Normalized Absolute Difference (NMAD). Mathematically, the prediction error is defined as in Eq. 4.12. The results of the best fit obtained from the Levenberg-Marquardt algorithm are given in Table 4.3. Between the evaluated hyperelastic models within the hysteresis material model, the Arruda-Boyce formulation was the only one capable of capturing the uniaxial tension curves within an acceptable error. As a result, it has the highest NMAD value. Despite its slightly lower predictive accuracy for the uniaxial compression tests compared to the Ogden and Neo-Hookean model, this model was selected due to the emphasizes on the tensile behavior in the context of this failure related study. The parameters of the hysteresis option with the fit of the Arruda-Boyce as hyperelastic formulation are shown in Table 4.4 which is also called the Bergstrom-Boyce [9] implementation in Abaqus. The top three parameters quantifying the hyperelastic part discussed in subsection 3.1.2 whereas the remaining five define the rate-dependent behavior.

$$\text{NMAD (\%)} = \frac{1}{n}\sum_{i=1}^{n}\left|\frac{x_i^{\text{prediction}} - x_i^{\text{experimental}}}{x_i^{\text{experimental}}}\right| \times 100 \tag{4.12}$$

Table 4.3: Normalized Mean Absolute Difference (NMAD) for prediction models

NMAD (%)	Neo-Hookean	Ogden	Arruda-Boyce
Uniaxial tension 0.0050/s	12.4%	24.5%	5.1%
Uniaxial tension 0.050/s	16.7%	8.1%	5.5%
Uniaxial tension 0.50/s	25.9%	6.6%	6.2%
Uniaxial compression 0.010/s	9.2%	8.9%	11.6%
Uniaxial compression 0.10/s	5.6%	7.3%	14.2%
Uniaxial compression 1.0/s	1.2%	11.7%	13.7%
Total NMAD	**11.9%**	**11.2%**	**9.4%**

Table 4.4: Parameters Bergström-Boyce model Abaqus implementation (sub option Hysteresis)

Parameters	Value	Unit
μ	0.75	MPa
λ	1.86	-
D	0	MPa
S	0.98	-
A	0.0057	$s^{-1}MPa^{-m}$
m	1.57	-
C	-1	-
E	0.032	-

5

Most suitable damage parameter

In general, the fatigue life of rubber is dependent on various factors such as filler type, filler volume and environmental conditions. The most important factor during operation that affects the fatigue life of the rubber is the loading ratio [6] [59]. The loading ratio is characterized as the ratio between minimum and maximum stress. In the literature, often strain, stress, or energy-based methods are used to quantify the fatigue life of rubber. To investigate the ability of several parameters to predict the fatigue life of rubber in a range of R ratios, a uniaxial dataset of X.Wang et al. [77] has been used.

5.1. Geometry specimen and compound

During the experiments, filled natural rubber with the compound according to Table 5.1 was used. The cylindrical dumbbell specimen in Figure 5.1a was loaded with displacement-controlled tests at an excitation of 5 Hz. The experiments included 30 load cases in total with loading ratios ranging from -0.58 to 0.22. Each load case is repeated at least three times to ensure redundancy, after which the average number of cycles to failure was taken. The hyperelastic material parameters of the rubber compound were described by the Mooney-Rivlin constants C_{10} and C_{01} being equal to 0.29 MPa and 0.060 MPa respectively. Since X.Wang et al. [77] performed displacement-related experiments, the dumbbell specimen was modeled in FEA as shown in Figure 5.1b to gain insight into the corresponding stresses and strains. During the analysis, 3D solid hexahedral elements (C3D8RH) were used.

Table 5.1: Rubber compound formulation [77]

Ingredient	**PHR[a]**	**Weight (%)**
Natural rubber	100	68.45
Zinc oxide	6	4.11
N330 carbon black	10	6.84
N550 carbon black	10	6.84
Naphthenic oil	7	4.79
Others	13.1	8.96
Total	**146.1**	**100.0**

[a] Parts per hundred rubber, by weight.

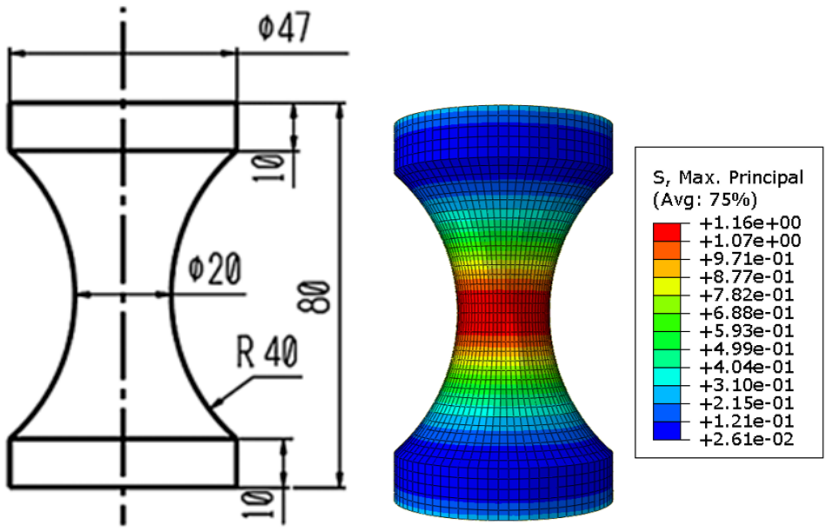

(a) Dumbbell specimen [77] **(b)** FEA modeling (stress example)

Figure 5.1: Process to determine stresses and strains inside dumbbell specimen

In addition to the maximum principal strain and stress, several studies in the literature [78] emphasize the use of mean strain, mean stress, or their strain or stress amplitudes as relevant parameters rather than the R ratio, since this is a scalar quantity. These parameters are defined in Eq. 5.1 through Eq. 5.4. Furthermore, the strain energy density according to Eq. 5.5 is also often used. Therefore, these parameters were also investigated based on the uniaxial dataset.

$$\sigma_{\text{mean}} = \frac{\sigma_{\text{max}} + \sigma_{\text{min}}}{2} \tag{5.1}$$

$$\sigma_{\text{amp}} = \frac{\sigma_{\text{max}} - \sigma_{\text{min}}}{2} \tag{5.2}$$

$$\epsilon_{\text{mean}} = \frac{\epsilon_{\text{max}} + \epsilon_{\text{min}}}{2} \tag{5.3}$$

$$\epsilon_{\text{amp}} = \frac{\epsilon_{\text{max}} - \epsilon_{\text{min}}}{2} \tag{5.4}$$

$$W = \int \sigma \, d\varepsilon \tag{5.5}$$

5.2. Damage parameters correlation

Several damage parameters have been analyzed based on the uniaxial dataset. The correlations for different loading ratios and the relations for a certain number of cycles before failure are given in Figure 5.2. The corresponding values in the data set can be found in Table 10.1.

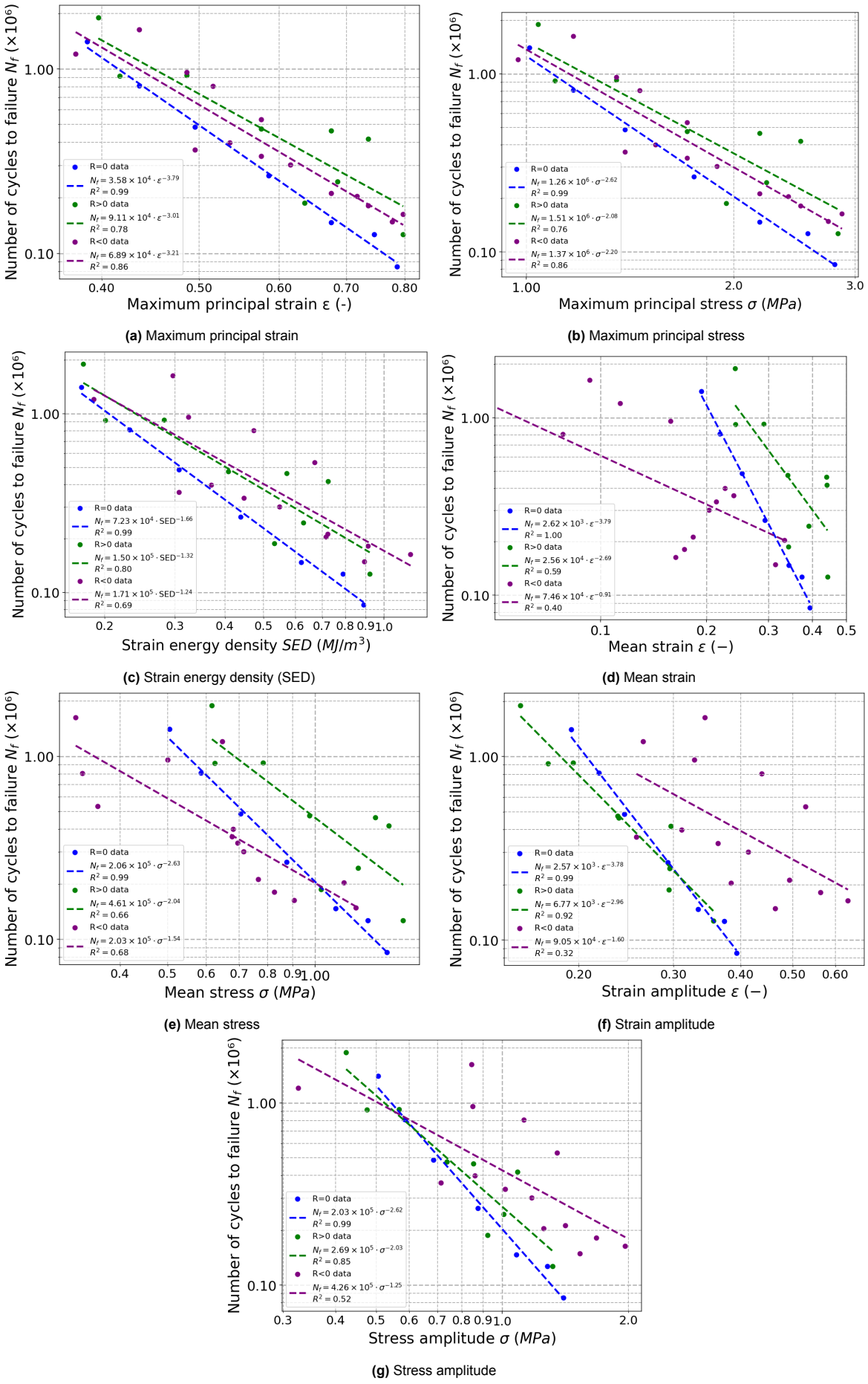

Figure 5.2: Correlation (R^2) damage parameters uniaxial tension with different R-ratios [77]

Based on the correlation analysis of the different parameters used for various loading ratios ranging from -0.85 to 0.22, it can be concluded that the maximum principal strain and stress perform consistently best across all combined loading ratios with coefficients of 0.83 and 0.82, respectively. The correlations were determined with the polynomial least squares method according Eq. 5.6. Here is $\hat{y}_i$, the predicted value calculated through the polynomial. $\bar{y}$, mean of all experimental values, and y_i the experimental value. For the specific case with a loading ratio of zero, all parameters exhibit high correlations with coefficients of 0.99. The amplitude strain and the amplitude stress proved to be the most suitable predictors for loading ratios greater than zero in the data set studied. Furthermore, the graphs based on the maximum principal strain and stress show that natural rubber fails most quickly with a loading ratio of zero, while it will endure the longest with loading ratios greater than zero. This observation is consistent with findings in the literature [60] and can be explained by the fact that natural rubber reinforces with positive loading ratios.

$$R^2 = \frac{\sum_{i=1}^{n}(\hat{y}_i - \bar{y})^2}{\sum_{i=1}^{n}(y_i - \bar{y})^2} \tag{5.6}$$

Table 5.2: Correlation coefficients (R^2) for different parameters and loading ratios (R) under uniaxial tension

Parameters	**Combined**	$\boldsymbol{R = 0}$	$\boldsymbol{R > 0}$	$\boldsymbol{R < 0}$
Max principal strain	0.83	0.99	0.78	0.86
Max principal stress	0.82	0.99	0.76	0.86
SED	0.75	0.99	0.80	0.69
Mean strain	0.23	1.0	0.59	0.40
Mean stress	0.54	0.99	0.66	0.68
Amplitude strain	0.37	0.99	0.92	0.32
Amplitude stress	0.61	0.99	0.85	0.52

Since the maximum principal strain and stress perform most consistent, these parameters were studied further. The relations of the number of cycles to failure for the maximal principal strain and stress are shown in Table 5.3 and Table 5.4, respectively. In Figure 5.3 and Figure 5.4 the correlations and predictions are illustrated using the relation for all loading ratios combined for the number of cycles to failure. From the 30 data points, only two fall slightly outside the factor-two prediction bounds. All of the remaining data points lie within a factor of two from the ideal fit curve, for both the principal strain and stress models.

Table 5.3: Maximum principal strain relation to number of cycles to failure (N_f)

Loading Ratio	$\boldsymbol{N_f}$
$R = 0$	$3.58 \times 10^4 \cdot \varepsilon^{-3.79}$
$R > 0$	$9.11 \times 10^4 \cdot \varepsilon^{-3.01}$
$R < 0$	$6.89 \times 10^4 \cdot \varepsilon^{-3.21}$
Combined	$6.48 \times 10^4 \cdot \varepsilon^{-3.28}$

Table 5.4: Maximum principal stress relation to number of cycles to failure (N_f)

Loading Ratio	$\boldsymbol{N_f}$
$R = 0$	$1.26 \times 10^6 \cdot \sigma^{-2.62}$
$R > 0$	$1.51 \times 10^6 \cdot \sigma^{-2.08}$
$R < 0$	$1.37 \times 10^6 \cdot \sigma^{-2.20}$
Combined	$1.38 \times 10^6 \cdot \sigma^{-2.26}$

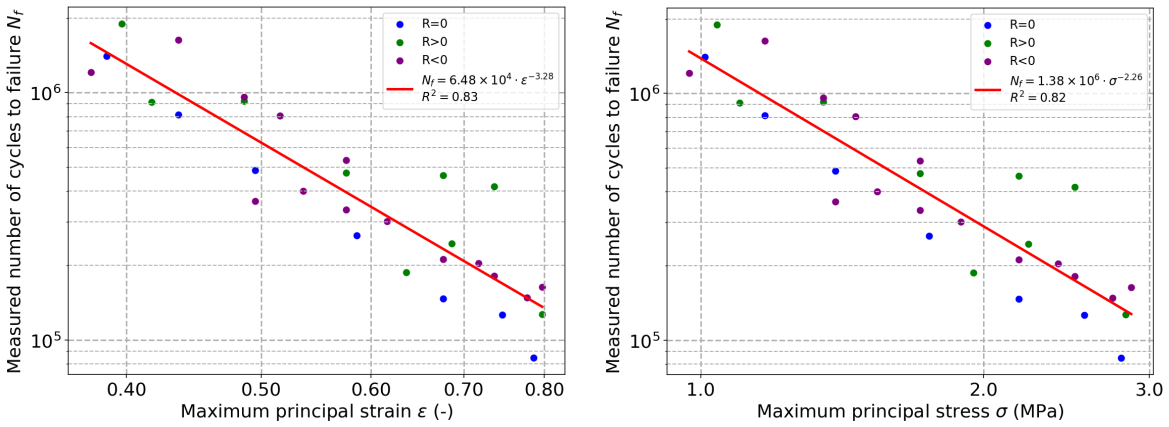

(a) Maximum principal strain

(b) Maximum principal stress

Figure 5.3: Correlation (R^2) principal strain and stress using all R-ratios combined for uniaxial tension

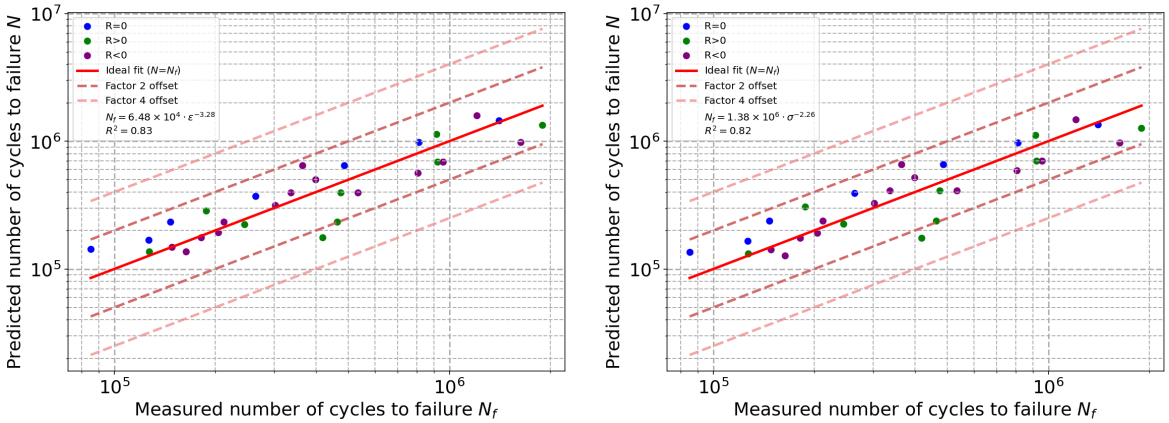

(a) Maximum principal strain

(b) Maximum principal stress

Figure 5.4: Predictions maximum principal strain and stress using all R-ratios combined for uniaxial tension

5.3. Relation with multiaxial fatigue

Based on the graphs in section 5.2, it can be concluded that the maximum principal strain and stress are the most suitable for the NR uniaxial dataset of X.Wang et al. [77] for all combined loading ratios of the parameters studied. In real-world applications, components are often subjected to a multiaxial stress state with shear stresses included as well. Therefore, the question arises whether the maximum principal strain and stress are also able to make reliable predictions under multiaxial conditions. N.Saintier et al. [60] found that the maximum principal stress for natural rubber is able to predict the number of cycles to crack initiation for loading ratios $R \leq 0$ in uniaxial tension and torsion experiments shown in Figure 5.5, due to the fact that natural rubber shows strain-induced crystallization for loading ratios greater than zero. This matched the findings for the uniaxial data set discussed in section 5.2. During torsion experiments, the observations show that natural rubber exhibits mode I failure, where cracks consistently initiate in the direction perpendicular to the maximum first principal stress when material rotations are taken into account. The test method used will be explained in subsection 5.3.1. Since the crack orientation is correctly predicted by the direction of the first principal stress, this validates the use of this damage parameter. In contrast with natural rubber, styrene butadiene rubber does not exhibit strain-induced crystallization. Therefore, G.Ayoub et al. [6] decided to use the maximum first principal stress as the damage parameter for positive loading ratios as well. There was good agreement between the tension, torsion, and combined tension torsion experiments. However, the principal strain did not serve as a suitable parameter for multiaxial fatigue. Based on these findings, the maximum principal stress looks promising for both uniaxial and multiaxial fatigue. Therefore, the relation between

the principal stress and the number of cycles to crack initiation in the uniaxial data set in section 5.2 will be used for further analysis.

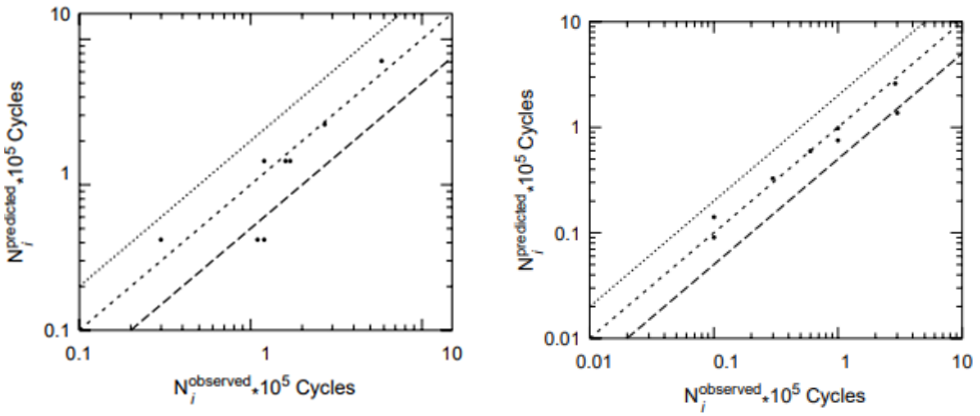

(a) Tension compression **(b)** Torsion

Figure 5.5: Uniaxial and torsion predictions N.Saintier et al. [60] maximum principal stress without reinforcement $R \leq 0$ [58]

5.3.1. Crack propagation

In addition to investigating a suitable multiaxial crack initiation parameter, Saintier et al. [58] investigated the crack propagation directions of small cracks with a length of approximately one millimeter as well with torsion experiments. When the angle of torsion of the specimen increases, the direction of the first principal stress also increases as shown in Figure 5.6a. Large strains lead to additional material rotations that must be taken into account with a material plane rotation angle. These are in general different from the direction of the first principal stress. Since the angle of orientation of the crack is usually measured in the undeformed state and the principal stress directions are calculated in the deformed state, they cannot be compared straightforwardly. With uniaxial-loaded push pull fatigue tests, it was found that cracks propagate normally in the tensile direction. Because the principal stress was an important crack initiation parameter in the torsion tests, the crack orientation at the moment of initiation was measured with an electron microscope. The following procedure was performed for the torsion tests at different angles. First, the plane that experiences the highest principal stress during a cycle is determined. Second, the associated eigenvector is transported in the undeformed configuration using Eq. 5.7. Third, the predicted and measured crack angles are compared. For these loading conditions, the conclusion can be drawn that cracks initiate normally to the local maximum principal stress and propagate in mode I as well for a multiaxial stress state [59].

$$\vec{n}_{CP}^{t_0} = \left(\left(F_{t_{\max}}^{-1} \right)^T \right)^{-1} \odot \vec{n}_{CP}^{t_{\max}} \tag{5.7}$$

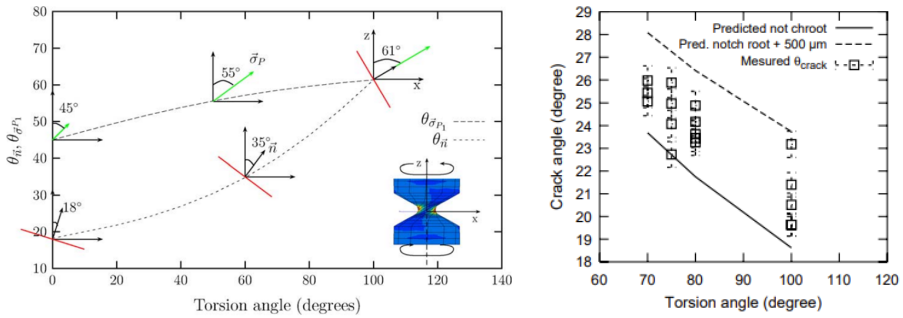

(a) Principal stress and material rotations for 0–100° torsion **(b)** Predicted and measured crack

Figure 5.6: Crack orientations torsion tests with principal stress direction Saintier et al. [58]

6

Cone fender implementation FEA

In this chapter, the cone fender will be implemented in FEA using the Abaqus software package [15] to evaluate the stress and strain distribution within the body. Cone fenders are the latest generation of fenders with high energy absorption capabilities and relative low reaction forces. Due to the conical geometry, this will ensure a stable compression cycle and effective shear resistance even for large deformations.

6.1. Dimensions

Trelleborg does have a various range of cone fenders ranging from 300 to 2500 millimeters in height with multiple compounds and their own characteristic performance. The exact dimensions of the example cone fender used are shown in Figure 6.1 obtained from the Trelleborg product brochure [40].

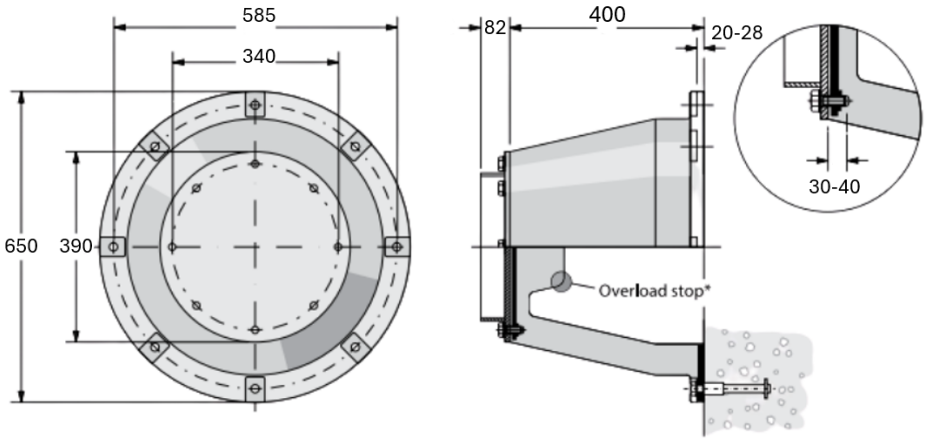

Figure 6.1: Dimensions (mm) Cone Fender (SCN 400) Trelleborg [40]

6.2. FEA model

The model in FEA of the cone fender is shown in Figure 6.2 modeled with axisymmetric elements as explained in subsection 6.2.1. To clarify the model towards the original design, the sweep function was used to generate the cut section view and 3D view. The cone fender was modeled using an implicit quasi-static dynamic analysis. In a quasi-static analysis, inertial effects are neglected. This assumption can be validated by plotting the internal energy against the kinetic energy of the system during a compression cycle. Here, a compression from 0 to 50% deflection was simulated using a compression time of five seconds, which is equal to a loading velocity of 40 mm/s. According to the

Abaqus guidelines [15], the kinetic energy of the system should not exceed the internal energy of the system with more than five percent. As shown in Figure 6.3, the simulation meets this criterion. This validates that a quasi static analysis is appropriate.

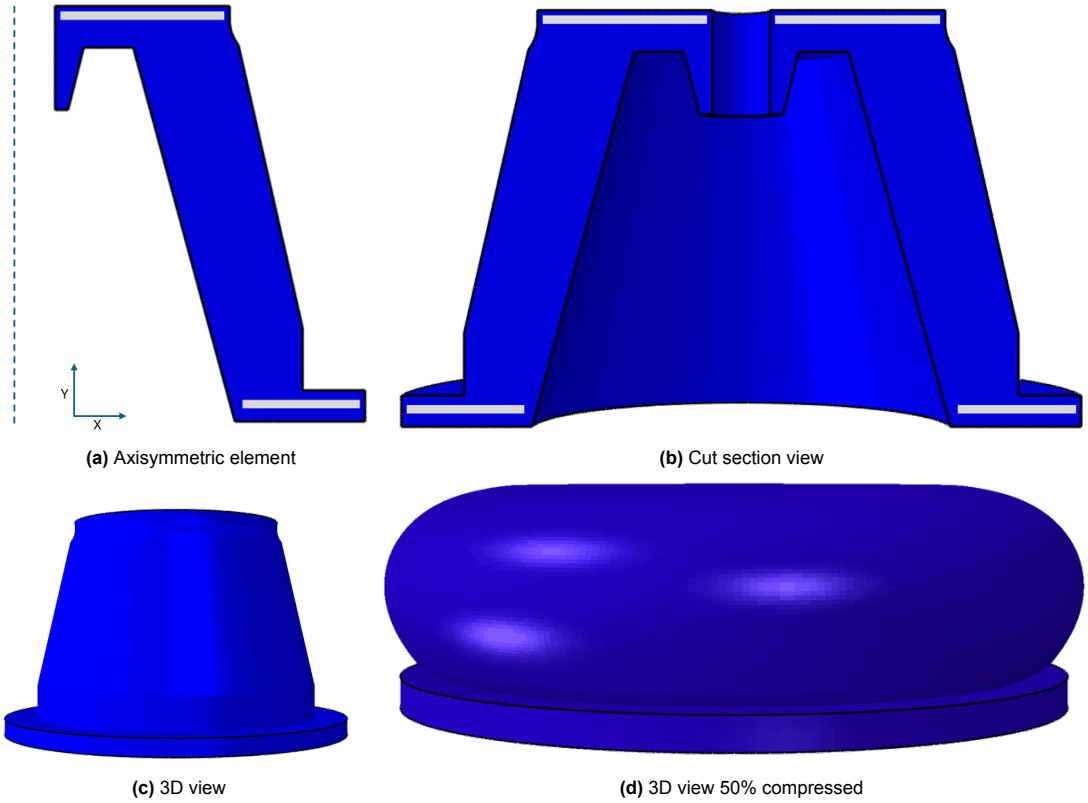

(a) Axisymmetric element

(b) Cut section view

(c) 3D view

(d) 3D view 50% compressed

Figure 6.2: Cone fender FEA model build in Abaqus

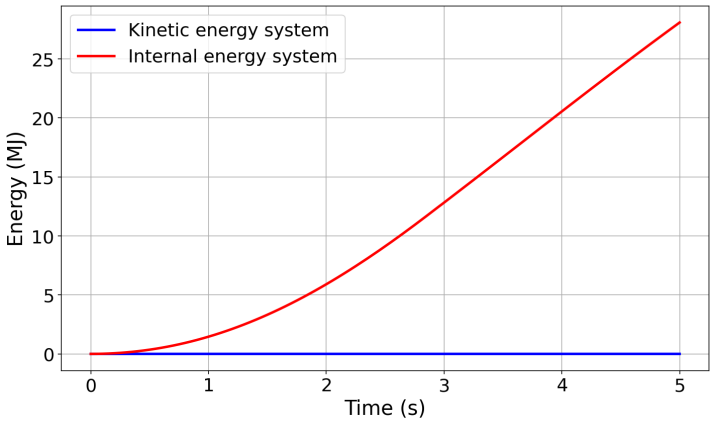

Figure 6.3: Internal energy and kinetic energy in FEA model during 0-50% compression in 5 seconds

6.2.1. Axisymmetric elements

Axisymmetric elements, as shown in Figure 6.4, could be used to implement a three-dimensional geometry in a two-dimensional representation in FEA. These elements can only be used when the geometry, material properties, and loading condition are equally around the symmetric axis. The radial and axial coordinates of a point in the section are given by r and z, respectively. When $\theta = 0$, the radial and axial coordinates are equal to the global Cartesian X and Y coordinates [15]. The displacement at each point will have only radial and axial components with θ indicating the principal direction of the material. This

results in the stress components given in Eq. 6.1. Here is σ_{rr}, the radial stress, σ_{zz}, the axial stress, $\sigma_{\phi\phi}$, the circumferential stress and σ_{rz} the shear stress acting on the rz plane. The deformation in the r-z plane fully defines the state of stress and strain in the body. The main advantage of these elements is that the computational time of the model is significantly reduced while maintaining accurate results.

$$\sigma = \begin{bmatrix} \sigma_{rr} & \sigma_{rz} & 0 \\ \sigma_{zr} & \sigma_{zz} & 0 \\ 0 & 0 & \sigma_{\theta\theta} \end{bmatrix} \tag{6.1}$$

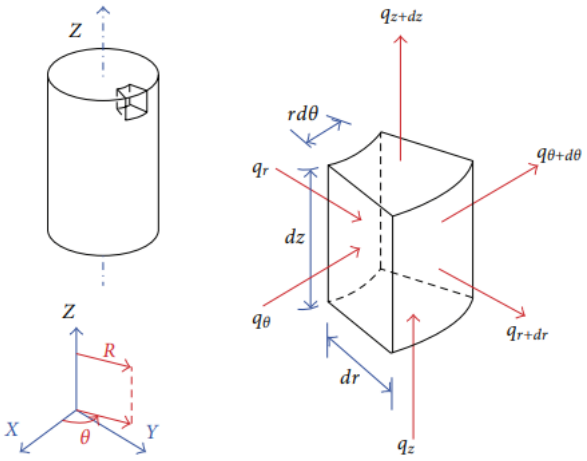

Figure 6.4: Axisymmetric element [17]

6.2.2. Boundary conditions

The rubber material of the cone fender (blue section) is modeled with the parameters determined in Table 4.4 from the experiments and implemented under the HYSTERESIS option in Abaqus. The steel plates (gray section) at the top and bottom are modeled as rigid bodies because they have a very high stiffness compared to the rubber section. The bottom steel plate is constrained in all directions according to Eq. 6.2 and cannot move because in reality it is attached to the quay wall with bolts. The top steel plate is bolted with the friction plates that are mounted on top of the cone fender. The assumption is that the rigid top part can only move in the axial direction with the corresponding constraint according to Eq. 6.3. Given that the most important scenario is when a vessel is already moored and often pre-tensioned with mooring lines and that friction plates mounted on top of the cone fender do have a relative low friction coefficient, this assumption is plausible. On the upper surface, a displacement is given in the vertical direction according to Eq. 6.4 to simulate the behavior of the cone fender during a compression cycle. Note that the boundary conditions are based on the axisymmetric element that is modeled in the XY plane. As a result, U_1 and UR_1 correspond to displacement in the x direction and rotation around the x axis, respectively. The constraints are visualized in Figure 6.5. For self contact, normal behavior was used with the pressure overclosure defined as hard contact. This ensures a pressure when two surfaces touch and penetration of the surfaces is not allowed.

$$U_1 = U_2 = U_3 = UR_1 = UR_2 = UR_3 = 0 \tag{6.2}$$

$$U_1 = U_3 = UR_1 = UR_2 = UR_3 = 0 \tag{6.3}$$

$$U_2 = x \tag{6.4}$$

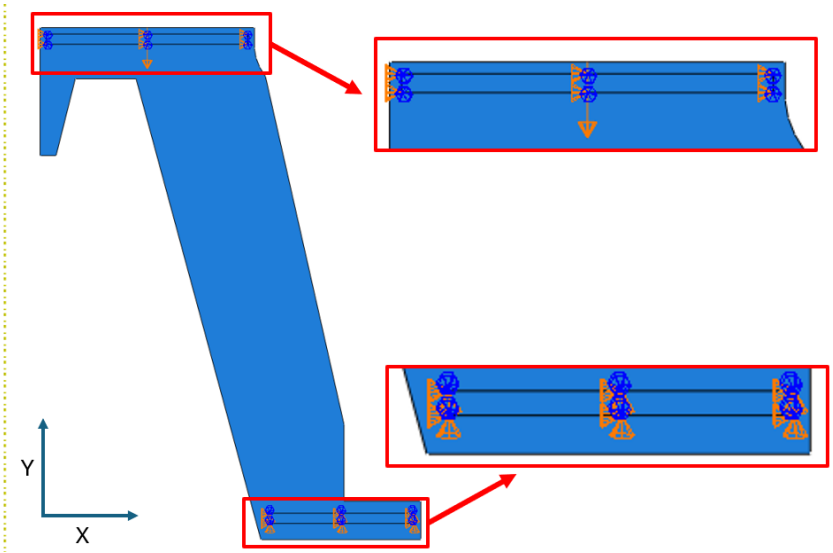

Figure 6.5: Constraints FEA model cone fender

6.2.3. Mesh convergence study

In FEA the reliability of the results of the model is dependent on the type of mesh used. The execution of a mesh convergence study is a crucial step in the analysis to ensure that the chosen element leads to the desired result without unnecessary computational time. For this study, axisymmetric four node quadrilateral hybrid elements (CAX4RH) were used with reduced integration for computational efficiency. This element is suitable for rubber experiencing large deformations. Since rubber is modeled as an incompressible material, the solution can not be determined only based on displacement due to the fact that hydrostatic pressure can be added without influencing displacements [15]. In this case, a small change in displacement will result in a large change of pressure that will result in a singularity. To solve this behavior, hybrid (mixed) elements were used that consist of a mixture between displacement and stress variables to solve the equilibrium equations. The mesh size on the axisymmetric element is varied from an average size of 20 mm to 3 mm, corresponding to 153 elements for the largest mesh size and 4322 elements for the smallest mesh size. The displacement, strain, and stress of the most critical element of the outer axis (defined in Figure 6.11) during a compression cycle from 0 to 50% have been determined for every mesh size. The results were normalized and given in Figure 6.7a. All parameters were found to stabilize with the average mesh of 3 mm that corresponded to 4322 elements in total. In Figure 6.7b is shown that the computational time of the model and the number of elements following a linear relationship for the investigated range.

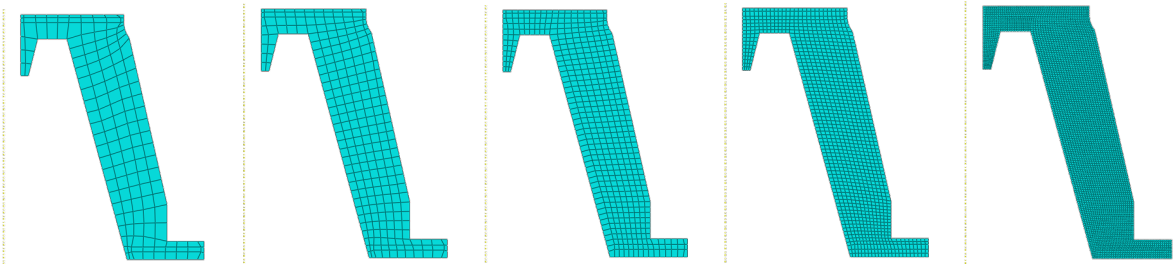

(a) 20 mm mesh 153 elements | **(b)** 15 mm mesh 264 elements | **(c)** 9 mm mesh 507 elements | **(d)** 6 mm mesh 1135 elements | **(e)** 3mm mesh 4322 elements

Figure 6.6: Axisymmetric quadrilateral hybrid element (CAX4RH) with different type of mesh sizes on FEA model

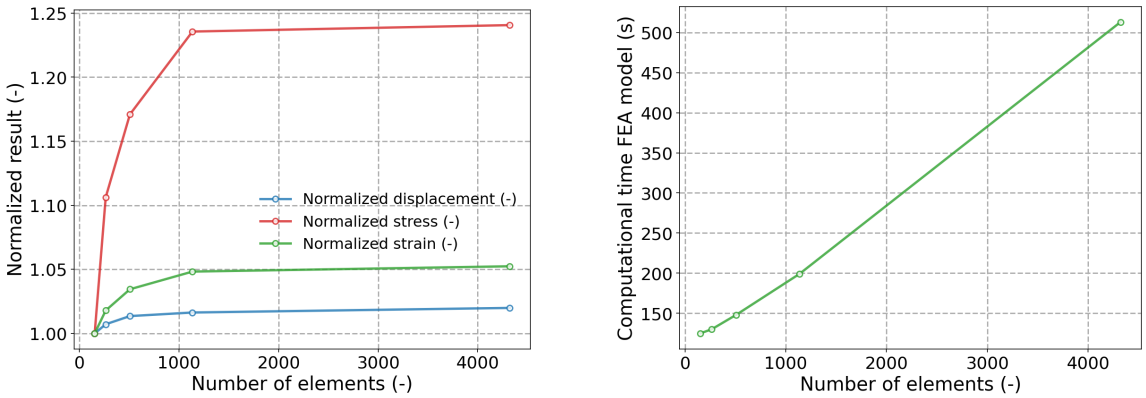

(a) Mesh convergence study

(b) Computational time model with number of elements

Figure 6.7: Mesh convergence study and computational time FEA model in Abaqus

6.2.4. Force deflection curve

To validate the FEA model of the cone fender based on the experimental test data and the boundary conditions of the model, the force deflection curve from the Trelleborg product brochure [40] was compared to the results of the model in FEA with a compression velocity of 40 mm/s. As shown in Figure 6.8, the shape of the curve shows good agreement. However, the FEA model acts stiffer than the actual experimental curve until the buckling point with a maximum reaction force of approximately 14% higher. This deviation can be explained by the fact that the experimental data from the uniaxial tension and compression tests did not contain any preconditioning cycles. Therefore, the expectation is that the performance of the model in FEA will drop significantly during the first few load cycles due to the Mullins effect. This phenomenon is explained in subsection 3.2.2. Furthermore, the post buckling behavior leads to a larger drop in reaction force. A possible explanation for this could be that the uniaxial compression tests reached a minimum true strain of -0.48, whereas the minimum true strain in the FEA model was found equal to -0.85. During the buckling phase of the FEA model, a small drop in force can be observed that is related to a local instability. Since this effect is minimal, it was considered acceptable.

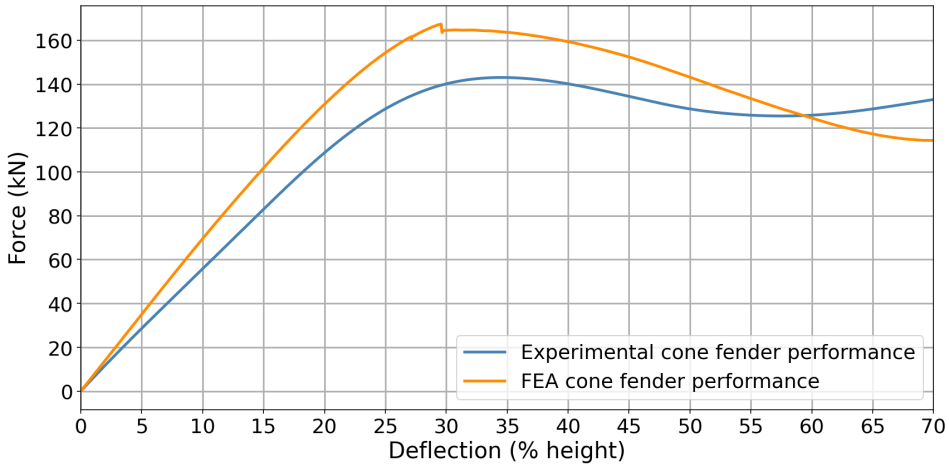

Figure 6.8: Force deflection curve FEA model and experimental curve cone fender

6.3. Stress development during compression cycle

Since the maximum principal stress has been found to be the most important damage parameter investigated in chapter 5, it was chosen to identify critical zones in the cone fender based on the evolution of the maximum principal stress during a compression cycle ranging from 0 to 50%.

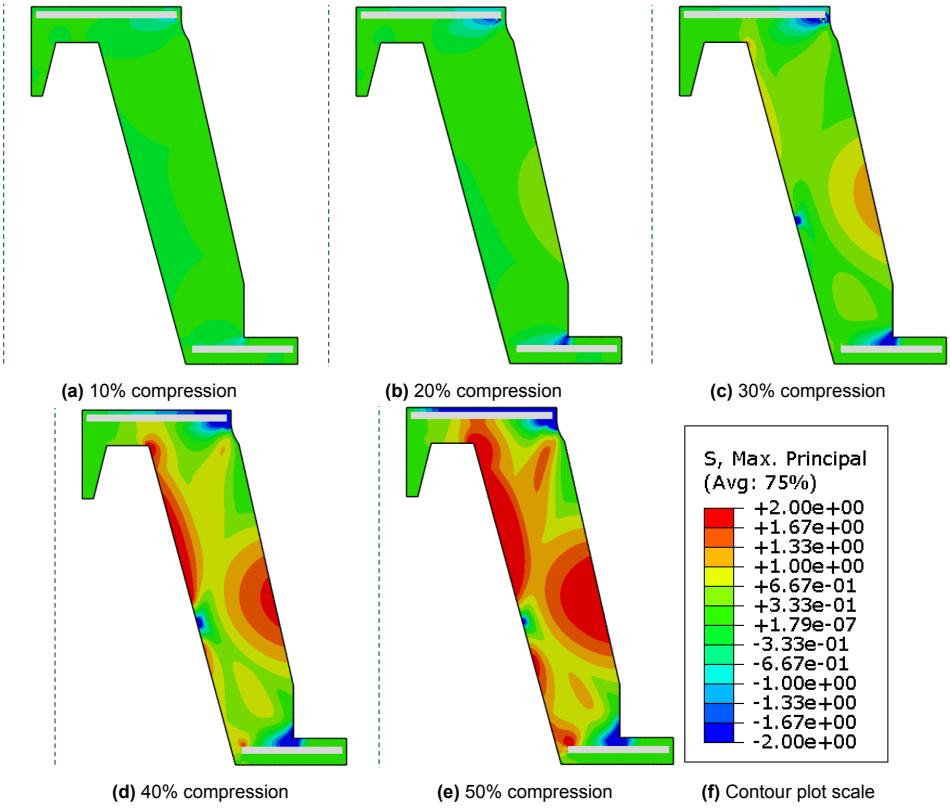

(a) 10% compression **(b)** 20% compression **(c)** 30% compression

(d) 40% compression **(e)** 50% compression **(f)** Contour plot scale

Figure 6.9: Maximum principal stress development FEA in undeformed configuration

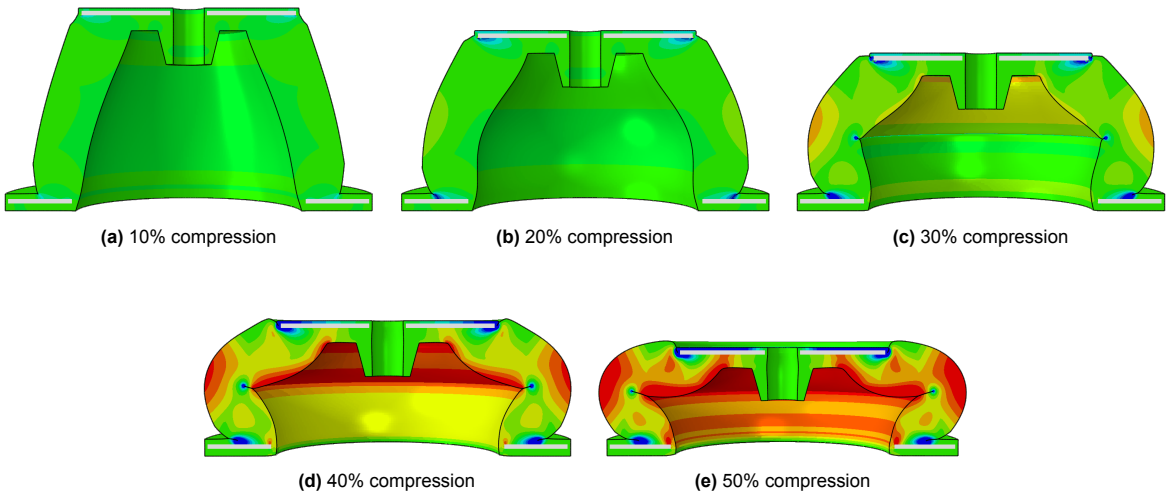

(a) 10% compression **(b)** 20% compression **(c)** 30% compression

(d) 40% compression **(e)** 50% compression

Figure 6.10: Maximum principal stress development FEA in deformed configuration cut section view

Due to the development of the maximum principal stress in multiple regions as shown in the undeformed configuration in Figure 6.9, three critical elements located within these regions were chosen for further analysis. In addition, three paths along the inside, intermediate, and outside axes have been

defined for detailed investigation. These critical elements and paths are defined in Figure 6.11. In Figure 6.12 is shown how the maximum principal stress develops along these (normalized) axes during a compression cycle. It is clearly observed that the maximum principal stress increases in the elements during the compression cycle, especially in the highest damaged regions within the selected elements one, two, and three.

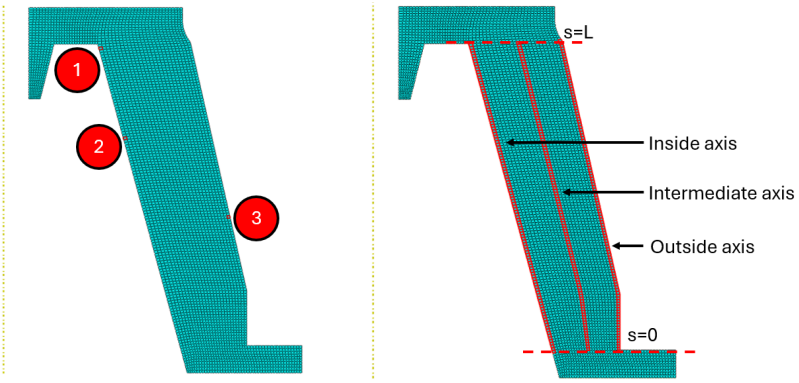

(a) Critical elements **(b)** Defined paths along axis

Figure 6.11: Critical elements and defined paths along axis FEA model

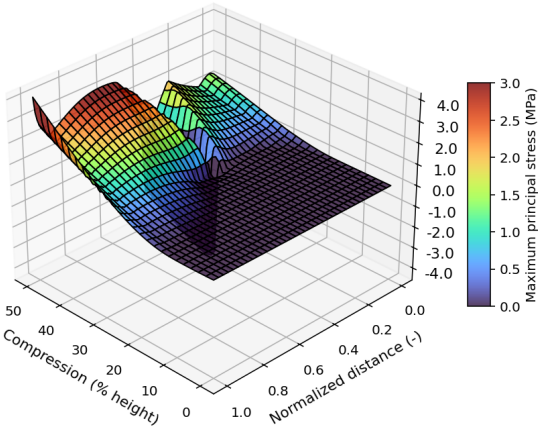

(a) Maximum principal stress inside axis

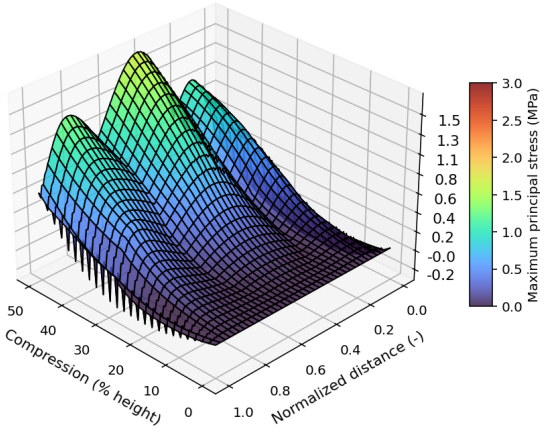

(b) Maximum principal stress intermediate axis

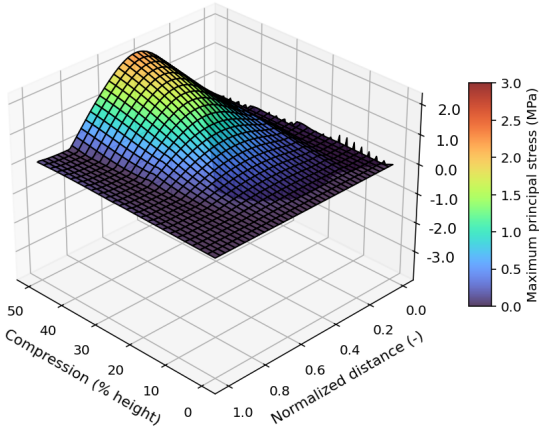

(c) Maximum principal stress outside axis

Figure 6.12: Stress distribution along axes FEA model during compression cycle

6.4. Strain rate evolution during compression cycle

To investigate the strain rate during a compression cycle, the axes defined in Figure 6.11 were used. To determine the compression velocity, the case study in Geraldton of a permanent moored vessel was analyzed [25]. The maximum compression velocity observed in this case study was found to be 80 mm/s. This is approximately half the compression velocity assumed for the fender design of a berthing vessel [2]. For further analysis, a compression velocity of 40 mm/s was used, which corresponds to a practical average.

The maximum principal strain rate and the minimum principal strain rate for the inside, intermediate, and outside axis of the cone fender during a compression cycle were plotted in Figure 6.13, Figure 6.14, and Figure 6.15, respectively. The maximum principal strain rate corresponds to the strain rate in tension, whereas the minimum principal strain rate corresponds to the strain rate in compression. The distances along the three axes were normalized and start at s = 0 with the end point s=L and are plotted in their undeformed configuration. The colors in the three-dimensional visualization graphs were based on the average strain rate between four points.

The graphs show an increase in the maximum principal strain rate and an decrease in the minimum principal strain rate during the buckling phase of the cone fender (around 30% deflection) in the inside axis. This corresponds to a maximum principal strain rate of approximately 1.2/s, while at the same time a minimum principal strain rate of -1.4/s was reached. Note that the duration of the maximum and minimum strain rates is really short and last approximately 0.1 seconds, which results in a lower average strain rate according to the color map. All other elements along the inside axis show a strain rate approximately six times lower than these peaks. The intermediate and outside axes do not show such peaks, allowing a more accurate analysis of how the strain rate varies on a smaller scale. Here, both the average maximum and the minimum principal strain rate among the elements during compression in time fluctuate around $\pm$ 0.1/s. Other elements show maximum and minimum principal strain rates of approximately ± 0.01/s at certain stages of the compression cycle. This results in a difference of two orders of magnitude between the maximum and minimal principal strain rate evolution among elements along the axes investigated during a compression cycle.

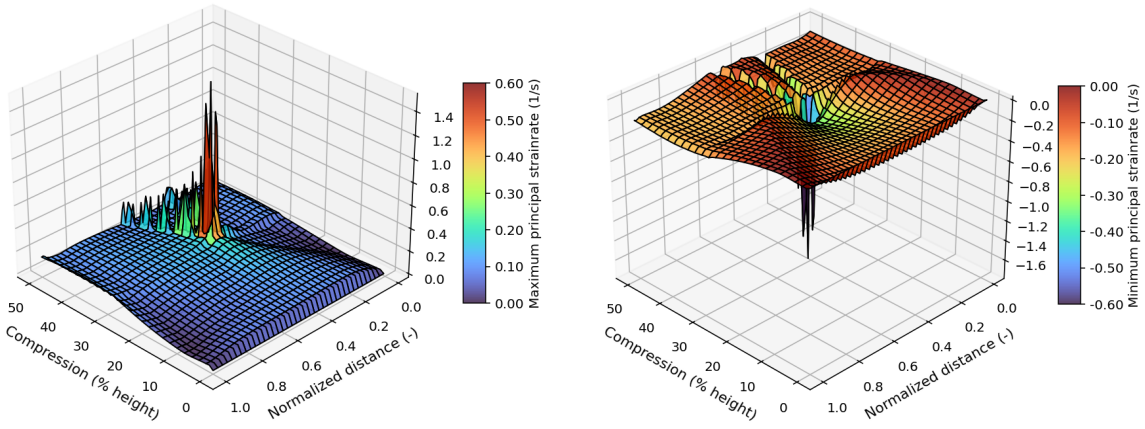

(a) Maximum principal strain rate

(b) Minimum principal strain rate

Figure 6.13: Strain rate distribution along inside axis FEA model during compression cycle

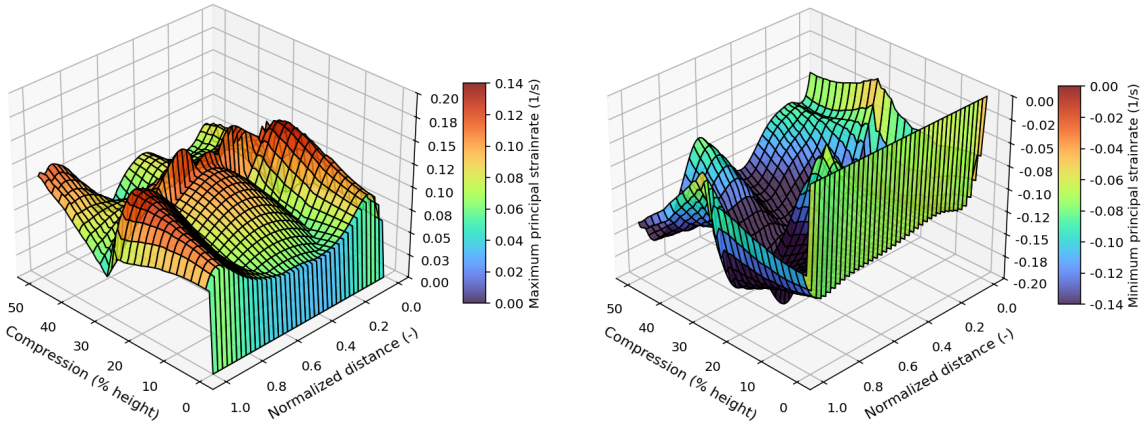

(a) Maximum principal strain rate **(b)** Minimum principal strain rate

Figure 6.14: Strain rate distribution along intermediate axis FEA model during compression cycle

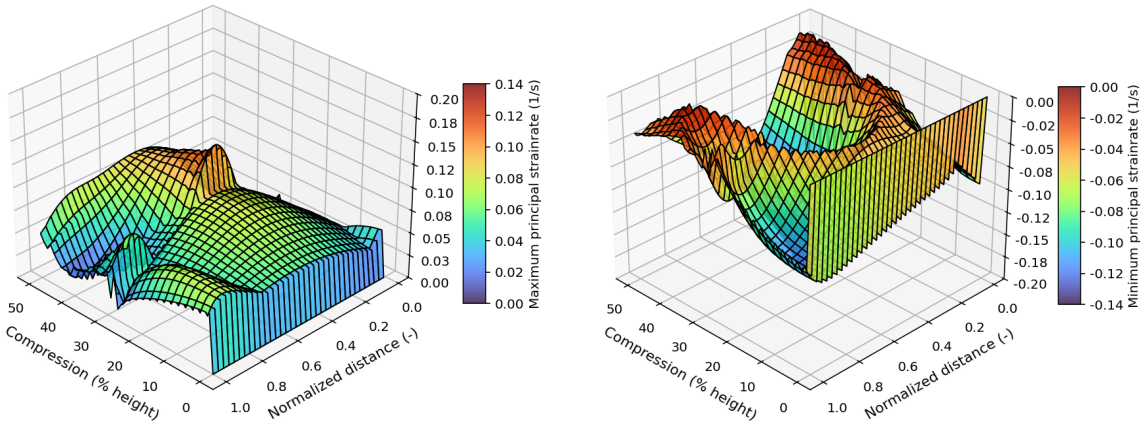

(a) Maximum principal strain rate **(b)** Minimum principal strain rate

Figure 6.15: Strain rate distribution along outside axis FEA model during compression cycle

6.5. Stress states critical elements varying compression velocity

To investigate the influence of loading velocity on the stress states in the cone fender, stress plots of the critical elements were made at various compression velocities. Based on the case study [25], loading velocities ranging from 10 mm/s to 80 mm/s were chosen, each scaled by a factor of two to highlight trends. In addition to the maximum principal stress, the minimum principal stress and the corresponding maximum and minimum principal strain rates were also plotted. The graphs are shown in Figure 6.16, Figure 6.17, and Figure 6.18.

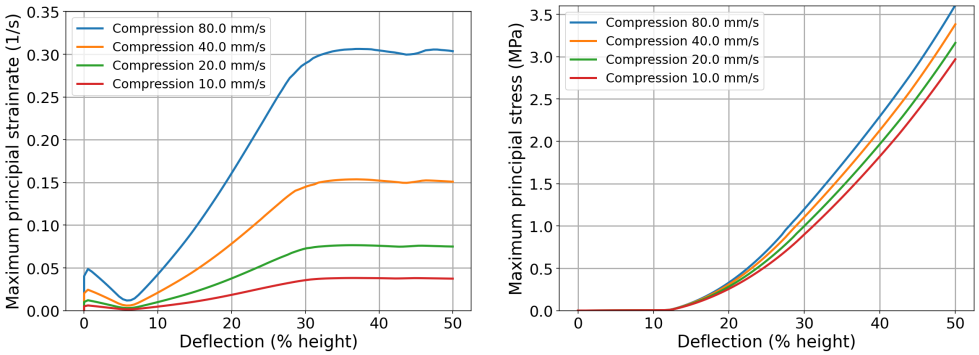

(a) Maximum principal strainrate during compression

(b) Maximum principal stress during compression

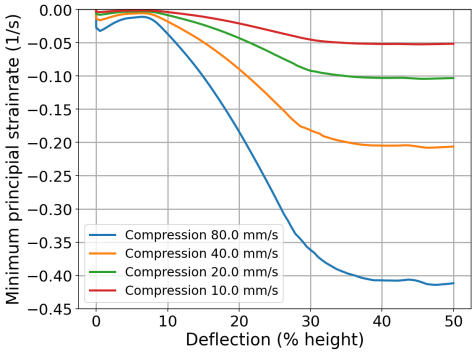

(c) Minimum principal strainrate during compression

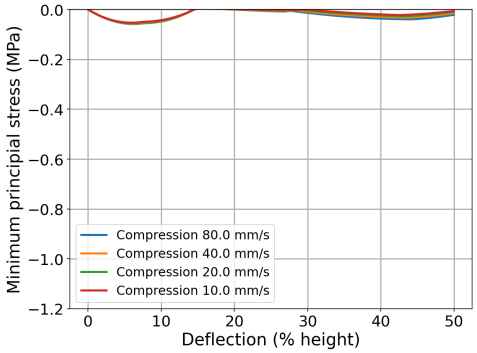

(d) Minimum principal stress during compression

Figure 6.16: Maximum and minimum principal strainrate and stress on critical element one during 0–50% compression

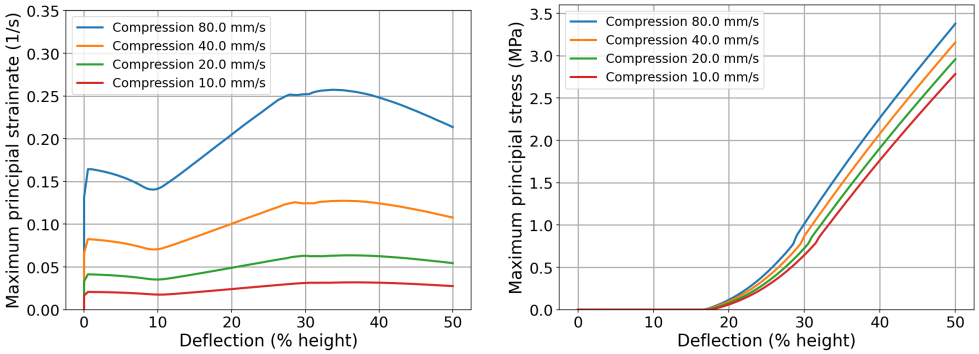

(a) Maximum principal strainrate during compression

(b) Maximum principal stress during compression

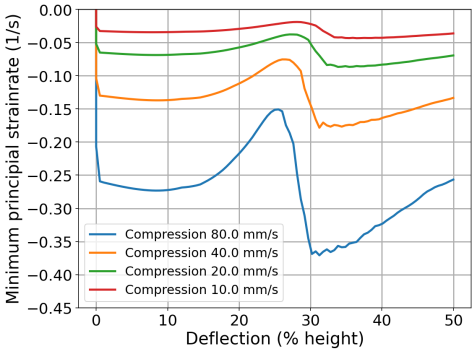

(c) Minimum principal strainrate during compression

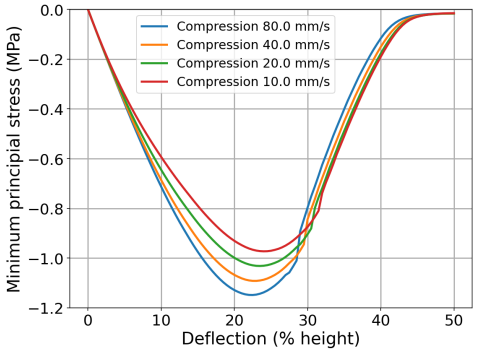

(d) Minimum principal stress during compression

Figure 6.17: Maximum and minimum principal strainrate and stress on critical element two during 0–50% compression

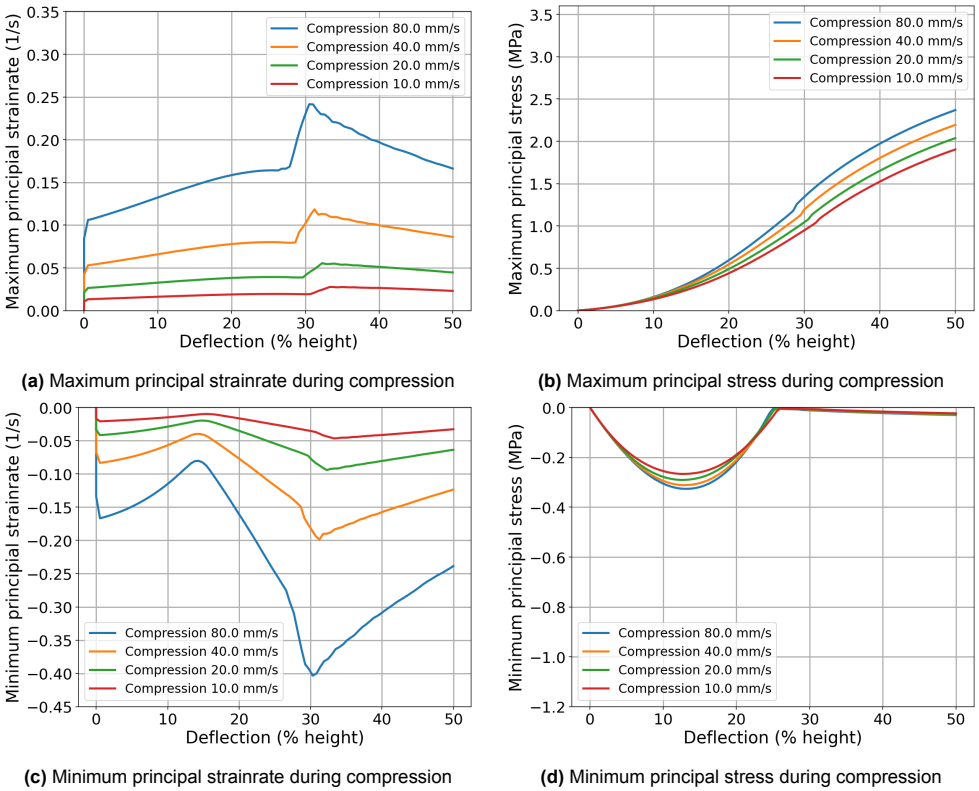

(a) Maximum principal strainrate during compression

(b) Maximum principal stress during compression

(c) Minimum principal strainrate during compression

(d) Minimum principal stress during compression

Figure 6.18: Maximum and minimum principal strainrate and stress on critical element three during 0–50% compression

In the corresponding strain rate graphs for each critical element, it is shown that both maximum and minimum principal strain rates scale proportionally to the loading velocity. Furthermore, the maximum principal stress increases while the minimum principal stress decreases with increasing loading velocity because of the rate-dependent properties of rubber. The average increase in the maximum principal stresses between the critical elements was further investigated for this study related to damage and is shown in Figure 6.19a. The higher loading velocities were compared to the slowest loading velocity of 10 mm/s. It can be observed that at 30% compression, the relative increase is highest. In case the fastest loading velocity of 80 mm/s is compared to the slowest of 10 mm/s, the maximum average increase in the maximum principal stress is 37% at a deflection of 25%, while this is only 22% at a deflection of 50%. Although stress increases for the critical elements with increasing loading velocity, this has an even greater influence on the predicted service life as shown in Figure 6.19b. The relationship used is further explained in section 6.7.

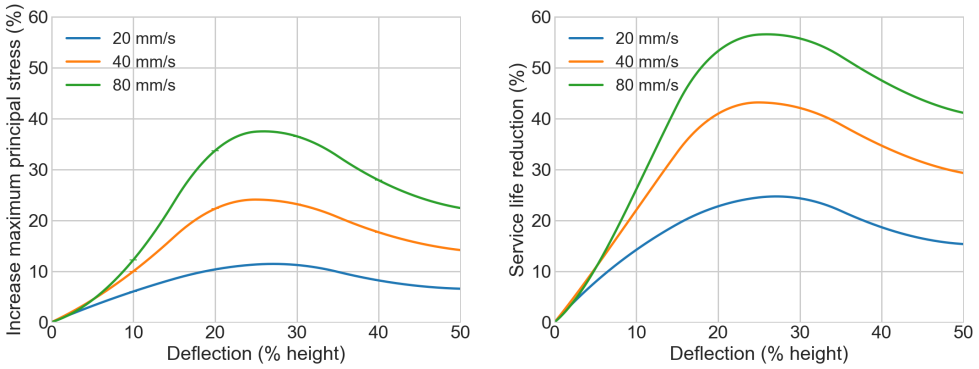

(a) Average maximum principal stress increase

(b) Service life decrease

Figure 6.19: Average increase stress critical elements with corresponding service life reduction relative to 10 mm/s

6.5.1. Maximum principal stress strain relations critical elements

The maximum principal stress strain relations for the critical elements were further investigated for the different compression velocities and given in Figure 6.20. It is relevant to examine whether an increase in compression velocity, or the corresponding proportional scaling strain rate found in section 6.5 results in the same increase in stress compared to the experiments performed in chapter 4. To determine this, the maximum principal stress of the critical elements was investigated at a maximum principal strain of 0.3. To achieve a factor of ten difference, the compression velocity of 100 mm/s was added to the graphs. The increase in maximum principal stress at 100 mm/s relative to 10 mm/s was found to be 22.0%, 31.7%, and 26.8% for critical elements one, two, and three, respectively. This results in an average increase of 26.8% among the critical elements. The increase in stress in the experimental true stress strain relation of the uniaxial tension tests was found to be 29.3% comparing a factor ten difference in engineering strain rate. This indicates that there is a minor difference of 2.5% between the average increase within the critical elements and the experimental tests. However, the compression velocity does not affect each element equally with respect to the increase in the maximum principal stress. This finding can be explained by the fact that the evolution of the maximum principal strain rate during a compression cycle for each element is different.

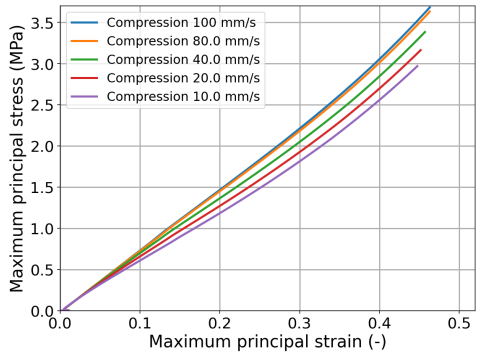

(a) Stress strain relation critical element one

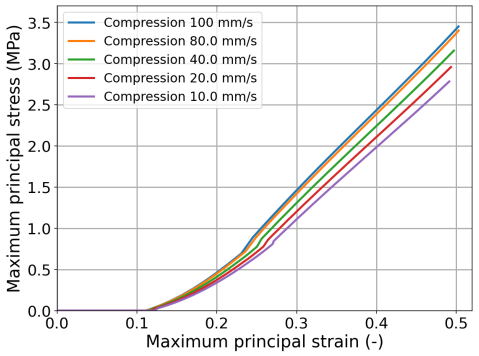

(b) Stress strain relation critical element two

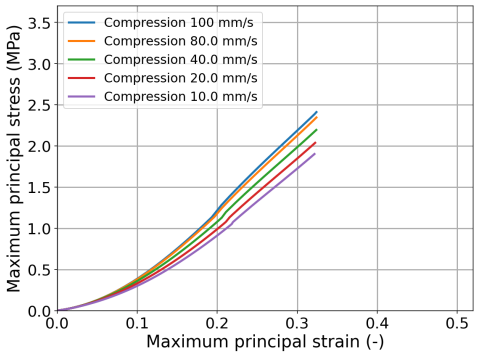

(c) Stress strain relation critical element three

Figure 6.20: Maximum principal stress and strain relations critical elements at different compression velocities

6.6. R-ratio critical elements

According to theory, the loading ratio is influenced by the maximum and minimum stress during a load cycle, which does impact the fatigue life of the rubber as discussed in chapter 5. When a vessel is exposed to cyclic loading, it is possible that the cone fenders do not fully return to their initial position due to the delayed strain, which is a viscoelastic property. To investigate this effect, six load unload cycles were applied to the model in FEA, followed by a rest period of three seconds, five seconds, and eight seconds. In the boundary conditions, a rigid plane was used to compress the cone fender from its original position to 50% deflection, corresponding to a displacement of 200 millimeters. The plots in Figure 6.21, Figure 6.22 and Figure 6.23 show the resulting force displacement curve for each load profile. With a rest period of three seconds, it stabilizes at 7.7%, with five seconds at 6.8% and with eight seconds at 4.9% deflection.

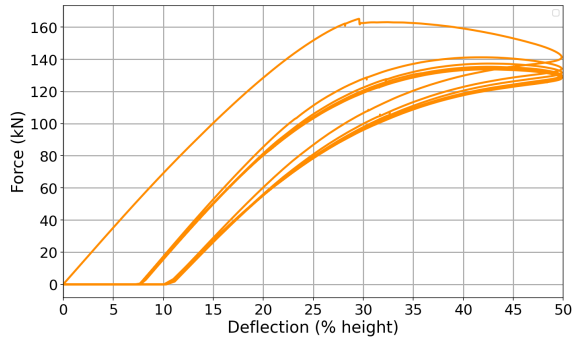

(a) Force deflection curves

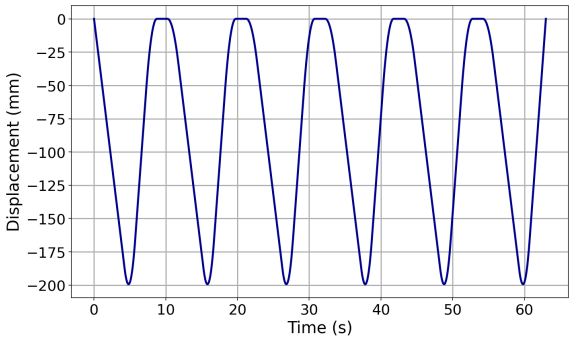

(b) Cyclic loading profile 6 cycles with 3 second pause

Figure 6.21: Force defection curves corresponding to load profile (3 seconds between cycles)

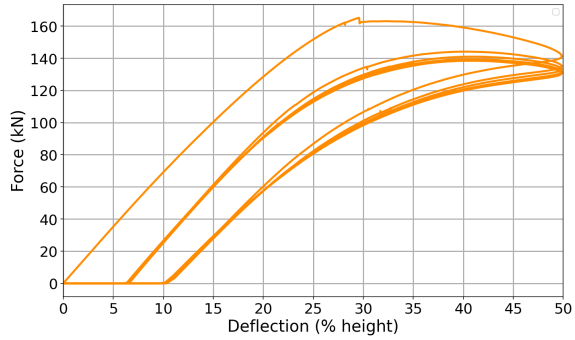

(a) Force deflection curves

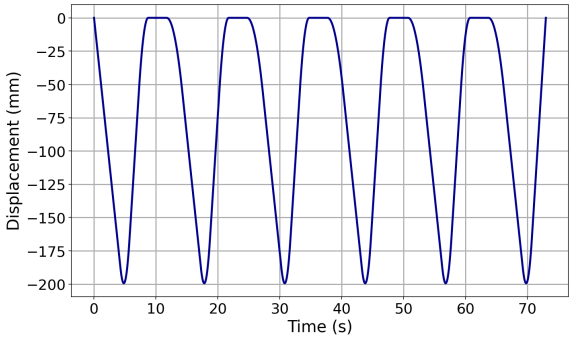

(b) Cyclic loading profile 6 cycles with 5 second pause

Figure 6.22: Force defection curves corresponding to load profile (5 seconds between cycles)

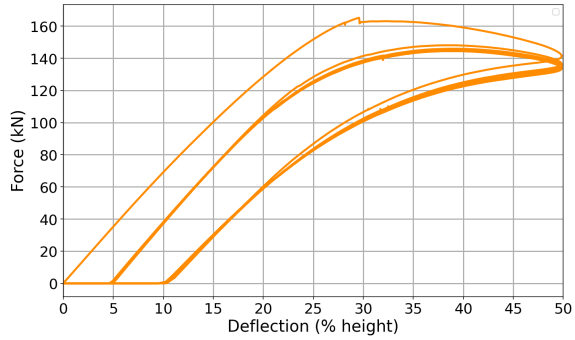

(a) Force deflection curves

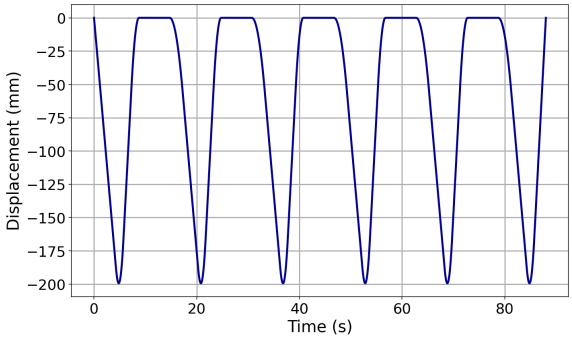

(b) Cyclic loading profile 6 cycles with 8 second pause

Figure 6.23: Force defection curves corresponding to load profile (8 seconds between cycles)

To determine the influence of stabilized deflections on the cone fender exposed to cyclic loading, the load cycles with the shortest rest period of three seconds with respect to the critical elements were further analyzed. The three-second rest period resulted in a delayed deflection of 7.7%. In Figure 6.24 the maximum, medium, and minimum principal stresses are plotted corresponding to this load profile. It can be observed that the stress behavior in the first load cycle is notably different compared to the second load cycle. The difference is clearly visible in the minimum principal stresses of elements two and three. After six load cycles, the stress response of the critical elements stabilizes, which aligns with the stabilization of the force deflection curve that represents the total reaction force of the system. The average decrease in the maximum principal stress across the critical elements over six load cycles is 3.7%. Furthermore, the minimum value of the maximum principal stress of the stabilized load cycle

across all critical elements is zero, with the exception of critical element three that is stabilizing at a stress of 0.04 MPa. Since the maximum principal stress has proven to be a suitable damage parameter, a loading ratio of zero was selected for the critical elements. It is important to note that a loading ratio of zero corresponds to the shortest fatigue life for rubber in general, but also according to the data set discussed in chapter 5. Therefore, it is convenient to select this loading ratio for the prediction of its service life, as it is applied to all critical elements, with the exception of critical element two. Element two has a loading ratio of 0.02, close to zero and a negligible difference in practice.

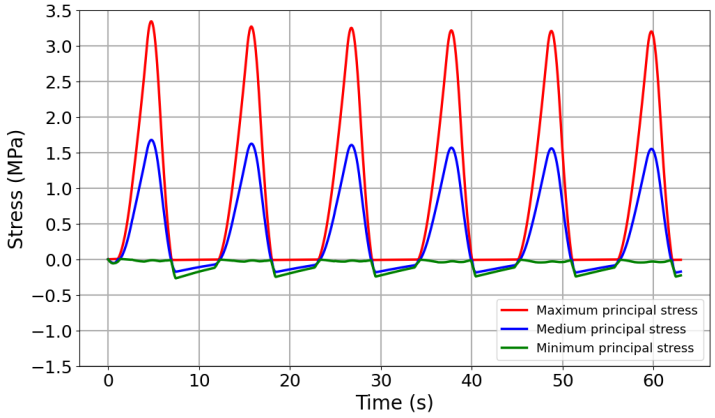

(a) Critical element one

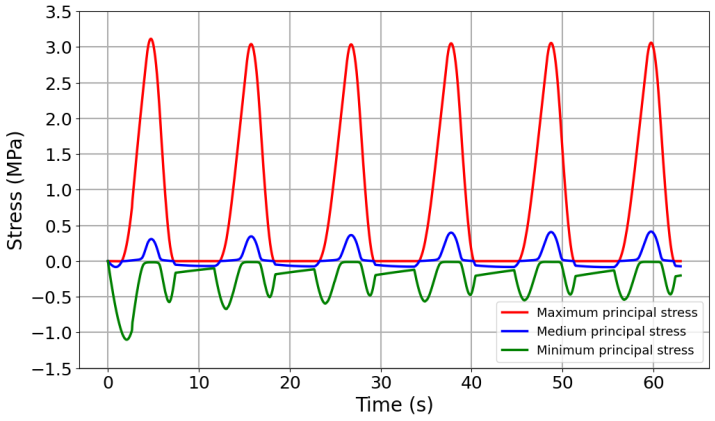

(b) Critical element two

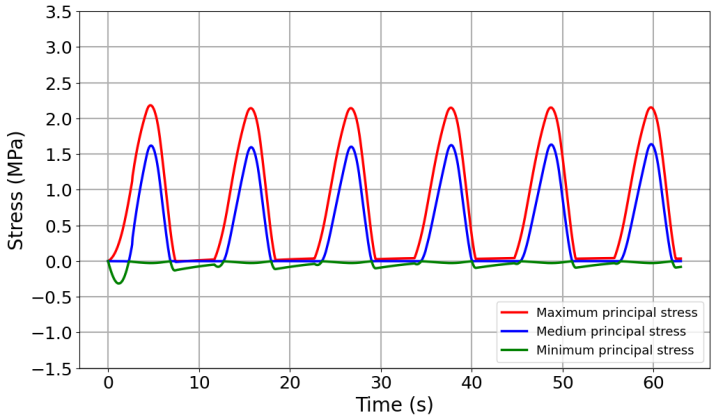

(c) Critical element three

Figure 6.24: Evolution principal stresses critical elements cyclic loading 3 second pause (7.7% residual deformation)

6.7. Number of cycles to crack initiation

Since the maximum principal stress is a suitable damage parameter and the loading ratio corresponding to the maximum principal stress of the critical elements selected within the FEA model is equal to zero. The relation defined in Eq. 6.5 is used to predict the number of cycles to crack initiation. Here is σ, the maximum principal stress in MPa. The predictions are given in Table 6.1 and Figure 6.25 represents the number of cycles until crack initiation for each deflection using a polynomial fit between the calculated predictions in the table. The corresponding polynomial relation is given in Eq. 6.6, here represents x the deflection (% height). The graph shows the most reduction in service life in the range from 10% to approximately 30% deflection.

$$N_f = 1.26 \times 10^6 \cdot \sigma^{-2.62} \tag{6.5}$$

Table 6.1: Predicted number of cycles until crack initiation for cone fender

Deflection (% height)	Max principal stress (MPa)	Cycles until crack initiation
10	0.15	181556351
20	0.54	6331387
30	1.18	816656
40	2.21	157783
50	3.45	49122
60	4.92	19383
70	5.70	13181

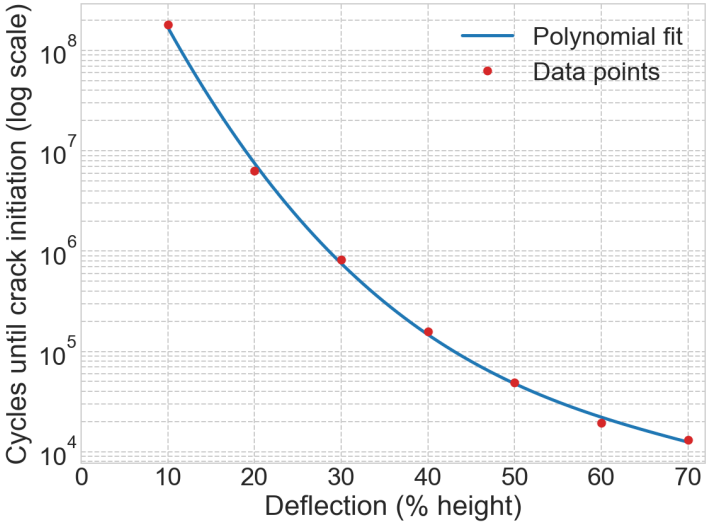

Figure 6.25: Deflection cone fender versus number of cycles until crack initiation using polynomial fit

$$\log_{10}(Cycles) = -1.1 \times 10^{-5}\, x^3 + 2.5 \times 10^{-3}\, x^2 - 2.0 \times 10^{-1}\, x + 1.0 \times 10^1 \tag{6.6}$$

6.8. Crack propagation

The direction of the maximum principal stress is a promising parameter when material rotations are taken into account to predict the crack propagation path, as explained in subsection 5.3.1. Therefore, the direction of the maximum principal stress is shown in the undeformed configuration in Figure 6.26 for the cone fender at 30% compression. For deflections beyond 30%, only the magnitude of the principal changes, while the change in direction is negligible small. Four zones (A,B,C and D) could be identified where the direction of the maximum principal stress differs significantly.

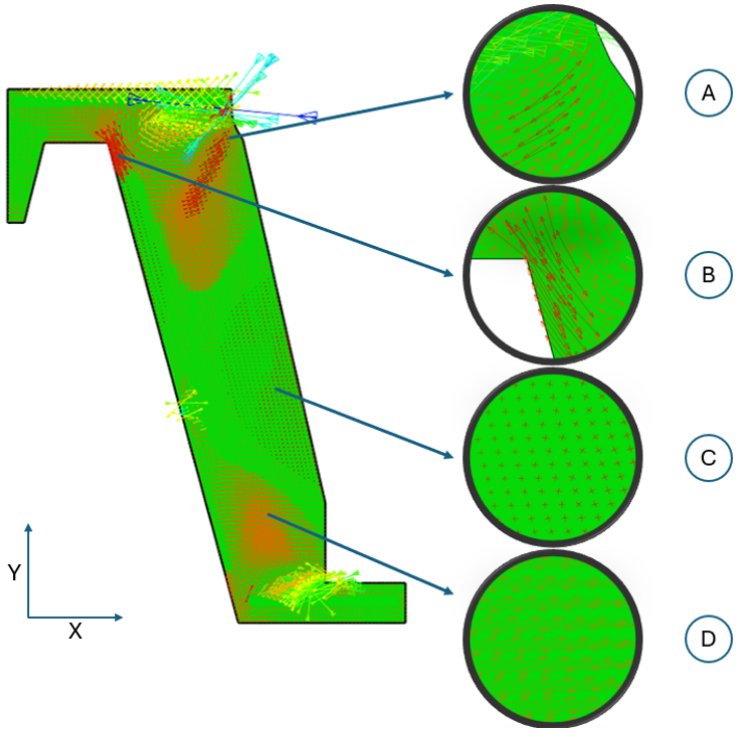

Figure 6.26: Principal stress directions undeformed configuration at 30% compression

The direction vectors of the maximum principal stresses are given with polar coordinates in Table 6.2. According to the theory [60], the path of crack propagation will occur in a specific plane that is perpendicular to the maximum principal stress. For this analysis, it is assumed that the crack propagates along the outer-surface of the cone fender while the crack growth along the thickness of the cone is neglected. Furthermore, it is also assumed that the directions of all the maximum principal stresses remain unchanged when a crack initiates. The result of the prediction is shown in Figure 6.27a. In Figure 6.27b a picture of a failed cone fender in practice is demonstrated. A clear observation is that the crack in practice propagates parallel to the qua wall at the bottom, and there also appears to be a tendency toward parallel cracking at the top. This aligns with the prediction, although the crack is not fully developed here. However, in practice, the crack along the height of the cone is observed to propagate at an angle less than 90 degrees relative to the qua wall. One possible explanation could be that in the FEA it was assumed that the cone fender is loaded purely axially, and in practice shear forces might also have an impact that was not taken into account. In addition to this, the directions of all the maximum principal stresses will most likely change when a crack initiates depending on the location of crack initiation.

Table 6.2: Direction of the first principal stress

Zone	Direction first principal stress $\vec{n}_1$ (r,z,θ)
A	$\begin{pmatrix} -0.82 \\ -0.57 \\ 0 \end{pmatrix}$
B	$\begin{pmatrix} -0.47 \\ 0.89 \\ 0 \end{pmatrix}$
C	$\begin{pmatrix} 0 \\ 0 \\ 1 \end{pmatrix}$
D	$\begin{pmatrix} -0.97 \\ -0.22 \\ 0 \end{pmatrix}$

(a) Crack propagation path prediction

(b) Failed cone fender in practice [32]

Figure 6.27: Comparison prediction and failed cone fender in practice

7

Cone fender optimization

In this chapter, an optimization of the example cone fender design is performed to enhance its suitability for a large number of small berthing energies. According to the theory of rubber fatigue, the new proposed design has a longer service life with small berthing energies up to the maximum principal stress limit while maintaining the efficiency ratio up to that specific point. Initially, a geometric variation analysis was carried out. Based on the insights gained from FEA, a new design is proposed.

7.1. Mathematical formulation of optimization problem

The equations below represent the optimization approach followed to obtain a design that is more suitable for a large amount of small berthing energies. The ultimate goal is to maximize energy absorption $E_{\sigma_{max}}$, up to the defined maximum principal stress limit of 1.8 MPa, which corresponds to a deflection of the original design of 35% according to FEA. Let $x \in R^n$ denote the set of design parameters. The boundary conditions are defined such that the minimum energy absorption until the stress limit is reached is at least equal to that of the original design, which corresponds to 14.6 kJ. In addition to this, the efficiency $\eta_{\sigma_{max}}$ must be at least 0.63, corresponding to the efficiency of the original design at the stress limit, to ensure that the reaction force on the structure and the vessel hull remain within reasonable limits relative to energy absorption. The efficiency can also be interpreted as a dimensionless number that indicates how much energy is absorbed relative to its theoretical maximum. In addition, the maximum reaction force $F_{\mathsf{max},\sigma_{max}}$, reached until the stress limit must not exceed 200 kN, while the maximum reaction force in the original design is approximately 164 kN. The total energy absorbed until time step i is calculated with the trapezoidal rule according to Eq. 7.2. The force deflection curve of the optimal design is given in Figure 7.1. Note that this design is only considered optimal when the maximum principal stress limit is reached at 50% deflection. This will have the highest possible value for $E_{\sigma_{max}}$, the maximum energy absorbed up to the stress limit for the investigated range (0-50%) while satisfying the boundary conditions.

$$\textbf{Maximize} : \mathbf{E}_{\boldsymbol{\sigma}_{\mathbf{max}}}(x) \tag{7.1}$$

$$E_i(x) = E_{i-1}(x) + \frac{F_i(x) + F_{i-1}(x)}{2} \cdot \Delta d_i, \qquad E_0 = 0 \tag{7.2}$$

$$F_{\max,i}(x) = \max_{0 \le j \le i} F_j(x) \tag{7.3}$$

$$\eta_i(x) = \frac{E_i(x)}{F_{\mathsf{max},i}(x) \cdot d_i} \tag{7.4}$$

$$\sigma_{\mathsf{max}}(x) = 1.8\ MPa \tag{7.5}$$

$$E_{\sigma_{max}}(x) \geq 14.6\ kJ \tag{7.6}$$

$$\eta_{\sigma_{max}}(x) \geq 0.63 \tag{7.7}$$

$$F_{\text{max},\sigma_{max}}(x) \leq 200\ kN \tag{7.8}$$

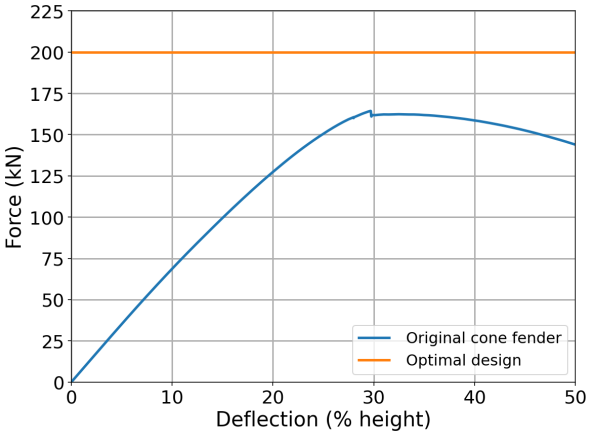

Figure 7.1: Optimal design according optimization problem

7.2. Geometric variation analysis

To gain insight into how small changes in the current cone fender design affect the fender characteristics, a geometric variation analysis was performed. The key geometric parameters used are shown in Figure 7.2. For each parameter, five different concepts were simulated, including the original design, while the other parameters, including the height of 400 millimeters were kept unchanged. The force displacement curves were plotted for each concept, and the point at which the maximum principal stress limit occurred was indicated with a bullet point. In addition, the most important characteristics for each concept were plotted in a bar chart.

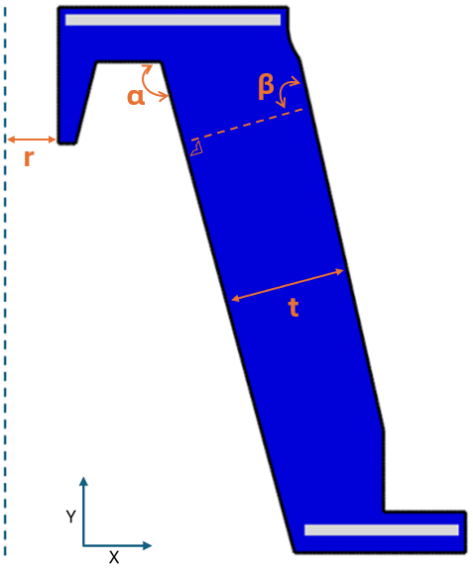

Figure 7.2: Key geometric parameters cone fender

7.2.1. Visualization modification key geometric parameters

The modifications of the key geometric parameters investigated are visualized below in the FEA model with respect to the axisymmetric element. The type and size of the mesh was kept the same during the analysis.

Modifications angle α

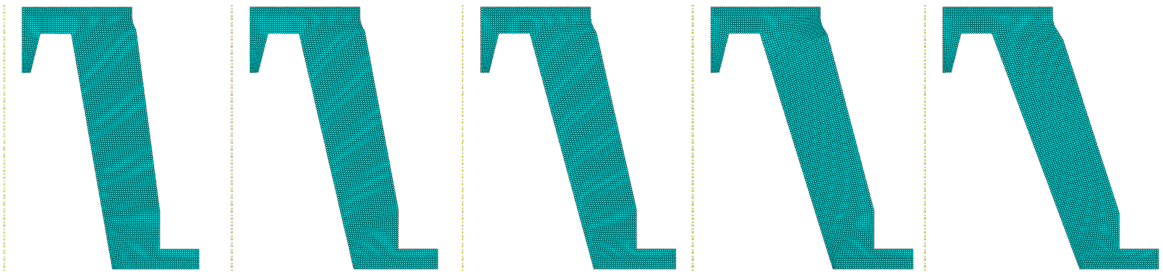

(a) $\alpha^* = \alpha - 5.0^\circ$ **(b)** $\alpha^* = \alpha - 2.5^\circ$ **(c)** Original cone fender **(d)** $\alpha^* = \alpha + 2.5^\circ$ **(e)** $\alpha^* = \alpha + 5.0^\circ$

Figure 7.3: Axisymmetric element with variation in angle α^*

Modifications distance r

(a) $r^* = 0.25r$ **(b)** $r^* = 0.50r$ **(c)** Original cone fender **(d)** $r^* = 2.0r$ **(e)** $r^* = 4.0r$

Figure 7.4: Axisymmetric element with variation in distance r^*

Modifications average thickness t

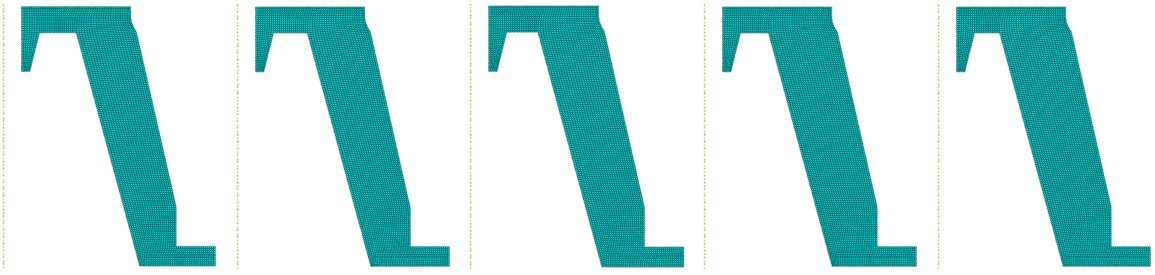

(a) $t^* = 0.90t$ **(b)** $t^* = 0.95t$ **(c)** Original cone fender **(d)** $t^* = 1.05t$ **(e)** $t^* = 1.10t$

Figure 7.5: Axisymmetric element with variation in averaged thickness t^*

Modifications angle β by changing inside axis

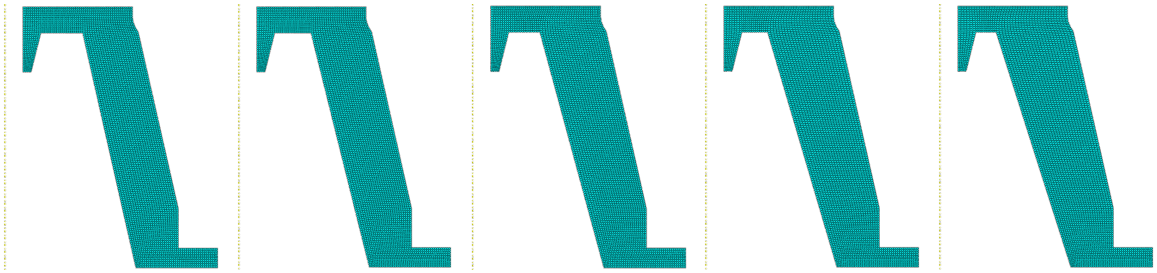

(a) $\beta^* = \beta - 2$ **(b)** $\beta^* = \beta - 1$ **(c)** Original cone fender **(d)** $\beta^* = \beta + 1$ **(e)** $\beta^* = \beta + 2$

Figure 7.6: The influence of angle variation β^* by changing the inside axis

Modifications angle β by changing outside axis

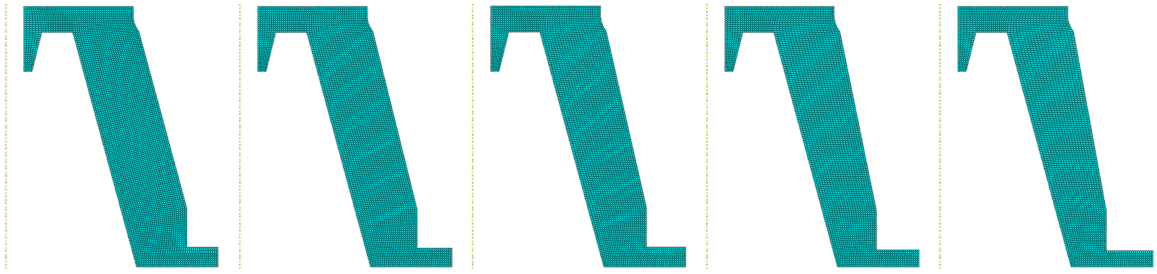

(a) $\beta^* = \beta - 2$ **(b)** $\beta^* = \beta - 1$ **(c)** Original cone fender **(d)** $\beta^* = \beta + 1$ **(e)** $\beta^* = \beta + 2$

Figure 7.7: The influence of angle variation β^* by changing the outside axis

7.2.2. Force deflection curves

The force deflection curves of the modification in key geometric parameters are given in Figure 7.8. The bullet points represent the deflection at which the maximum principal stress limit occurred.

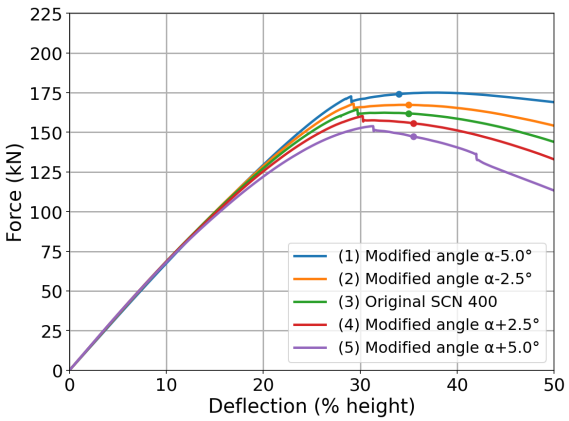

(a) Modifications angle α

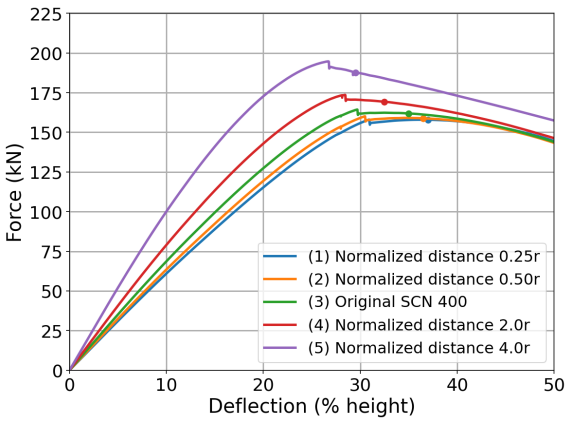

(b) Modifications distance r

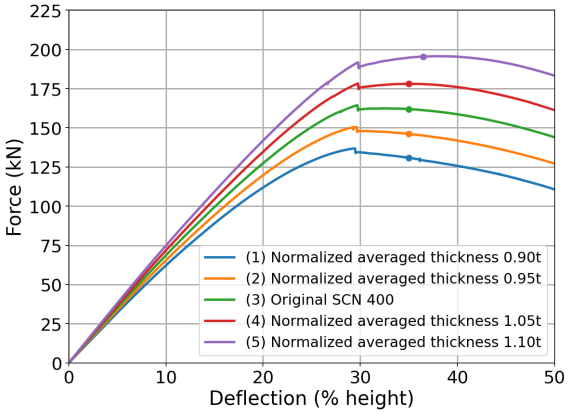

(c) Modifications averaged thickness t

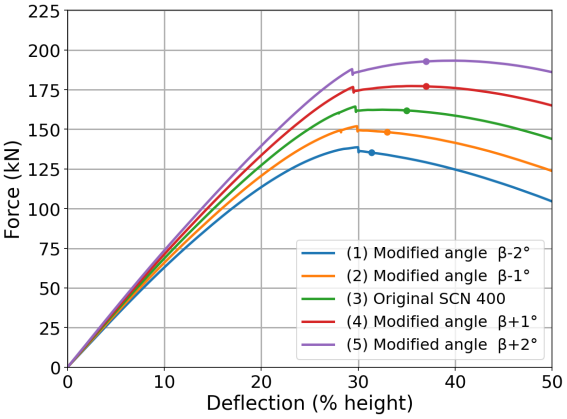

(d) Modifications angle β inside axis

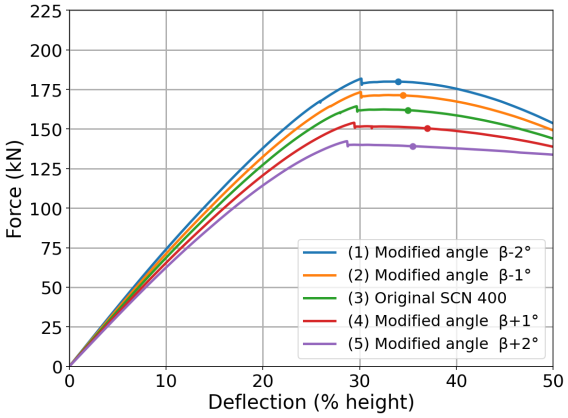

(e) Modifications angle β outside axis

Figure 7.8: Force deflection curves modifications key geometric parameters

7.2.3. Important characteristics

The most important characteristics of the modification in key geometric parameters are illustrated in the bar charts in Figure 7.9. The bar graph includes energy absorption up to the maximum principal stress limit, the maximum reaction force, and the efficiency at the maximum principal stress limit. The scenarios in red do not meet the boundary conditions, whereas the scenarios in green satisfy the boundary conditions. The dark green scenario is considered optimal, achieving the highest absorbed energy while satisfying all the boundary conditions.

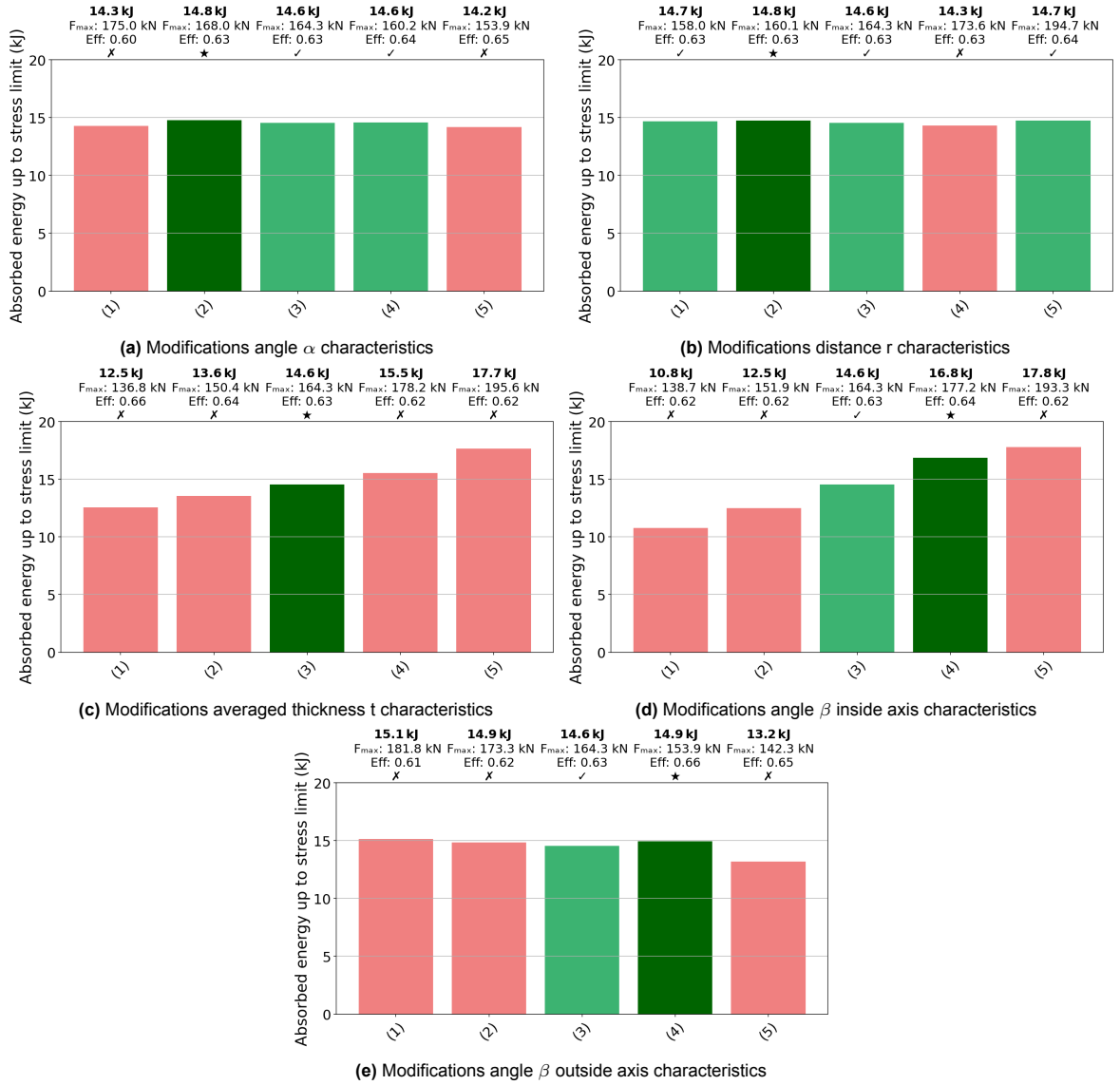

Figure 7.9: Characteristics modifications key geometric parameters

7.2.4. Conclusion geometric variation analysis

Based on the geometric variation analysis, it can be concluded that even a small change in the geometry affects the force deflection curve associated with characteristics such as the maximum reaction force, the amount of energy absorbed, and the efficiency. The most important finding of the analysis was that changes in angle α, average thickness t, and angle β by changing the outside axis did not shift the point when the maximum principal stress limit occurred along the deflection (%) axis. This means that the stress limit occurred at approximately the same percentage of deflection independent of the reaction force. However, when changing the distance r and the angle β by varying the inner axis, the point at which the maximum principal stress limit occurred depends on the percentage of deflection. In addition, the initial stiffness of the cone could be significantly influenced by changing the distance r. Since there was expected to be an optimum between these two parameters. That is, achieving the highest possible stiffness before buckling, while at the same time increasing the point at which the maximum principal stress limit takes place in terms of deflection. These two parameters will be further explored in section 7.3. Furthermore, the elements where the maximum principal stress limit was first observed during compression were often located in the sharp inner corner, as shown in Figure 7.10. To minimize this, it was decided to round the inner corner for further analysis. This corner will remain rounded in the study of the two parameters in section 7.3.

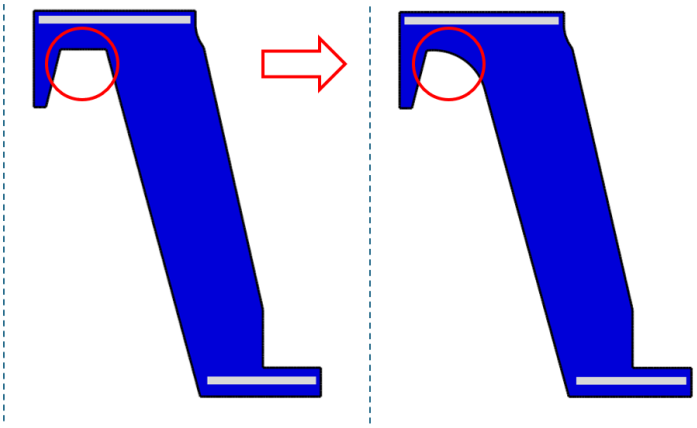

Figure 7.10: Rounded corner to prevent high principal stresses

7.3. Analysis two important parameters with rounded corner

Since in section 7.2 it was found that rounding the sharp angle reduces high stresses, and it is highly likely that there is an opium between the parameters r and β, these parameters were further investigated. In total, 20 concepts were made, including the rounded corner and four variations of r and five variations of β. The force deflection curves are given in Figure 7.11 and the bar chart in Figure 7.12 represents the most important characteristics of each concept. Based on the optimization approach, it can be concluded that the concept with geometry modifications 2r and β+2 (nr.10) is the most optimal variant that satisfies all boundary conditions while maximizing energy absorption up to the defined stress limit.

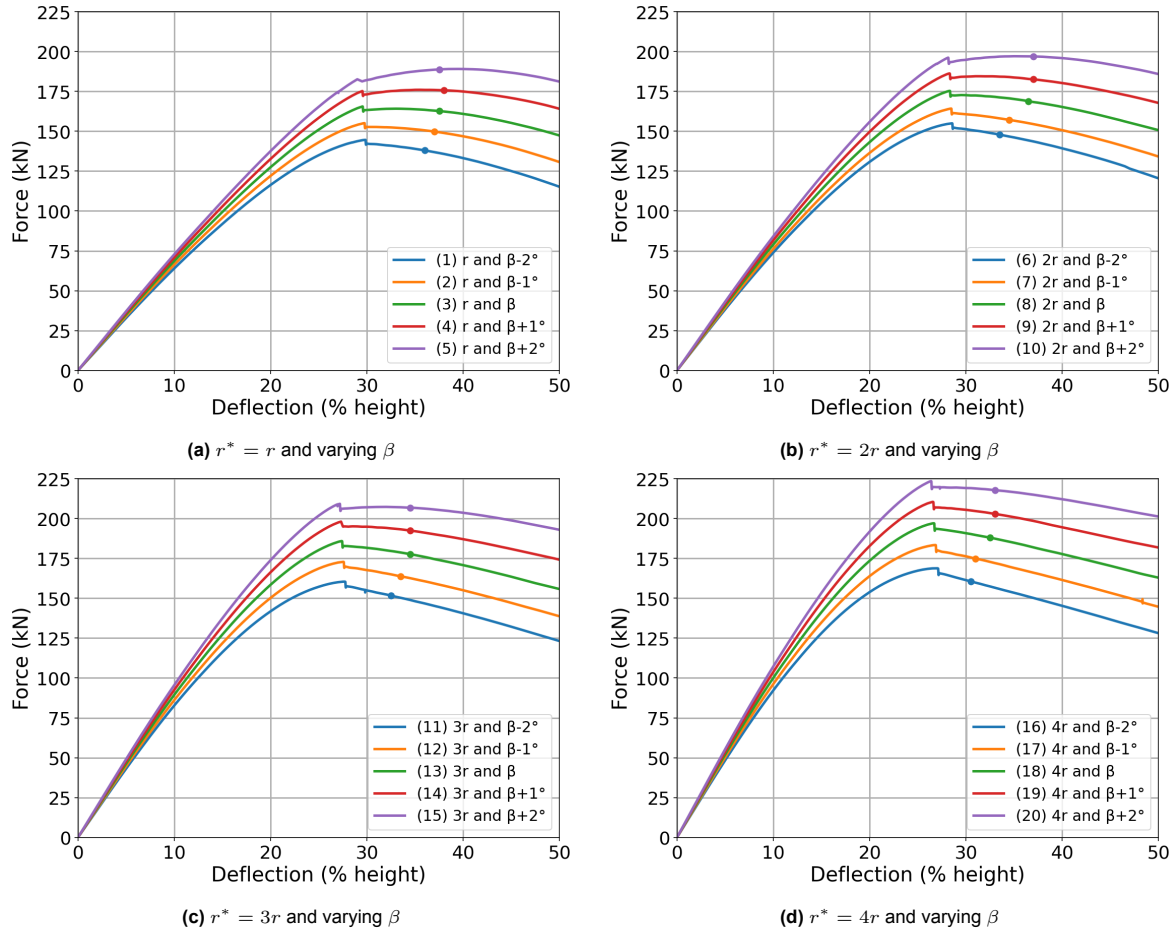

(a) $r^* = r$ and varying β

(b) $r^* = 2r$ and varying β

(c) $r^* = 3r$ and varying β

(d) $r^* = 4r$ and varying β

Figure 7.11: Multiple combinations of geometry parameters β and r

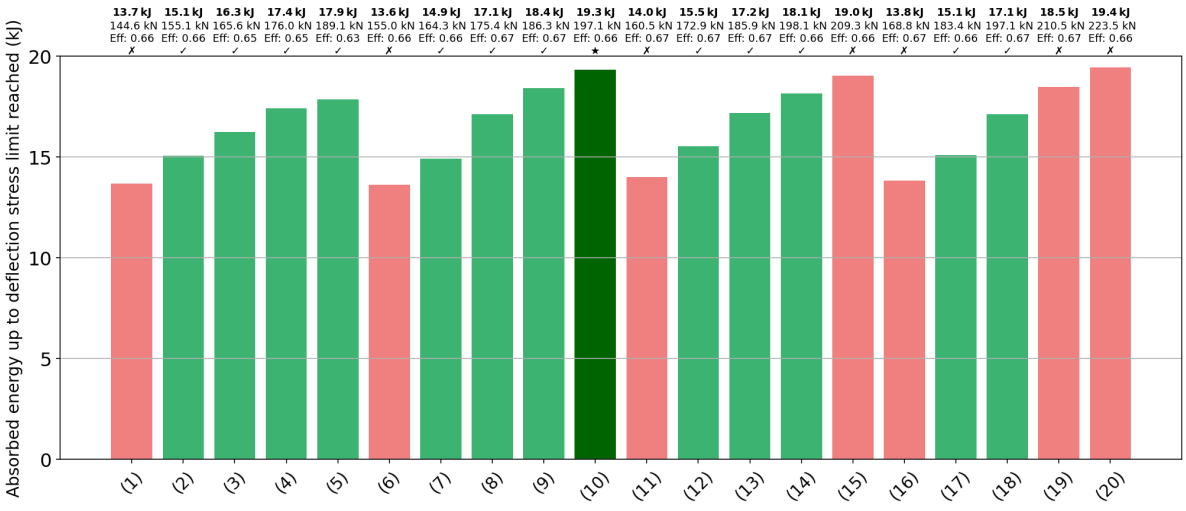

Figure 7.12: Important characteristics combinations geometry parameters β and r

7.4. Proposed concept

The original cone fender and the proposed concept are placed side by side in Figure 7.13. The proposed concept is capable of absorbing 32% more energy until the point at which the maximum principal stress limit of 1.8 MPa takes place. In addition, the efficiency at the stress limit is 5% higher in the proposed design. The force displacement curves of the two models are given in Figure 7.13. In addition to its suitability for its characteristics before buckling, the proposed model also demonstrates proper post buckling behavior.

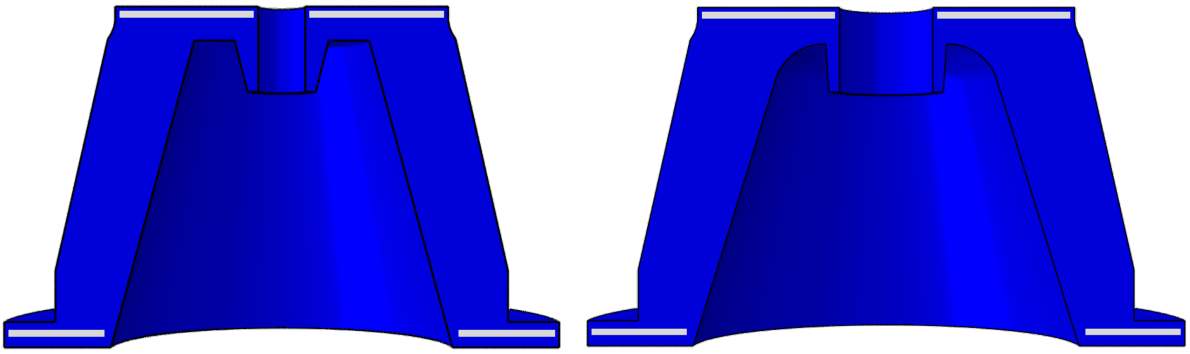

(a) Original cone fender **(b)** Proposed concept

Figure 7.13: Comparison original cone fender and proposed concept

Table 7.1: Important characteristics comparison original cone fender and proposed concept

Important parameters	Original cone fender	Proposed concept
$E_{i,\sigma_{max}}$	14.6 kJ	19.3 kJ
$\eta_{i,\sigma_{max}}$	0.63	0.66
$F_{\text{max, i},\sigma_{max}}$	164.3 kN	197.1 kN

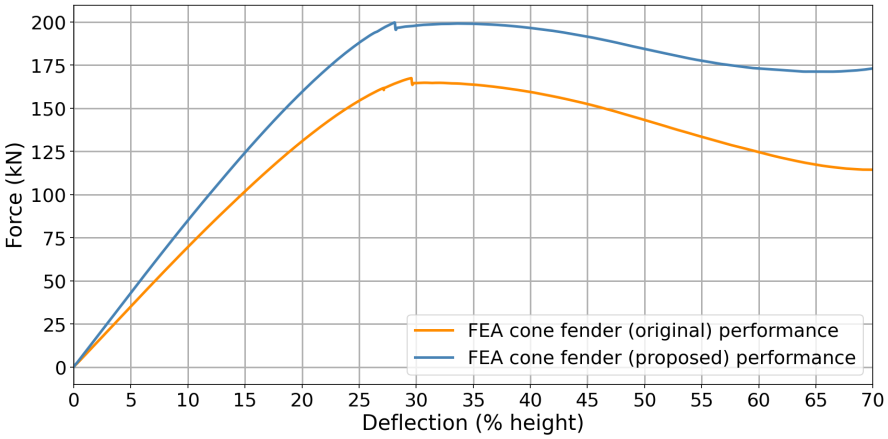

Figure 7.14: FEA model original and proposed performance

7.4.1. Case study

Based on the optimization approach that resulted in a proposed concept, a case study was performed to determine the enhanced service life of the cone fender when subjected to cyclic loading conditions. The parameters of the case study with the corresponding results can be found in Table 7.2. Since cyclic loading typically occurs at deflections smaller than the buckling point (30% deflection) [20]. Three

energy cases were selected that resulted in a maximum defection of approximately 30% for the largest energy case. The maximum principal stress development is shown in the undeformed configuration for each energy case for both the original and the proposed design. The service life is calculated according to Eq. 6.5 using the highest value of the maximum principal stress. It can be concluded that for the three cases investigated, this results in an average improved service life of 83%. In addition to this, not only was the highest value of the maximum principal stress lowered in the proposed design, but the average stress development also decreased. This is clearly visible in the contour plots for each energy case.

Table 7.2: Comparison of fender performance (original vs. proposed) three energy cases cyclic loading

Case	Energy (kJ)	Design	Deflection (%)	Max stress (MPa)	Service life (cycles)	Life increase (%)
1	4.0	Original Proposed	17.0 15.4	0.38 0.31	15897818 27102097	70
2	8.0	Original Proposed	24.5 22.3	0.81 0.66	2188465 3742531	71
3	12.0	Original Proposed	30.7 27.4	1.28 0.97	659903 1364673	107

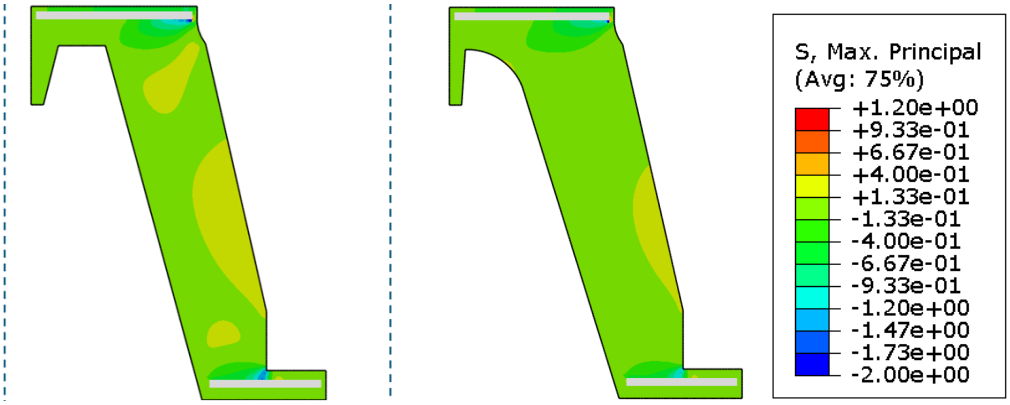

(a) Original cone fender (17.0% deflection) **(b)** Proposed concept (15.4% deflection) **(c)** Contour plot scale

Figure 7.15: Maximum principal stress development undeformed configuration case one (4 kJ)

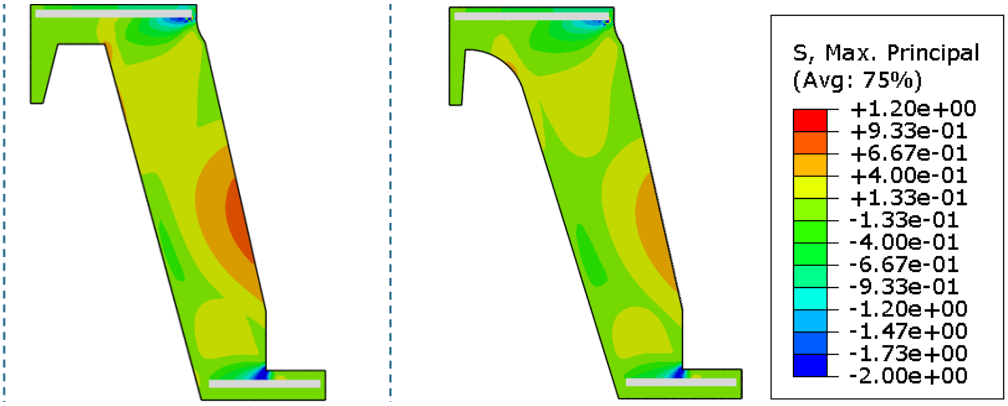

(a) Original cone fender (24.5% deflection) **(b)** Proposed concept (22.3% deflection) **(c)** Contour plot scale

Figure 7.16: Maximum principal stress development undeformed configuration case two (8 kJ)

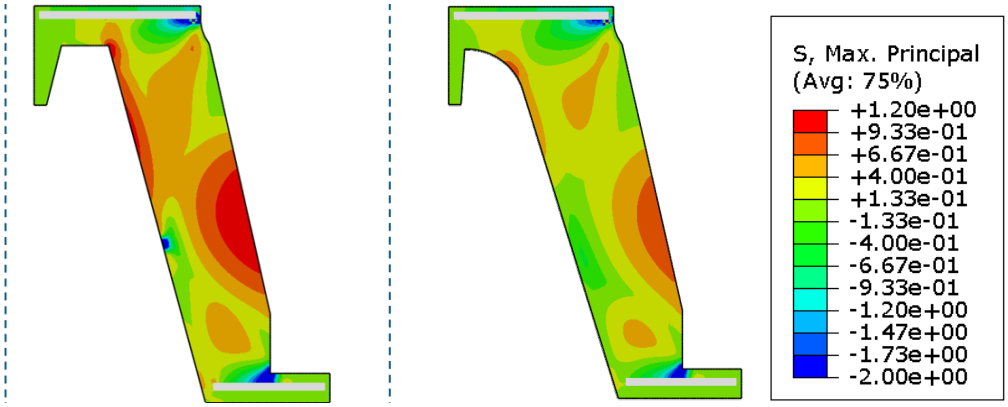

(a) Original cone fender (30.7% deflection) **(b)** Proposed concept (27.4% deflection) **(c)** Contour plot scale

Figure 7.17: Maximum principal stress development undeformed configuration case three (12 kJ)

8

Discussion

This thesis represented a framework for predicting the service life of rubber marine cone fenders subjected to cyclic loading. A polynomial fit was defined between the percentage of deflection and the number of cycles until crack initiation. In the range of 10% to 30% deflection a steep decrease was found. This implies that even a small reduction in deflection within this range can lead to a significant increase in service life for the cone fender studied. When the compression velocity was increased by a factor of eight, the average stress among the critical elements increased with 37% near the buckling phase, resulting in a reduction of 56% of its predicted service life. This highlights the importance of using a rate dependent model instead of a hyperelastic model.

Uniaxial compression tests were performed until a true strain of approximately -0.5 due to high levels of friction with the steel plates for values smaller than -0.5 which is not desired. However, the minimum true strain of the FEA model was found to be -0.85 at 70% deflection of the cone fender. This difference could potentially result in the observed deviation of the force deflection curve of the FEA model compared to the experimental curve with large deflections. The Bergström-Boyce implementation in Abaqus was fitted to the experimental data of the uniaxial tension and compression tests at different strain rates with a normalized mean absolute difference of 9.4%. Using some additional equibiaxial and planar tests, this difference could most likely be reduced for more accurate insights. Furthermore, the absolute values of the maximum principal strain rate of 1.2/s and the minimum principal strain rate of -1.4/s were higher than the values captured in the experimental tests. However, since the duration of these rates is less than 0.1 seconds during a compression cycle (0-50%) of 5 seconds, and the average values of the evolution of the strain rate ($\pm$0.1/s) correspond to the values captured in the tests, the strain rates tested were expected to be sufficient.

To make a cone fender more suitable for cyclic loading, it is important to keep the maximum principal stress in the cone as low as possible. Since stresses increase rapidly up to the buckling point, it is recommended to keep the deflection below 30% in any case. The initial stiffness of the cone fender can be increased by increasing the inner distance (r), while keeping the height constant. However, it is important to note that this leads to greater forces on the structure. By varying the inner axis (β), the deflection at which the defined stress limit was reached could be shifted. These two parameters were found to be important, particularly in the case of cyclic loading, where deflections occur largely up to the buckling point. Depending on the situation, these two parameters can be adjusted to maximize energy absorption for a certain stress limit. It should be noted, that in some cases the stress increased after the defined stress limit which is an important factor to consider. Furthermore, the question arises of whether the chosen value of this stress limit influenced the results obtained with the corresponding conclusions.

The rounded corner led to a reduction in stress development and had a negligible influence on overall performance. This makes this beneficial not only for cases with cyclic loading, but also across the entire deflection range. The proposed design exhibits a promising force deflection curve even after the buckling phase. However, the validity of its post buckling behavior is questionable since the original design does not fully align with the experimental post buckling results. Therefore, it is recommended to validate this first by ensuring a perfect match between the original force deflection curve and the experimental results. This will, consequently, allow for proper validation of the proposed design.

8.1. Recommendations for future research

This thesis led to the following recommendations for future work, as they are not sufficiently understood in literature and relevant for this research.

- **Investigating heat built up due to hysteresis of rubber:** Heat built up due to hysteresis might play a significant role in the reduction of fatigue life of rubber when subjected to cyclic loading. Many studies focused on the influence of the ambient temperature on the rubber, but here they often neglect the self-heating effect due to its viscoelasticity. Therefore, it is recommended to investigate this effect further.
- **Microstructure investigation rubber:** After a large number of load cycles, the microstructure of the rubber changes. The exact nature of these changes and their impact on mechanical properties are still not fully understood. Doing a study with lab-scale specimens using, for example, an X-ray CT with various cyclic loading tests can help to detect microstructure changes. This results in a better understanding what is physically happening inside the material with the associated damage mechanisms.
- **Effect variable loading amplitude on fatigue life rubber:** Most of the fatigue tests performed in the laboratory are based on a constant amplitude. In practice, these load amplitudes often vary over time. Therefore, a damage model capable of converting load histories with different amplitudes into equivalent damage is needed.
- **The influence of fillers on fatigue life:** Carbon black, silica, and nano fillers are often added to rubber. The influence of the exact filler with the corresponding concentration on the fatigue life of the rubber could significantly influence crack initiation and propagation. Therefore, optimizing filler selection and concentration is recommended with experimental validation and micro structural analysis.
- **Investigating impact environmental conditions:** Rubber is often exposed to high temperatures, UV radiation, ozone, and salt. The combination of environmental conditions can significantly reduce its fatigue life as a result of aging. Therefore, it is recommended to include environmental aging in experimental tests to capture this in fatigue life predictions.

8.2. Recommendations Trelleborg

The following recommendations are recommended for Trelleborg to conduct a deeper analysis of this study.

- **Scalability cone fenders:** This study focused on an example cone fender of Trelleborg with a height of 400 millimeters. It is recommended to investigate internal stress development and consequently service life between different cone fender sizes. Although the dimensionless force deflection curve appears to be similar for all sizes, larger cone fenders may experience different stress concentrations due to scale effects. Additional numerical studies are therefore required to confirm whether the current service life predictions can be applied for al cone fender sizes.
- **Including radial forces in FEA:** This study assumed only axial compression, which allowed the model to be built with axisymmetric elements. However, in practice, radial forces will also play a role. This might lead to an overestimation of its service life. To investigate this, future research should develop an FEA model using full 3D elements, in which both axial and radial forces are applied to the model.
- **Experimental material calibration specimens:** The experimental calibration tests for the material model were performed using the first load cycle. However, the Mullins effect is still present here, meaning that the material becomes significantly less stiff over the first ten load cycles. Therefore, it might be more practical to apply at least ten pre-cycles before conducting the calibration tests. Furthermore, only uniaxial compression and tension tests were performed. To provide more input for the calibration of a suitable material model, it is convenient to perform some equibiaxial and planar tension/compression tests as well. This will likely result in an FEA model that corresponds more accurately to the stabilized experimental force deflection curve of the cone fender.

- **Selected material model:** The hysteresis material model in Abaqus was used with the Bergström Boyce implementation to simulate the behavior of rubber. During the analysis, it was observed that the deformation behavior of the cone fender differs significantly when a hyperelastic material model was selected as input. Although hyperelastic models are not rate dependent, they might provide accurate predictions at relatively low compression velocities, as some authors in the literature argue that hyperelastic material models show better agreement with their application. Therefore, it is relevant to compare the force deflection curves and the deformed shape of the cone fender with experimental cone fender data to determine which model matches the best with the real behavior.
- **Fatigue dataset:** The most suitable damage parameter found in this research was based on a dataset from the literature that contained fatigue data from natural rubber with carbon black in it. However, the calibration experiments to fit a material model were performed with the compound used in Trelleborg their cone fenders. The exact compound of the rubber formulation can have a significant influence on the number of cycles until crack initiation. Therefore, it is recommended to perform the fatigue experiments with the same compound as used in the calibration experiments. In addition to this, it is recommended to perform the fatigue experiments for both a uniaxial stress state and for a multiaxial stress state by using torsion tests for example due to the multiaxial stress state that develops during the compression of the cone fender. This will result in a more accurate service life estimation of the cone fender in practice.

9

Conclusion

This thesis aimed to understand the correlation between the local distribution of stress and strain within a rubber cone fender and how this correlates with crack initiation. This work followed a numerical approach with experimental calibration. By characterizing the mechanical properties of the compound in the laboratory, identifying a suitable damage parameter, and performing a finite element analysis with a commercial cone fender of Trelleborg, this thesis developed a framework for predicting the service life of rubber cone fenders subjected to cyclic loading.

Based on a uniaxial fatigue data set from the literature and the modeling of the specimen in finite element analysis, it was found that the maximum principal strain and the maximum principal stress exhibited the highest correlation for all loading ratios combined in the data set studied. Since multiaxial fatigue studies showed that the maximum principal stress successfully captured crack initiation, and the directions of crack growth, while the maximum principal strain failed in multiaxial fatigue. The maximum principal stress was chosen as the most suitable damage parameter to predict the service life of a rubber marine cone fender.

The most suitable loading ratio of a cone fender subjected to cyclic loading was investigated by applying load cycles to the FEA model with different frequencies. Three critical elements with relative high development of principal stress during compression were selected. The loading ratios for all the critical elements investigated were found to be approximately zero even for the highest frequency examined, corresponding to a residual deformation of 7.7% of the cone fender.

The average maximum and minimum principal strain rate across all elements in time was found to be approximately ±0.1/s during a constant compression cycle, ranging from 0 to 50% compression with a velocity of 40 mm/s. Relative high local values of the strain rate were found during the buckling phase of the cone fender inside the buckling element. The highest value of the maximum principal strain rate was here 1.2/s whereas the lowest value of the minimum principal strain rate was -1.4/s. For the critical elements, the strain rate scaled proportionally to the compression velocity of the cone fender.

The effect of loading velocity on the resulting stress states was evaluated for the critical elements. The average increase in stress among the critical elements was found to be the highest in the buckling phase during compression. When the loading velocity increased by a factor of eight, the average stress in this phase increased by 38%, corresponding to a reduction of 57% of its predicted service life.

Furthermore, the average increase in the maximum principal stress among the critical elements was found to be 26.8% at a strain of 0.3 when the strain rate increased by a factor of ten. This is 2.5% lower than the increase in stress in the uniaxial tension tests by a factor of ten difference in engineering strain rate. However, the compression velocity does not affect each critical element equally with respect to the maximum principal stress despite the proportional increase in the strain rate with the compression velocity. It was therefore observed that, at a strain of 0.3, the relative increase in maximum principal stress differed across the three critical elements despite the same increase in strain rate.

Finally, an optimization was performed on the original cone fender to enhance its suitability for a large number of relative small energies resulting in an enhanced service life. The goal was here to maximize the energy absorption until a defined stress limit of 1.8 MPa. A geometric variation analysis had been conducted that resulted in the selection of two important dimensional parameters. Focusing on the inner radius and the angle of the inner axis led to a design that achieved a 32% increase in energy absorption while satisfying the boundary conditions. Based on a case study with three energy cases, this resulted in an average improved service life of 83% for the energy cases investigated.

References

[1] PIANC Working Group 186. *Mooring of large ships at quay walls*. Tech. rep. 186. MARITIME COMMISSION, PIANC. PIANC, July 2024.

[2] PIANC Working Group 211. *Guidelines for the Design, Manufacturing and Testing of Fender Systems*. Tech. rep. 211. Maritime Navigation Commission, PIANC. PIANC, Mar. 2024.

[3] H. Akiyama et al. “Investigation on service years of large rubber marine fenders”. In: *Journal of JSCE* 5.1 (2017), pp. 392–401.

[4] E. M. Arruda and M. C. Boyce. “A three-dimensional constitutive model for the large stretch behavior of rubber elastic materials”. In: *Journal of the Mechanics and Physics of Solids* 41.2 (1993), pp. 389–412.

[5] M. Atiq, A. Shajib, and K. N. Hoque. “Analysis of Marine Fender Systems Minimizing the Impact of Collision Damage”. In: *SSRN Electronic Journal* (Jan. 2023). DOI: 10.2139/ssrn.4445128.

[6] G. Ayoub. “Comportement en grandes déformations et fatigue des polymères : modélisation constitutive et prédiction de la durée de vie en fatigue”. Thèse de doctorat. Université Lille 1 Sciences et Technologies, 2010.

[7] G. Ayoub et al. “Multiaxial fatigue life prediction of rubber-like materials using the continuum damage mechanics approach”. In: *Procedia Engineering* 2.1 (2010). Fatigue 2010, pp. 985–993.

[8] E.A. Berendsen. “STRUCTURAL CAPACITIES OF SHIP’S PARALLEL HULL SUBJECT TO FENDER-INDUCED BERTHING IMPACT LOADS”. In: *Proceedings of the 35th PIANC World Congres* (2024).

[9] J. S. Bergström and M. C. Boyce. “Constitutive modeling of the large strain time-dependent behavior of elastomers”. In: *Journal of the Mechanics and Physics of Solids* 46.5 (1998), pp. 931–954.

[10] A. Bower. *Mechanics of Solid Materials*. https://solidmechanics.org. Accessed: 18 March 2025. 2006.

[11] F. Carleo et al. “Modeling the Full Time-Dependent Phenomenology of Filled Rubber for Use in Anti-Vibration Design”. In: *Polymers* 12.4 (2020).

[12] O. D. Chaudhuri. “Viscoelasticity Acts as a Marker for Tumor Extracellular Matrix Characteristics”. In: *Nature Biomedical Engineering* 4.1 (2020), pp. 112–122.

[13] J. Chen et al. “Effect of microstructural damage on the mechanical properties of silica nanoparticle-reinforced silicone rubber composites”. In: *Engineering Fracture Mechanics* 235 (2020), p. 107195.

[14] N. L. Costa et al. “A Review of EPDM (Ethylene Propylene Diene Monomer) Rubber-Based Nanocomposites: Properties and Progress”. In: *Polymers* 16.12 (2024). ISSN: 2073-4360.

[15] Dassault Systèmes. *Abaqus 2024 Documentation*. Dassault Systèmes Simulia Corp. Providence, RI, USA, 2024.

[16] P. Del Estado. “ROM 3.1-99: recommendations for the design of the maritime configuration of ports, approach channels and harbour basins”. In: *Part V: Tug Boats* (2007).

[17] A. Elmaryami and B. Omar. “Developing 1D MM of Axisymmetric Transient Quenched Chromium Steel to Determine LHP”. In: *Journal of Metallurgy* 2012 (Mar. 2012). DOI: 10.1155/2012/539823.

[18] T. Fadhilah, S. Rizal, and H. Firman. “Port Congestion Solutions: The Future of Efficient Transport Networks in Global Trade”. In: *Shipping and Transport Management Journal* (2025).

[19] B. Fazekas and T. J. Goda. “Constitutive modelling of rubbers: Mullins effect, residual strain, time-temperature dependence”. In: *International Journal of Mechanical Sciences* 210 (2021), p. 106735. ISSN: 0020-7403.

[20] M. Gaal and M. Kumar. “Cyclic Conditions and Impact on Marine Fenders”. In: *35th PIANC World Congress, Cape Town, South Africa* (2024).

[21] W. Galor. “The analysis of effective energy of ship’s berthing to the quay”. In: *Journal of KONES* 19 (2012), pp. 185–191.

[22] H. P. Gavin. “The Levenberg-Marquardt algorithm for nonlinear least squares curve-fitting problems”. In: *Department of Civil and Environmental Engineering Duke University August* 3 (2019), pp. 1–23.

[23] T. Gehling et al. “Fatigue Behavior of Elastomeric Components: A Review of the Key Factors of Rubber Formulation, Manufacturing, and Service Conditions”. In: *Polymer Reviews* 63.3 (2023), pp. 763–804.

[24] P. Ghosh et al. “Investigation of fatigue crack growth characteristics of NR/BR blend based tyre tread compounds”. In: *International Journal of Fracture* 188 (2014), pp. 9–21.

[25] T. Gourlay and M. Kumar. “The effect of fender energy dissipation on moored ship wave-induced motions”. In: *Australasian Coasts & Ports 2021: Te Oranga Takutai, Adapt and Thrive: Te Oranga Takutai, Adapt and Thrive*. New Zealand Coastal Society Christchurch, NZ, 2022, pp. 483–489.

[26] G. Heinrich, R. Kipscholl, and R. Stoček. “Fatigue crack growth in rubber materials”. In: *Advances in polymer science. Springer Nature Switzerland AG* (2021).

[27] ANSYS Inc. *MCalibration*. Version 25.1. Material model calibration tool. Used with Qt version 6.5.5. 2025.

[28] W. Kang et al. “Basic mechanical and fatigue properties of rubber materials and components for railway vehicles: A literature survey”. In: *Reviews on Advanced Materials Science* 61.1 (2022), pp. 587–610.

[29] P. A. Kelly. *Mechanics Lecture Notes: An Introduction to Solid Mechanics*. `http://homepages.engineering.auckland.ac.nz/~pkel015/SolidMechanicsBooks/index.html`. Accessed: April 19, 2025. 2023.

[30] B. Kim et al. “A comparison among Neo-Hookean model, Mooney-Rivlin model, and Ogden model for chloroprene rubber”. In: *International Journal of Precision Engineering and Manufacturing* 13 (2012), pp. 759–764.

[31] W. D. Kim et al. “Fatigue life estimation of an engine rubber mount”. In: *International Journal of Fatigue* 26.5 (2004), pp. 553–560.

[32] M Kumar. *Consultant Meet Presentation*. Presentation, Trelleborg Marine & Infrastructure. 2018.

[33] R. Lattime. “Styrene-Butadiene Rubber”. In: *Kirk-Othmer Encyclopedia of Chemical Technology* (2000).

[34] E. Lefeber. “Tracking Control of Nonlinear Mechanical Systems”. In: *Eindhoven University of Technology* (Jan. 2000).

[35] Q. Li, J. Zhao, and B. Zhao. “Fatigue life prediction of a rubber mount based on test of material properties and finite element analysis”. In: *Engineering Failure Analysis - ENG FAIL ANAL* 16 (Oct. 2009), pp. 2304–2310. DOI: `10.1016/j.engfailanal.2009.03.008`.

[36] Y. Liu, W. Chen, and D. Jiang. “Review on heat generation of rubber composites”. In: *polymers* 15.1 (2022), p. 2.

[37] W. Luo et al. “Fatigue Life Assessment of Filled Rubber by Hysteresis Induced Self-Heating Temperature”. In: *Polymers* 12.4 (2020).

[38] N. F. A. Manan et al. “Numerical investigation of Ogden and Mooney-Rivlin material parameters”. In: *ARPN J. Eng. Appl. Sci* 10.15 (2015), pp. 6329–6335.

[39] M. A. Margalho de Barros, S. Govindjee, and J. Schröder. “A note on the nonlinear viscoelastic Schapery model applied to PMMA and asphalt”. In: *PAMM* 24.3 (2024).

[40] Trelleborg Marine and Infrastructure. *Fender Systems Product*. `https://www.trelleborg.com`. 2025.

[41] Trelleborg Marine and Infrastructure. *Rubber Fenders - Mixing it Up*. `https://www.trelleborg.com`. 2023.

[42] W.V. Mars. “Cracking energy density as a predictor of fatigue life under multiaxial conditions”. In: *Rubber chemistry and technology* 75.1 (2002), pp. 1–17.

[43] W.V. Mars and A. Fatemi. “A literature survey on fatigue analysis approaches for rubber”. In: *International Journal of Fatigue* 24.9 (2002), pp. 949–961.

[44] W.V. Mars and A. Fatemi. “Factors that affect the fatigue life of rubber: a literature survey”. In: *Rubber chemistry and technology* 77.3 (2004), pp. 391–412.

[45] G. Maugin. *Continuum Mechanics Through the Twentieth Century: A Concise Historical Perspective*. Vol. 196. springer, Jan. 2013.

[46] A. Mohammed, M.M. Nemat-Alla, and K.M. Emara. “Influence of cyclic loading on fatigue behaviour of SBR and NBR compounds with different contents of carbon black”. In: *JES. Journal of Engineering Sciences* 42.2 (2014), pp. 365–384.

[47] S.I. Moon et al. “Study on determination of durability analysis process and fatigue damage parameter for rubber component”. In: *Journal of mechanical science and technology* 25 (2011), pp. 1159–1165.

[48] H. Naghash, D. Schott, and J. Pruyn. “A review on global shipping projections and methodologies”. In: *Journal of Shipping and Trade* 9 (2024), p. 29.

[49] G. Neser and D. Unsalan. “Dynamics of ships and fenders during berthing in a time domain”. In: *Ocean engineering* 33.14-15 (2006), pp. 1919–1934.

[50] R. W. Ogden. “Large deformation isotropic elasticity–on the correlation of theory and experiment for incompressible rubberlike solids”. In: *Proceedings of the Royal Society of London. A. Mathematical and Physical Sciences* 326.1567 (1972), pp. 565–584.

[51] R. W. Ogden and D. G. Roxburgh. “A pseudo–elastic model for the Mullins effect in filled rubber”. In: *Proceedings of the Royal Society of London. Series A: Mathematical, Physical and Engineering Sciences* 455.1988 (1999), pp. 2861–2877.

[52] A. Ostadrahimi et al. “A Nonlinear Thermo-Visco-Green-Elastic Constitutive Model for Mullins Damage of Shape Memory Polymers under Giant Elongations”. In: *Journal of the Mechanics and Physics of Solids* 196 (2025), p. 106029. ISSN: 0022-5096.

[53] X. Qiu, H. Yin, and Q. Xing. “Research Progress on Fatigue Life of Rubber Materials”. In: *Polymers* 14.21 (2022).

[54] G. Raghvendra. *Profile of Raghvendra Gopal – Materials Info Consultancy*. https://www.corrosionpedia.com. Accessed: April 19, 2025. 2025.

[55] T. Rapp et al. “Determining Dynamic Properties of Elastomer-Dampers by Means of Impact Testing”. In: *Experimental Mechanics* 62 (Mar. 2022), pp. 1–14.

[56] H. S. Ro. “Modeling and interpretation of fatigue failure initiation in rubber related to pneumatic tires”. PhD thesis. Purdue University, 1989.

[57] J. Rojas Gregorio. “Microstructural characterization & viscoelastic properties of AlZnMg & AlCuMg alloys”. PhD thesis. Polytechnic University of Catalonia, Jan. 2011, p. 130.

[58] N. Saintier, G. Cailletaud, and R. Piques. “Crack initiation and propagation under multiaxial fatigue in a natural rubber”. In: *International Journal of Fatigue* 28.1 (2006), pp. 61–72. ISSN: 0142-1123.

[59] N. Saintier, G. Cailletaud, and R. Piques. “Fatigue life prediction of natural rubber components under uniaxial and multiaxial loading”. In: *Materials Center Pierre-Marie Fourt* (2006).

[60] N. Saintier, G. Cailletaud, and R. Piques. “Multiaxial fatigue life prediction for a natural rubber”. In: *International Journal of Fatigue* 28.5 (2006), pp. 530–539. ISSN: 0142-1123.

[61] R.J. Schaefer. “Mechanical properties of rubber”. In: *Harris’ Shock and Vibration Handbook* 6 (2010), pp. 33–1.

[62] R. A. Schapery. “Nonlinear viscoelastic and viscoplastic constitutive equations based on thermodynamics”. In: *Mechanics of time-dependent materials* 1 (1997), pp. 209–240.

[63] J. Schieppati et al. “Temperature impact on the mechanical and fatigue behavior of a non-crystallizing rubber”. In: *International Journal of Fatigue* 144 (2021), p. 106050.

[64] K. Shimizu, M. Yasui, and S. Yamase. “A Study of Durability for Marine Fenders with Reclaimed Rubber and Calcium Carbonate”. In: *The Twenty-fifth International Ocean and Polar Engineering Conference*. International Society of Offshore and Polar Engineers. 2015.

[65] W. Sikora, K. Michalczyk, and T. Machniewicz. “Numerical Modelling of Metal-Elastomer Spring Nonlinear Response for Low-Rate Deformations”. In: *Acta Mechanica et Automatica* 12 (Mar. 2018). DOI: 10.2478/ama-2018-0005.

[66] R. Stocek, O. Kratina, and I. Kuritika. “Focus on future trends in experimental determination of crack initiation in reinforced rubber”. In: *Chemicke Listy* 107 (2014), pp. 71–77.

[67] Trelleborg Marine Systems. *Correction Factor for Fender Systems: Velocity and Temperature Effects*. Accessed: 2025-01-23. 2025.

[68] L.-C. Tang et al. “Chapter Twelve - Mechanical Properties of Rubber Nanocomposites Containing Carbon Nanofillers”. In: *Carbon-Based Nanofillers and Their Rubber Nanocomposites*. Ed. by Srinivasarao Yaragalla et al. Elsevier, 2019, pp. 367–423. ISBN: 978-0-12-817342-8.

[69] Shibata Fender Team. *White Paper Series Part 1: Compounding*. https://www.shibata-fender.team/. Accessed: 2025-02-20. 2023.

[70] Coastal Development Institute of Technology (CDIT). *Guidelines for Design and Testing of Rubber Fender Systems*. Coastal Development Institute of Technology, 2019.

[71] Y. L. Tee, M. Loo, and A. Andriyana. “Recent advances on fatigue of rubber after the literature survey by Mars and Fatemi in 2002 and 2004”. In: *International Journal of Fatigue* 110 (May 2018). DOI: 10.1016/j.ijfatigue.2018.01.007.

[72] L. R. G. Treloar. *The Physics of Rubber Elasticity*. 4th ed. Oxford University Press, 2023. ISBN: 9780198570271.

[73] K. N. Ulu et al. “Fatigue resistance of natural rubber in seawater with comparison to air”. In: *International Journal of Fatigue* 88 (2016), pp. 247–256. ISSN: 0142-1123.

[74] University of Cambridge. *S-shaped stress-strain curves in bioelasticity*. https://www.doitpoms.ac.uk/. Accessed: 30-Jan-2025. 2024.

[75] G. Wang et al. “Fatigue Life Prediction of Radial Tire Bead Using a Maximum Strain Energy Density Range Method”. In: *Applied Sciences* 11.12 (2021). ISSN: 2076-3417. URL: https://www.mdpi.com/2076-3417/11/12/5477.

[76] K. Wang and B. Pierscionek. “Biomechanics of the human lens and accommodative system: Functional relevance to physiological states”. In: *Progress in Retinal and Eye Research* (Nov. 2018).

[77] X. Wang et al. “A method to develop a unified fatigue life prediction model for filled natural rubbers under uniaxial loads”. In: *Fatigue Fracture of Engineering Materials Structures* 37 (Jan. 2014). DOI: 10.1111/ffe.12081.

[78] X. Wang et al. “Rubber Fatigue Revisited: A State-of-the-Art Review Expanding on Prior Works by Tee, Mars and Fatemi”. In: *Polymers* 17.7 (2025). ISSN: 2073-4360. DOI: 10.3390/polym17070918. URL: https://www.mdpi.com/2073-4360/17/7/918.

[79] X.-L. Wang et al. “Fatigue crack propagation characteristics of rubbery materials under variable amplitude loading”. In: *Results in Physics* 10 (2018), pp. 233–240.

[80] S. Wenbin et al. “Experiment and modeling of uniaxial tension fatigue performances for filled natural rubbers”. In: *Materials & Design* 58 (2014), pp. 65–73. URL: https://api.semanticscholar.org/CorpusID:137652409.

[81] X. Xue et al. “Mechanical behaviours of a hybrid composite with orthogonal spiral wire mesh and polyurethane elastomer”. In: *Research square* (June 2023).

[82] Y. Yin, Z. Yang, and M. Shi. “Dynamic mechanical response for bituminous mixtures in wide frequency range”. In: *IOP Conference Series: Materials Science and Engineering* 592 (Sept. 2019), p. 012059.

[83] P. Zheng et al. “Fatigue life prediction and effects of cerium oxide□filled vulcanized natural rubber on fatigue life under multiaxial loading”. In: *Fatigue and Fracture of Engineering Materials and Structures* 44 (2021).

[84] A. Zine, N. Benseddiq, and M. Naït Abdelaziz. “Rubber fatigue life under multiaxial loading: Numerical and experimental investigations”. In: *International Journal of Fatigue* 33.10 (2011), pp. 1360–1368. ISSN: 0142-1123.

10

Appendix

10.1. Dimensions uniaxial tension specimen

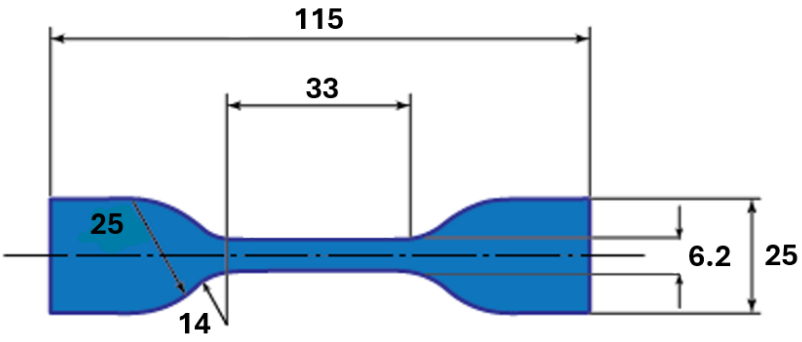

Figure 10.1: Dumbbell specimen dimensions (mm) Trelleborg

10.2. Dataset uniaxial fatigue including different R-ratios

Table 10.1: Fatigue life results FEA modeling [77]

$Nr.$	$\delta_{\min}$ (mm)	$\delta_{\max}$ (mm)	$\epsilon_{\min}$ (–)	$\epsilon_{\max}$ (–)	$\sigma_{\min}$ (MPa)	$\sigma_{\max}$ (MPa)	SED (MJ/m^3)	R_{ratio}	ω (Hz)	N_f (cycles)
1	0.00	38.76	0.00	0.79	0.00	2.80	0.89	0.00	5	84994
2	0.00	36.07	0.00	0.75	0.00	2.56	0.79	0.00	5	126560
3	0.36	31.64	0.01	0.68	0.02	2.18	0.62	0.01	5	146934
4	0.00	26.41	0.00	0.59	0.00	1.75	0.44	0.00	5	264222
5	0.36	21.62	0.01	0.50	0.02	1.39	0.31	0.01	5	485644
6	0.00	18.64	0.00	0.44	0.00	1.17	0.23	0.00	5	812012
7	0.00	16.28	0.00	0.39	0.00	1.01	0.18	0.00	5	1404492
8	3.34	39.46	0.09	0.80	0.19	2.83	0.92	0.07	5	126954
9	1.84	29.25	0.05	0.64	0.11	1.95	0.53	0.05	5	187636
10	3.73	32.25	0.10	0.69	0.22	2.23	0.63	0.10	5	244933
11	5.66	35.42	0.14	0.74	0.33	2.50	0.73	0.13	5	417953
12	8.05	31.64	0.20	0.68	0.47	2.18	0.57	0.22	5	463240
13	4.11	25.85	0.10	0.58	0.24	1.71	0.41	0.14	5	474589
14	2.59	17.69	0.07	0.42	0.15	1.10	0.20	0.14	5	916558
15	3.73	21.11	0.10	0.49	0.22	1.35	0.28	0.16	5	921771
16	3.34	16.74	0.09	0.40	0.19	1.04	0.18	0.18	5	1896574
17	-5.66	38.08	-0.15	0.78	-0.32	2.74	0.89	-0.12	5	148542
18	-17.16	39.45	-0.47	0.80	-1.06	2.87	1.17	-0.37	5	163539
19	-14.36	35.42	-0.39	0.74	-0.85	2.50	0.91	-0.34	5	181609
20	-1.95	34.13	-0.05	0.72	-0.11	2.40	0.72	-0.05	5	204281
21	-11.30	31.64	-0.31	0.68	-0.65	2.18	0.72	-0.30	5	212232
22	-7.99	28.10	-0.21	0.62	-0.46	1.89	0.55	-0.24	5	301805
23	-5.66	25.85	-0.15	0.58	-0.32	1.71	0.45	-0.19	5	336450
24	-0.66	21.62	-0.02	0.50	-0.04	1.39	0.31	-0.03	5	364001
25	-3.21	23.70	-0.09	0.54	-0.18	1.54	0.37	-0.12	5	399140
26	-16.26	25.85	-0.48	0.58	-0.99	1.71	0.67	-0.58	5	532498
27	-13.37	22.65	-0.36	0.52	-0.79	1.46	0.47	-0.54	5	805766
28	-6.25	21.11	-0.17	0.49	-0.35	1.35	0.32	-0.26	5	958260
29	-5.66	15.82	-0.15	0.38	-0.32	0.97	0.19	-0.33	5	1205349
30	-9.12	18.64	-0.25	0.44	-0.52	1.17	0.30	-0.44	5	1631035

11

Academic Paper

Damage Evolution and Failure Prediction in Rubber Marine Cone Fenders Subjected to Cyclic Loading

R. Kenters[1], C.L. Walters [1], J. Jovanova [1], A.A. Roubos [1], A.F.J. van Deyzen [2], M. Gaal [3]

[1]Delft University of Technology, Delft, The Netherlands
[2]Haskoning, Delft, The Netherlands
[3]Trelleborg, Rotterdam, The Netherlands

Abstract -

Rubber marine cone fenders play a crucial role in port infrastructure by dissipating the berthing energy of a vessel. However, their performance under cyclic loading remains poorly understood. Current PIANC guidelines do not provide limits for fatigue related damage, leaving a gap to predict its service life. This research addresses this gap by using Finite Element Analysis (FEA) to characterize the damage evolution in cone fenders. The highest relative decrease in service life was found to occur in deflections up to the buckling point. Furthermore, when the loading velocity increases by a factor of eight, this resulted in a reduction of 57% of its service life for deflections near the buckling point. Finally, a geometric optimization identified two key dimensional parameters that improved energy absorption by 32% until the maximum principal stress limit occurred, resulting in a design with an improved service life for cyclic loading conditions.

Keywords -

Rubber Cone Fenders, Service Life, Fatigue, Cyclic Loading, Damage Parameters

1 Introduction

Marine fenders are essential components in port infrastructure, designed to protect vessels and quay structures from forces that occur during mooring operations. The main function of a fender system is to absorb the energy of a berthing vessel and to dissipate the associated reaction forces into the supporting structure [1]. Before fenders were developed approximately 60 years ago, old wires and wood were used for this application. From then on, the fenders have developed significantly in both size and variety to handle the increasing dimensions and diversity of vessels [2]. Ports play a crucial role in the distribution of goods, since 80% of goods are transported by sea [3]. When fenders suddenly fail, this can lead to delays in operations, damage to vessels and qua walls, and increased maintenance costs. In busy ports, this will have a significant impact on supply chains and the economy. Moreover, sudden failure of fenders, may lead to additional safety risks to personnel and in case of the transportation of chemicals, this may even lead to environmental accidents such as oil spills. Since ports have become busier over the years [4] and vessel sizes are increasing, this topic will become even more relevant. Today, in most cases, rubber cone fenders with steel panels are used due to their high efficiency, energy absorption capabilities, and suitability for angular loads. Therefore, this study is focused on that specific type. Currently, the fender selection process is based on berthing energy and does not take cyclic loading into account. When vessels such as Floating Storage and Regasification Units (FSRUs) are permanently moored in harsh wave and wind environments, this can cause 500.000 fender compressions per year [5] due to resonant vessel motions. Resonant vessel motions typically occur when the wave or wind forces match or are close to the vessel's natural frequency [6]. The PIANC 2024 [1] considers 3000 full compression cycles for experimental durability testing raising the question of whether cone fenders can withstand this large number of deflections without failure. In recent cases in the industry, cone fenders failed too quickly due to complete rupture in cases with cyclic loading. The PIANC 2024 mentioned that within the current guidelines, there is insufficient data available to provide limits for cone fenders subjected to a large number of fender compressions. This study will use experimental and numerical models of the behavior of rubber to estimate the damage development and predict the service life of cone fenders subjected to cyclic loading. Furthermore, it proposed a design with improved service life for these specific cases.

2 Experimental tests

Uniaxial tension and compression tests were performed in the Delft University laboratory to characterize the stress strain relation of the specific rubber compound used in cone fenders. The dumbbell specimens for tension and the cylindrical specimens for compression were obtained from Trelleborg and are according to the ISO 815-1 standard. Three uniaxial tension and three uniaxial compression tests were performed at different engineering strain rates to capture the rate dependence, each scaled by a factor ten between. To ensure redundancy, each test was repeated three times, after which the average was taken per test.

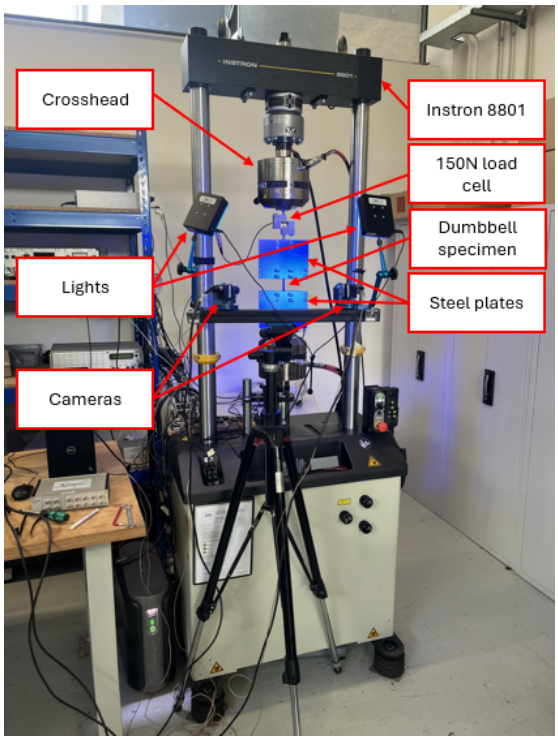

Figure 1. Instron 8801 servo-hydraulic setup

The test setup for uniaxial tension and compression is given in Figure 2. For uniaxial tension, self-fabricated steel plates were integrated to tighten the dumbbell-shaped specimen with 16 bolts with an additional 150 N load cell. During the compression tests, standard compression plates were used, including the 100 kN load cell located inside the Instron. DIC (Digital Image Correlation) was applied to measure the displacements on the surface of the gauge length of the dumbbell specimen for uniaxial tension. For the uniaxial compression tests, the displacement was determined by measuring the crosshead displacement, as this setup provides greater rigidity and focus on the reduction in height of the cylindrical specimen.

Figure 2. Uniaxial tension and compression

2.1 True stress strain relations

The true stress strain relations of the uniaxial tension and compression tests performed are given in Figure 3 and Figure 4, respectively.

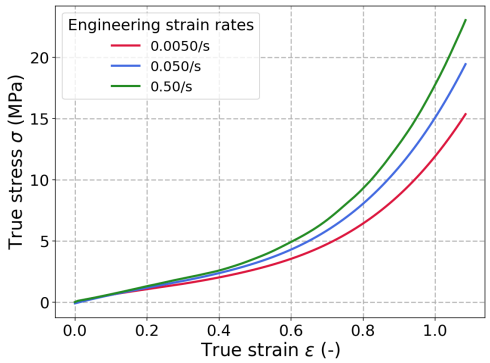

Figure 3. Stress strain relations uniaxial tension

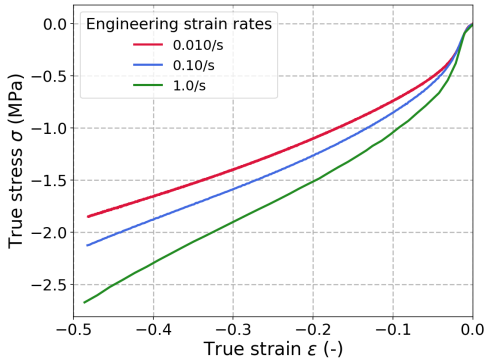

Figure 4. Stress strain relations uniaxial compression

2.2 Determination parameters hysteresis model

The hysteresis material model is an advanced model for predicting non linear, time dependent, and large strain behavior of elastomers. The response of elastomers is modeled by two parallel networks. Network A is a non linear hyperelastic network and network B consists of a non linear hyperelastic network in series with a non linear viscoelastic network. The hysteresis material model is implemented in Abaqus [7] under the sub option *HYSTERESIS. The MCalibration software package [8] was used to determine the parameters of the hysteresis material model. The Levenberg-Marquardt Algorithm (LMA) is implemented [9] in MCalibration to fit the model to the experimental data. It was found that the Arruda-Boyce formulation had the highest correlation with the experimental data. This model is also known as the Bergström-Boyce implemenation in Abaqus in combination with network B. The parameter fit resulted in a normalized absolute difference of 9.4% with the experimental data and is shown in Figure 5 with the corresponding parameters in Table 1.

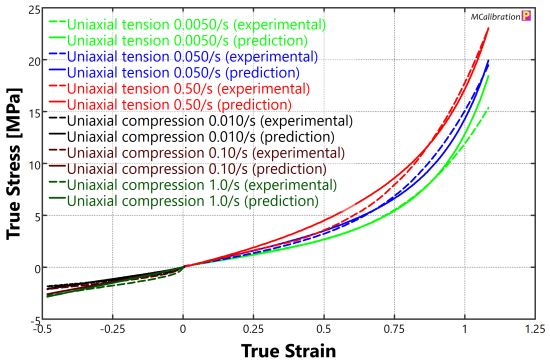

Figure 5. Bergström-Boyce model curve fitting

Table 1. Parameters Bergström-Boyce model

Parameters	Value	Unit
μ	0.75	MPa
λ	1.86	-
D	0	MPa
S	0.98	-
A	0.0057	$s^{-1}MPa^{-m}$
m	1.57	-
C	-1	-
E	0.032	-

3 Most suitable damage parameter

To investigate the ability of the maximum principal strain, maximum principal stress, and strain energy density (SED) to predict the fatigue life of rubber, a uniaxial data set on natural rubber of X.Wang et al. [10] has been used including various loading ratios ranging from -0.85 to 0.22. The dumbbell specimen was modeled in FEA as demonstrated in Figure 6 to gain insight into the corresponding stresses and strains. The hyperelastic material parameters of the rubber compound were described by the Mooney-Rivlin constants C_{10} and C_{01} being equal to 0.2897 MPa and 0.0599 MPa respectively. The correlations between the experimental data and the predicted values were determined using the polynomial least squares method. Based on the correlations analysis it can be concluded that the maximum principal strain and maximum principal stress perform consistently best across all loading ratios combined. However, the strain energy density was found to have the best correlation for loading ratios greater than zero but failed to predict loading ratios smaller than zero, resulting in a poor correlation for all loading ratios combined.

Table 2. Correlation coefficients (R^2)

Parameters	Combined	$R = 0$	$R > 0$	$R < 0$
Max principal strain	0.83	0.99	0.78	0.86
Max principal stress	0.82	0.99	0.76	0.86
SED	0.75	0.99	0.80	0.69

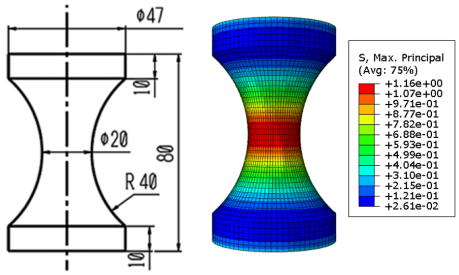

Figure 6. Modeling dumbbell specimen in FEA [10]

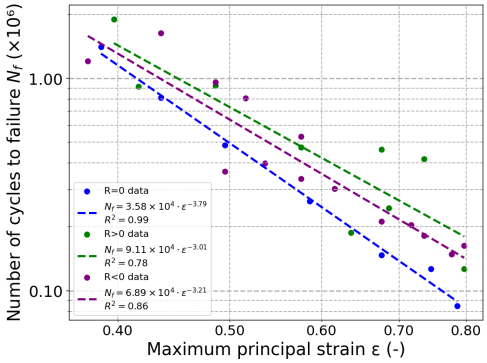

Figure 7. Maximum principal strain

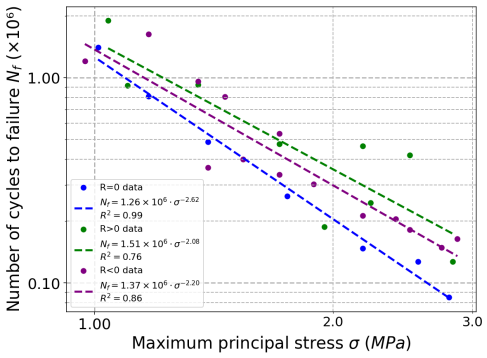

Figure 8. Maximum principal stress

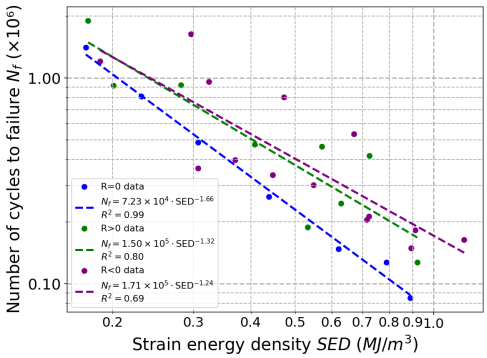

Figure 9. Strain Energy Density (SED)

3.1 Relation with multiaxial fatigue

In real-world applications, components such as cone fenders are often subjected to a multiaxial stress state. Therefore, the question arises whether the maximum principal strain and stress are also able to make reliable predictions under realistic multiaxial conditions. N.Saintier et al. [11] found that the maximum principal stress for natural rubber is able to predict the number of cycles to crack initiation and the crack orientation in uniaxial tension and torsion experiments corresponding to a multiaxial stress state. In addition, G.Ayoub et al. [12] found that for styrene butadiene rubber the maximum principal stress also worked for a multiaxial stress state. However, the maximum principal strain did not serve as a suitable damage parameter. Therefore, it was decided to select the maximum principal stress as the most suitable damage parameter for the cone fender.

4 FEA model cone fender

The cone fender was implemented in FEA and modeled with axisymmetric elements as illustrated in Figure 10 using an implicit quasi-static dynamic analysis. For this study, axisymmetric 4 node quadrilateral hybrid elements (CAX4RH) were used with reduced integration for computational efficiency. The steel plates (gray section) at the top and bottom are modeled as rigid bodies because of their high stiffness compared to the rubber (blue) section. The steel plate at the top is only allowed to move in the Y direction, and the steel plate at the bottom is constrained in each direction. On the upper surface, a displacement is given in the vertical direction.

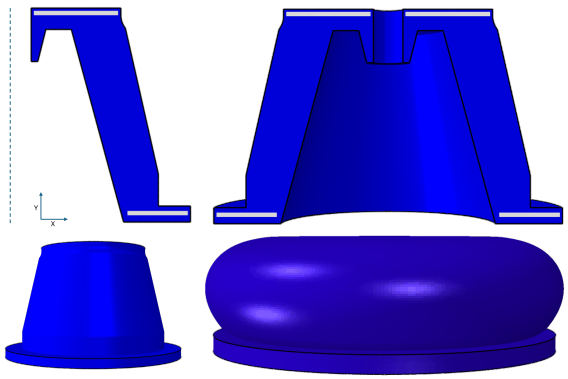

Figure 10. Cone fender implemenation FEA

4.1 Validation model

To validate the FEA model of the cone fender based on the experimental test data and the boundary conditions of the model, the force deflection curve from the Trelleborg product brochure [13] was compared to the results of the model in FEA with a compression velocity of 40 mm/s. As shown in Figure 11, the shape of the curve shows good agreement. However, the FEA model acts stiffer than the actual experimental curve with a maximum reaction force of approximately 14% higher. This deviation can be explained by the fact that the experimental data from the uniaxial tension and compression tests did not contain any preconditioning cycles. Therefore, the expectation is that the performance of the model in FEA will drop significantly during the first few load cycles due to the Mullins effect [14]. Furthermore, the post buckling behavior leads to a larger drop in reaction force. A possible explanation for this could be that the uniaxial compression tests reached a minimum true strain of -0.48, whereas the minimum true strain in the FEA model was found to be equal to -0.85 at 70% deflection.

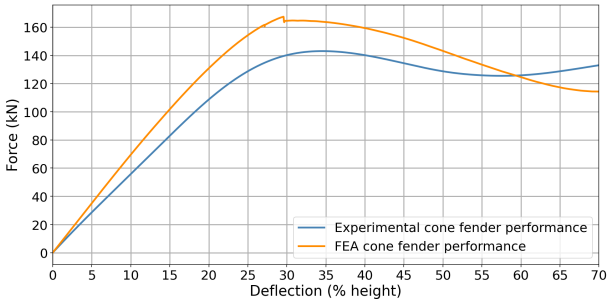

Figure 11. Force deflection curve comparison

4.2 Stress development

Since the maximum principal stress has been found as a suitable damage parameter, it was chosen to identify critical zones in the undeformed configuration of the cone fender based on the development of the maximum principal stress during a compression cycle ranging from 0 to 50% with a compression velocity of 40 mm/s. For further analysis, three critical elements within the critical zones have been selected as illustrated in Figure 12.

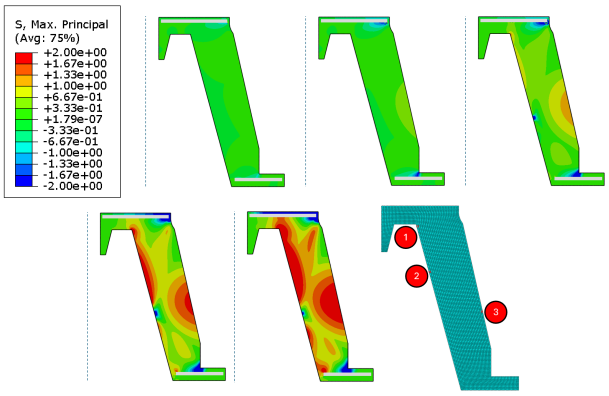

Figure 12. Maximum principal stress development

4.3 Service life prediction

The most suitable loading ratio (R-ratio) of the critical elements was investigated by applying six load cycles to the cone fender model in FEA. Even for the highest frequency studied, with a rest period of 3 seconds this resulted in a maximum principal stress that returned nearly to zero, leading to a loading ratio of zero. Therefore, the correlation in Equation 1 corresponding to the maximum principal stress with a loading ratio of zero was used for the service life prediction. The predictions are given in Table 3 and Figure 13 represents the number of cycles until crack initiation for each deflection using a polynomial fit between the calculated predictions in the table. The graph shows the relative highest reduction in service life in the range from 10% to approximately 30% deflection.

$$N_f = 1.26 \times 10^6 \cdot \sigma^{-2.62} \tag{1}$$

Table 3. Cycles until crack initiation (prediction)

Deflection (%)	σ **(MPa)**	N_f
10	0.15	181556351
20	0.54	6331387
30	1.18	816656
40	2.21	157783
50	3.45	49122
60	4.92	19383
70	5.70	13181

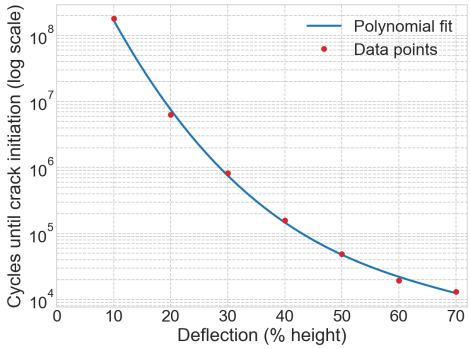

Figure 13. Polynomial fit N_f

4.4 Influence of loading velocity

Since rubber is rate dependent, the compression velocity will affect the stress states within the cone fender. Various compression velocities were applied to the model and the corresponding stress states were analyzed.

4.4.1 Stress strain relations critical elements

The maximum principal stress and principal strain relations for the critical elements are given in Figure 14, Figure 15, and Figure 16. To determine the influence of compression velocity on the stress states, a compression velocity of 10 mm/s was compared to 100 mm/s at a maximum principal strain of 0.3 in the critical elements. The increase in maximum principal stress at 100 mm/s relative to 10 mm/s was found to be 22.0%, 31.7%, and 26.8% for critical elements one, two, and three, respectively. This results in an average increase of 26.8% among the critical elements. The increase in stress in the experimental true stress strain relation in Figure 3 of the uniaxial tension tests was found to be 29.3%, scaled by a factor ten in engineering strain rate. This indicates that there is a minor difference of 2.5% between the average stress increase within the critical elements and the uniaxial tension tests.

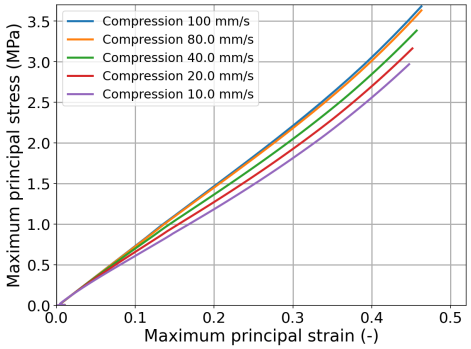

Figure 14. Critical element one

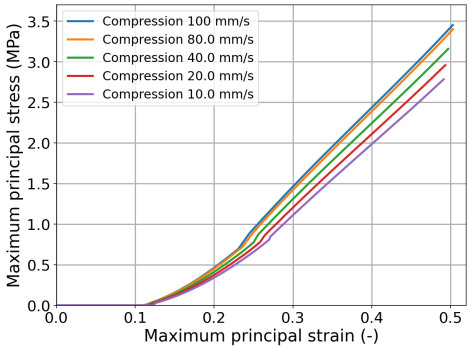

Figure 15. Critical element two

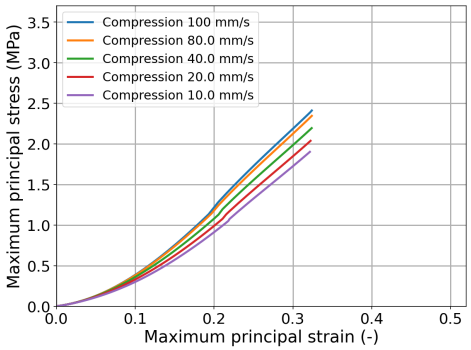

Figure 16. Critical element three

4.4.2 Relative increase stress and decrease service life

The higher loading velocities were compared to the slowest loading velocity of 10 mm/s. It can be observed that at 25% compression, the relative increase is highest. In case the fastest loading velocity of 80 mm/s is compared to the slowest of 10 mm/s, the maximum average increase in the maximum principal stress is 37% at a deflection of 25%, while this is only 22% at a deflection of 50% according Figure 17. Although stress increases for the critical elements with increasing loading velocity, this has an even greater influence on the predicted service life as shown in Figure 18. The relationship used is given in Equation 1.

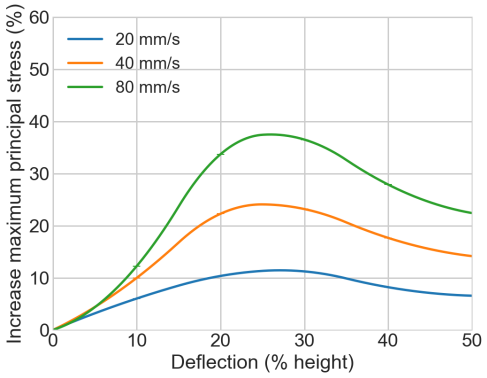

Figure 17. Stress increase compared 10 mm/s

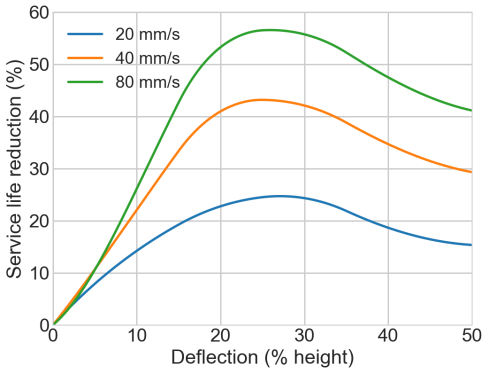

Figure 18. Service life reduction compared 10 mm/s

5 Cone fender optimization

The equations below represent the optimization approach followed to obtain a design that is more suitable for a large amount of small energies. The ultimate goal is to maximize energy absorption $E_{\sigma_{max}}$, up to the defined maximum principal stress limit of 1.8 MPa, which corresponds to a deflection of the original design of 35 percent according to FEA. Let $x \in R^n$ denote the set of design parameters. The boundary conditions are defined such that the minimum energy absorption until the stress limit is reached is at least equal to that of the original design, which corresponds to 14.6 kJ. In addition to this, the efficiency $\eta_{\sigma_{max}}$ must be at least 0.63, corresponding to the efficiency of the original design at the stress limit, to ensure that the reaction force on the structure and the vessel hull remain within reasonable limits relative to energy absorption. The efficiency can also be interpreted as a dimensionless number that indicates how much energy is absorbed relative to its theoretical maximum. In addition, the maximum reaction force $F_{\max,\sigma_{max}}$ reached until the stress limit must not exceed 200 kN, while the maximum reaction force in the original design is approximately 164 kN. The total energy absorbed until time step i is calculated with the trapezoidal rule according to Equation 3.

$$\textbf{Maximize} : \mathbf{E}_{\boldsymbol{\sigma}_{\mathbf{max}}}(x) \tag{2}$$

$$E_i(x) = E_{i-1}(x) + \frac{F_i(x) + F_{i-1}(x)}{2} \cdot \Delta d_i, \quad E_0 = 0 \tag{3}$$

$$F_{\max,i}(x) = \max_{0 \le j \le i} F_j(x) \tag{4}$$

$$\eta_i(x) = \frac{E_i(x)}{F_{\max,i}(x) \cdot d_i} \tag{5}$$

$$\sigma_{\max}(x) = 1.8\ MPa \tag{6}$$

$$E_{\sigma_{max}}(x) \ge 14.6\ kJ \tag{7}$$

$$\eta_{\sigma_{max}}(x) \ge 0.63 \tag{8}$$

$$F_{\max,\sigma_{max}}(x) \le 200\ kN \tag{9}$$

5.1 Geometric variation analysis

To gain insight into how small changes in the current cone fender design affect the design characteristics, a geometric variation analysis was performed. Five key geometric parameters were defined in Figure 19. For each key parameter, five difference scenarios were simulated while keeping the other parameters unchanged, including the height of 400 millimeters. The most important finding of the analysis was that changes in angle α, average thickness t, and angle β by changing the outside axis did not shift the point when the maximum principal stress limit was reached along the deflection (%) axis. This meant that the stress limit occurred at approximately the same percentage of deflection independent of the reaction force. However, when changing the distance r and the angle β by varying

the inner axis, the point at which the maximum principal stress limit was reached depends on the percentage of deflection. In addition, the initial stiffness of the cone can be significantly influenced by changing the distance r. Since there is expected to be an optimum between these two parameters. That is, achieving the highest possible stiffness before buckling, while at the same time increasing the point at which the maximum principal stress limit takes place in terms of deflection. These two parameters were explored further.

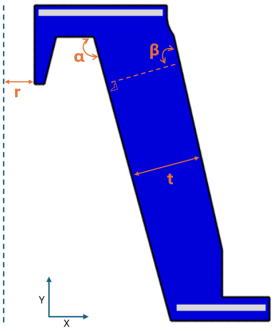

Figure 19. Key geometric parameters

In addition, the elements where the maximum principal stress limit was first observed during compression were often located in the sharp inner corner, as shown in Figure 20. To minimize this, it was decided to round the inner corner for further analysis. This corner will remain rounded in the study of the two parameters r and β.

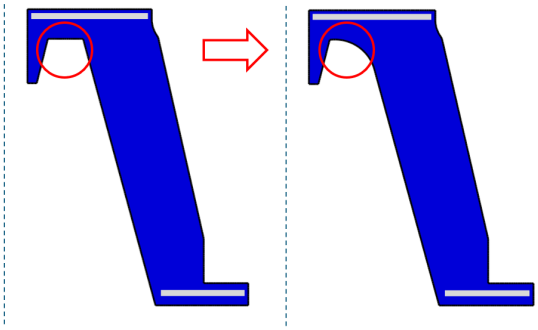

Figure 20. Rounded corner

In total, 20 concepts were developed with four variations in r and five variations in β. The force deflection curves are illustrated in Figure 21 where the bullet points represent the deflection at which the maximum stress limit occurs. In the bar chart in Figure 22 important characteristics of the cone fender are shown. The red bars do not meet the boundary conditions, while the green bars do, and the dark green bar is considered optimal. Therefore, it can be concluded that the concept with geometry modifications 2r and β+2 (nr.10) is the most optimal variant that satisfies all boundary conditions and has the highest energy absorption up to the stress limit.

5.2 Proposed design

The original cone fender and the proposed design are placed side by side in Figure 23. The proposed design is capable of absorbing 32% more energy until the point at which the maximum principal stress limit of 1.8 MPa is reached. In addition, the efficiency at the stress limit is 5% higher in the proposed design.

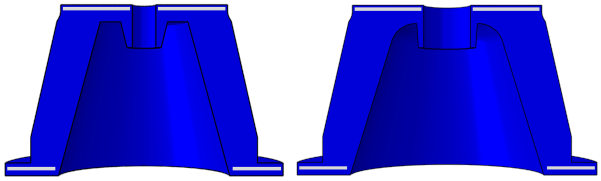

Figure 23. Comparison designs

Table 4. Important parameters comparison

Important parameters	Original	Proposed
$E_{i,\sigma_{max}}$	14.6 kJ	19.3 kJ
$\eta_{i,\sigma_{max}}$	0.63	0.66
$F_{\text{max, i},\sigma_{max}}$	164.3 kN	197.1 kN

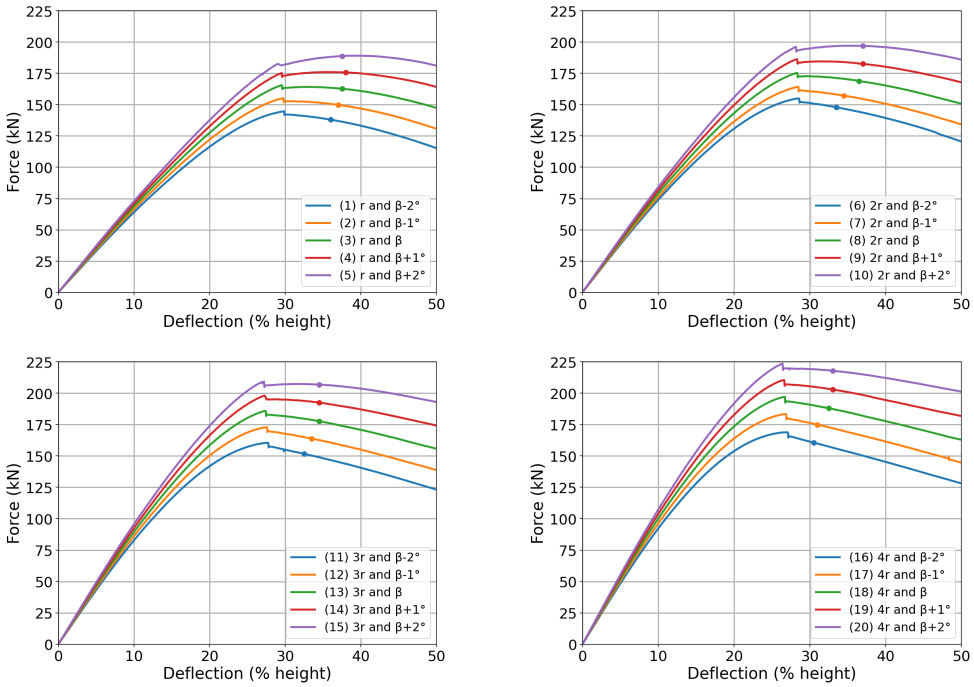

Figure 21. Combinations geometry parameters β and r

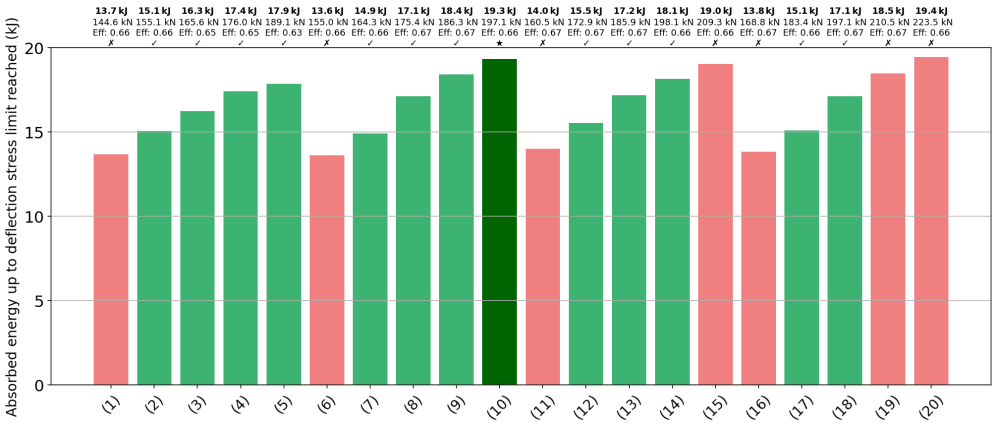

Figure 22. Important parameters 20 concepts varying β and r

6 Discussion

This research represented a framework for predicting the service life of rubber marine cone fenders subjected to cyclic loading. Uniaxial compression tests were performed until a true strain of approximately -0.5 due to high levels of friction with the steel plates for values smaller than -0.5 which is not desired. However, the minimum true strain of the FEA model was found to be -0.85 at a deflection of 70%. This difference could potentially result in the observed deviation of the force deflection curve of the FEA model compared to the experimental curve with large deflections. The Bergström-Boyce implementation in Abaqus was fitted to the experimental data of the uniaxial tension and compression tests at different strain rates with a normalized mean absolute difference of 9.4%. Using some additional equibiaxial and planar tests, this difference could most likely be reduced for more accurate insights. To make a cone fender more suitable for cyclic loading, it is important to keep the maximum principal stress in the cone as low as possible. Since stresses increase rapidly up to the buckling point, it is recommended to keep the deflection below 30% in any case. The proposed design exhibits a promising force deflection curve even after the buckling phase. However, the validity of its post buckling behavior is questionable since the original design does not fully align with the experimental post buckling results. Therefore, it is recommended to validate

this first by ensuring a perfect match between the original force deflection curve and the experimental results. This will, consequently, allow for proper validation of the proposed design.

6.1 Recommendations for further research

- **Investigating heat built up hysteresis rubber:** Heat built up due to hysteresis might play a significant role in the reduction of fatigue life of rubber when subjected to cyclic loading. Many studies focused on the influence of the ambient temperature on the rubber, but here they often neglect the self-heating effect due to its viscoelasticity. Therefore, it is recommended to investigate this effect further.

- **Effect variable loading amplitude:** Most of the fatigue tests performed in the laboratory are based on a constant amplitude. In practice, these load amplitudes often vary over time. Therefore, a damage model capable of converting load histories with different amplitudes into equivalent damage is needed.

- **Investigating impact environmental conditions:** Rubber is often exposed to high temperatures, UV radiation, ozone, and salt. The combination of environmental conditions can significantly reduce its fatigue life as a result of aging, and the extent of degradation is also dependent on the specific compound used. Therefore, it is recommended to include environmental aging in experimental tests to capture this in fatigue life predictions.

6.2 Design recommendations

- **Scalability cone fenders:** This study focused on an example cone fender from Trelleborg with a height of 400 millimeters. It is recommended to investigate internal stress development and consequently service life between different cone fender sizes. Although the dimensionless force deflection curve appears to be similar for all sizes, larger cone fenders may experience different stress concentrations due to scale effects. Additional numerical studies are therefore required to confirm whether the current service life predictions can be applied for al cone fender sizes.

- **Including radial forces in FEA:** This study assumed only axial compression, which allowed the model to be built with axisymmetric elements. However, in practice, radial forces will also play a role. This might lead to an overestimation of its service life. To investigate this, future research should develop an FEA model using full 3D elements, in which both axial and radial forces are applied to the model.

- **Fatigue dataset:** The most suitable damage parameter found in this research was based on a dataset from the literature that contained fatigue data from natural rubber with carbon black in it. However, the calibration experiments to fit a material model were performed with the compound used in Trelleborg their cone fenders. The exact compound of the rubber formulation can have a significant influence on the number of cycles until crack initiation. Therefore, it is recommended to perform the fatigue experiments with the same compound as used in the calibration experiments. In addition to this, it is recommended to perform the fatigue experiments for both a uniaxial stress state and for a multiaxial stress state by using torsion tests for example due to the multiaxial stress state that develops during the compression of the cone fender. This will result in a more accurate service life estimation of the cone fender in practice.

7 Conclusion

This research aimed to understand the correlation between the local distribution of stress and strain within a rubber cone fender and how this correlates with crack initiation. The maximum principal stress was identified as the most suitable damage parameter. The FEA model of the cone fender showed good agreement with the experimental curve, despite a slight overestimation of its stiffness and its post buckling behavior. The highest relative decrease in service life occurs in deflections up to the buckling point. The average increase in stress among critical elements was found to be the highest in the buckling phase by increasing the loading velocity. When the loading velocity increased by a factor of eight, the average stress in this phase increased by 38%, corresponding to a reduction of 57% of its predicted service life. Furthermore, the average increase in the maximum principal stress among the critical elements was found to be 26.8% at a strain of 0.3 when the strain rate increased by a factor of ten. This is 2.5% lower than the increase in stress in the uniaxial tension tests scaled by a factor of ten difference in engineering strain rate. However, the compression velocity does not affect each critical element equally with respect to the maximum principal stress. A geometric variation analysis had been conducted that resulted in the selection of two important dimensional parameters. Focusing on the inner radius and the angle of the inner axis led to a design that achieved a 32% increase in energy absorption up to the maximum principal stress limit while satisfying the boundary conditions.

References

[1] PIANC Working Group 211. Guidelines for the design, manufacturing and testing of fender systems. Technical Report 211, PIANC, 3 2024. Maritime Navigation Commission, PIANC.

[2] H. Akiyama, K. SHIMIZU, S. UEDA, and T. KAMADA. Investigation on service years of large rubber marine fenders. *Journal of JSCE*, 5(1):392–401, 2017.

[3] H. Naghash, D. Schott, and J. Pruyn. A review on global shipping projections and methodologies. *Journal of Shipping and Trade*, 9:29, 2024.

[4] T. Fadhilah, S. Rizal, and H. Firman. Port congestion solutions: The future of efficient transport networks in global trade. *Shipping and Transport Management Journal*, 2025.

[5] M. Gaal and M. Kumar. Cyclic conditions and impact on marine fenders. *35th PIANC World Congress, Cape Town, South Africa*, 2024.

[6] T. Gourlay and M. Kumar. The effect of fender energy dissipation on moored ship wave-induced motions. In *Australasian Coasts & Ports 2021: Te Oranga Takutai, Adapt and Thrive: Te Oranga Takutai, Adapt and Thrive*, pages 483–489. New Zealand Coastal Society Christchurch, NZ, 2022.

[7] Dassault Systèmes. *Abaqus 2024 Documentation*. Dassault Systèmes Simulia Corp., Providence, RI, USA, 2024.

[8] ANSYS Inc. Mcalibration, 2025. Material model calibration tool. Used with Qt version 6.5.5.

[9] H. P. Gavin. The levenberg-marquardt algorithm for nonlinear least squares curve-fitting problems. *Department of Civil and Environmental Engineering Duke University August*, 3:1–23, 2019.

[10] X. Wang, W. Shangguan, S. Rakheja, W. Li, and B. Yu. A method to develop a unified fatigue life prediction model for filled natural rubbers under uniaxial loads. *Fatigue Fracture of Engineering Materials Structures*, 37, 01 2014. doi:10.1111/ffe.12081.

[11] N. Saintier, G. Cailletaud, and R. Piques. Multiaxial fatigue life prediction for a natural rubber. *International Journal of Fatigue*, 28(5):530–539, 2006. ISSN 0142-1123.

[12] G. Ayoub. *Comportement en grandes déformations et fatigue des polymères : modélisation constitutive et prédiction de la durée de vie en fatigue*. Thèse de doctorat, Université Lille 1 Sciences et Technologies, 2010.

[13] Trelleborg Marine and Infrastructure. Fender systems product. `https://www.trelleborg.com`, 2025.

[14] L. Zhan, S. Qu, and R. Xiao. A review on the mullins effect in tough elastomers and gels. *Acta Mechanica Solida Sinica*, 37(2):181–214, 2024.


Delft University of Technology
TUDelft
Haskoning
Enhancing Society Together
TRELLEBORG